

Perovskites for next-generation optical sources

Quan, Li Na; Rand, Barry P.; Friend, Richard H.; Mhaisalkar, Subodh Gautam; Lee, Tae-Woo;
Sargent, Edward H.

2019

Quan, L. N., Rand, B. P., Friend, R. H., Mhaisalkar, S. G., Lee, T.-W., & Sargent, E. H. (2019).
Perovskites for next-generation optical sources. *Chemical Reviews*, 119(12), 7444–7477.
[doi:10.1021/acs.chemrev.9b00107](https://doi.org/10.1021/acs.chemrev.9b00107)

<https://hdl.handle.net/10356/140305>

<https://doi.org/10.1021/acs.chemrev.9b00107>

This document is the Accepted Manuscript version of a Published Work that appeared in
final form in *Chemical Reviews*, copyright © American Chemical Society after peer review
and technical editing by the publisher. To access the final edited and published work see
<https://doi.org/10.1021/acs.chemrev.9b00107>

Downloaded on 22 Jul 2024 04:06:48 SGT

Perovskites for Next-Generation Optical Sources

Li Na Quan¹, Barry P. Rand², Richard H. Friend³, Subodh Gautam Mhaisalkar⁴,

Tae-Woo Lee⁵, Edward H. Sargent¹

1. Department of Electrical and Computer Engineering, University of Toronto, 10 King's College Road, Toronto, Ontario M5S 3G4, Canada.
2. Department of Electrical Engineering and Andlinger Center for Energy and the Environment, Princeton University, Princeton, NJ 08544, USA.
3. Cavendish Laboratory, University of Cambridge, JJ Thomson Avenue, Cambridge CB3 0HE, United Kingdom.
4. Energy Research Institute, Nanyang Technological University, Research Techno Plaza, X-Frontier Block, Level 5, 50 Nanyang Drive, 637553 Singapore.
5. Department of Materials Science and Engineering, Seoul National University, 1 Gwanak-ro, Gwanak-gu, Seoul 08826, Republic of Korea.

E-mail: ted.sargent@utoronto.ca

Next-generation displays and lighting technologies require efficient optical sources that combine brightness, color purity, stability, substrate flexibility and, in certain applications, transparency. Metal halide perovskites are a promising platform for these applications, for they possess excellent charge transport, bandgap tunability and – in the most promising recent optical source materials – intense and efficient luminescence. This review links metal halide perovskites' performance as efficient light emitters with their underlying materials electronic and photophysical attributes.

CONTENTS

1. **Introduction: Overview of perovskites and their optoelectronic properties**
2. **Chemical Structural Diversity in Perovskites**
 - 2.1 Effect of organic and inorganic compounds

2.2 Effect of dimensionality in perovskites

2.2.1 Three-dimensional perovskites

2.2.2 Two-dimensional perovskites

2.2.3 Zero-dimensional perovskites

2.3 Lead-free perovskites

3. Perovskite Photophysical Properties

3.1 Recombination mechanisms

3.2 Exciton and free carrier dynamics

3.3 Photoluminescence quantum yield

4. Perovskite Light-Emitting Diodes (LEDs)

4.1 Perovskite materials engineering for LEDs

4.1.1 Modulating dimensionality in perovskites for LEDs

4.1.2 Colloidal synthesized perovskite nanocrystals for LEDs

4.2 Engineering perovskite LEDs toward high efficiency

4.2.1 Engineering interfacial layers

4.2.2 Perovskite LEDs compared with QLED and OLEDs

4.3 Stability of perovskite LEDs

4.3.1 Status and mechanisms underpinning stability in perovskite LEDs

4.3.2 Strategies to improve LED stability

5. Perovskites for Lasing

5.1 Optical amplification using perovskites

5.1.1 Original reports of perovskite lasing

5.1.2 Laser cavity structures in perovskite lasers

5.2 Cavity structures in perovskite lasers

6. Conclusions and Outlook

1. Introduction: Overview of perovskites and their optoelectronic properties

Hybrid perovskites are an emerging class of semiconducting materials exhibiting outstanding opto-electronic properties. The general chemical formula for perovskite materials is ABX_3 , in which A and B are cations and X are anions that octahedrally coordinate to B. The A-site cations are usually larger than the B-site cations, allowing $[BX_6]^{4-}$ octahedra to corner-share in a 3D framework, with the A-site cations located in the framework cavities. The canonical perovskite material is calcium titanate, discovered in the Ural mountains of Russia by Gustav Rose in 1839 and named after Russian mineralogist Lev Perovski (1792-1856).

Diverse perovskite materials exhibit ferroelectricity, superconductivity and magnetoresistance, to name a few of their intriguing properties. Metal halide perovskites can exhibit high absorption coefficients (in $CH_3NH_3PbI_3$ of order 10^4 cm^{-1}), high charge-carrier mobilities (exceeding $10\text{ cm}^2\text{ V}^{-1}\text{ s}^{-1}$), long minority carrier diffusion lengths ($1\text{ }\mu\text{m}$ and greater), and low trap densities (lower than 10^{16} cm^{-3}). These impressive properties make halide perovskites excellent semiconductors for solar cells. Since Miyasaka and co-workers introduced halide perovskites in liquid-electrolyte solar cells in 2009, thousands of researchers have turned their attention to perovskite solar cells (PSCs) (Figure 1)¹⁻⁶. The certified power conversion efficiency of PSCs has risen in nine years from approximately 3% to greater than 23%⁷ (Figure 2).

Halide perovskites also possess materials properties of interest for optical sources: bright photoluminescence, narrow light emission linewidth, tunable exciton binding energy and balanced charge carrier mobility^{8,9}. In the early 1990s, researchers applied layered structured halide perovskites (e.g. Ruddlesden-Popper phases) to create light-emitting diodes (LEDs) that operated

at liquid nitrogen temperature¹⁰. In 2012, room temperature halide perovskite LEDs were reported¹¹. In 2015, the first efficient perovskite LEDs (EQE~8.5 %) were reported¹². Studies of perovskite optical sources have similarly intensified in the past 6 years.

This Review discusses the structural and materials processing degrees of freedom available in perovskites and their impact on light emission and photophysical properties. We discuss cases for, and the challenges in, the use of perovskites in optical sources. We address device architectures in perovskite LEDs as well as interface engineering therein. We seek to connect device performance with underlying photophysics and perovskites' distinctive optical properties.

2. Chemical and Structural Diversity in Perovskites

Three distinct lattice positions in perovskites are referred to as the A, B and X sites. The highest symmetry phase perovskite occupies the $Pm3m$ space group in which the ions are perfectly packed and their ionic radii follow $r_A + r_x = \sqrt{2}(r_B + r_x)$ where r_A , r_B and r_x are the ionic radii of A, B and X. To study the stability of perovskites, Goldschmidt proposed the tolerance factor t and the octahedral factor μ . The tolerance factor indicates the state of distortion by $t = (r_A + r_x)/\sqrt{2}(r_B + r_x)$ and the octahedral factor is defined by the ratio of r_B/r_x for the BX_6 octahedron. In general, hybrid perovskites present $0.44 < \mu < 0.90$ and $0.81 < t < 1.11$. For the perovskite cubic structure, t falls between 0.9 and 1.0, whereas the 0.71 - 0.90 range exhibits tetragonal and orthorhombic structures (Figure 3). Many properties of perovskites depend on the details of structural distortions and, as a consequence, partial or full cation and/or anion substitution can be used to tune the physical properties. In metal halide perovskites, the B-site metal is typically a divalent cation (e.g., Pb^{2+} , Sn^{2+} , Ge^{2+} , Mg^{2+} , Ca^{2+} , Sr^{2+} , Cu^{2+} , Ni^{2+}), the A-site is a monovalent cation (e.g., Cs^+ , $CH_3NH_3^+$ (MA), $HC(NH_2)_2^+$ (FA) and the X-site is a halide or pseudohalide anion (e.g., I^- , Br^- , Cl^- etc.).

Layered two-dimensional (2D) perovskites and other lower-dimensional structures, such as one-dimensional (1D) chained and zero-dimensional (0D) isolated octahedra, add further tuning through chemical and structural engineering. Subtle chemical modifications can yield materials with nearly identical composition and structure yet dramatically different properties, including disparate bandgaps, exciton binding energies, and conductivities, making low-dimensional perovskites promising materials for tunable optoelectronics.

2.1 Effect of organic and inorganic compounds

To describe the symmetry of halide perovskites, one needs to consider the dynamic motion of organic A-sites and X-sites. Order-disorder of the A-site organic cation changes hydrogen bonding and, as a result, affects symmetry variations. The specific alignment of the A-site polar organic cation is often induced by hydrogen bonding with the perovskite framework, a fact that may result in bulk electric ordering¹³. Such electrical ordering is dependent on the dipole moments of the A-site and the strength of the hydrogen bonds (Figure 4). Organic cations (MA ions) possess an electrical dipole of 2.3 D¹⁴, an aspect that impacts the observed properties and behavior of perovskite solar cells (Figure 5). For example, the dipolar disorder of MA cations contributes to high dielectric constants in MAPbX₃, a fact that assists in screening charged states¹⁵. The incorporation of MA does not necessarily reduce the formation of defects, but the incorporation of the dipolar MA cation in mixed cation mixed halide wide-bandgap perovskites heals deep trap defects, resulting in a more defect-tolerant material¹⁶. Quasielastic neutron scattering (QENS) measurements have directly measured the motions of MA ions within the inorganic lattice of the perovskite. Density functional theory (DFT) on lattice dynamics indicates that low-energy phonons are composed entirely of the motion of metals and halides¹⁷⁻²¹, and that these are readily excited at lower temperatures and determine the ensuing physical properties.

In an ideal cubic halide perovskite, the B-site divalent metal is located at the body-centered position of the cube, and the anions occupy the six face-centered locations, forming an octahedral surrounding for the divalent metal, with the monovalent cations situated at the cube vertices. The chemical bonding between the metal and the halogen determines the bandgap and the dispersion of the energy bands in the material. Larger electronegativity differences correspond to a more ionic bond character, resulting in an electronic cloud less dispersed along the bond and located closer to the nuclei.

The inorganic metal cation at the B site is often chosen to be Pb^{2+} in light of the superior optoelectronic properties and solar cell performance of the resultant material. There is interest in finding ions to replace Pb in light of its environmental / toxicological properties²². Engineering the choice of the B site cation also affects the dimensionality of the perovskite structure, particularly so in the case of trivalent and tetravalent metal cations.

The X-site anion is chosen from the halides or halides (typically I^- and/or Br^-) and the bandgap energy of perovskites is varied by the alternation of the anion and the use of mixed anions. For example, the absorbance spectrum of the $\text{MAPbI}_{3-x}\text{Br}_x$ perovskites blueshifts as the bromide concentration is increased – a fact related to the lower electronegativity of the smaller halogen atoms. The optical absorption is therefore readily tuned, via bandgap engineering of halide perovskites, across the visible spectrum.

2.2 Effect of dimensionality in perovskites

Reducing perovskite materials' dimensionality also modulates their optical properties²³. The increased structural freedom creates the possibility to create larger and more complex structures with tailored photophysical and electronic properties. The ABX_3 structure has rigid structural constraints due to the corner-shared BX_6 octahedra crystal structure; whereas the extended family

of lower-dimensional perovskites allows increased structural flexibility, influenced by the length of interlayer organic cations. As the ABX_3 perovskite structure is cut into slices (layers), the size restrictions and the tolerance factor seen in the 3-D structures are gradually lifted. In two-dimensional (2D) layered derivatives of the perovskite structure, the interlayer A cation lengths are more easily tuned; and in the zero-dimensional (0D) derivatives, size restrictions are not applicable, as the isolated MX_6 octahedra shift readily in relative position (Figure 6).

2.2.1 Three-dimensional perovskites

Early embodiments of perovskite solar cells were demonstrated using three dimensional (3D) $MAPbI_3$ compounds in 2009. The 3D perovskites possess a sharp optical absorption onset, with an absorption coefficient (α) exceeding 10^4 cm^{-1} near the bandedge²⁴. The bandgap of $MAPbI_3$ is evaluated to be 1.50–1.55 eV using UV photoelectron spectroscopy. Measurements on single crystals of $MAPbI_3$ enabled detailed characterization of their optical and charge transport characteristics. Exceptionally low trap-state densities on the order of 10^9 cm^{-3} to 10^{10} cm^{-3} in $MAPbI_3$ single crystals – values comparables to those in high-quality silicon – and diffusion lengths on the order of 3-10 μm have been reported^{8,25}. Charge mobilities in thin film $MAPbI_3$ were obtained as high as $0.5 \text{ cm}^2/\text{Vs}$ using field-effect transistor measurements (FETs)²⁶. However, perovskites with MA cations have raised concerns regarding stability because of the organics' volatile nature – evaporation may be possible at temperatures as low as 85°C , and such materials have been seen to degrade upon exposure to moisture, heat and light soaking.

Replacing MA with other organic or inorganic cations tunes the bandgap of 3D lead halide perovskites. A new choice of A site cation changes the bandgap because of the modification of the lattice constant: FA is larger than MA, which in turn is larger than Cs, resulting in an increase of bandgap going from FA to Cs through MA. The A-site cation also influences the extent of metal-

halide orbital overlap. This change in metal-halide bonding has a direct impact on valence and conduction band positions²⁷.

The replacement of MA with formamidinium ($\text{HC}(\text{NH}_2)_2$; FA) was found to reduce the bandgap by about 0.07 eV, which has led to the most recent photovoltaic performance advances.

Because FA produces more thermally stable materials, FA-based perovskites have recently become a major avenue of research, promising higher efficiency and robustness. However, these FA compounds tend not to form the photoactive black perovskite phase at room temperature. Instead, a photoinactive yellow phase of FAPbI_3 , mixing of Br and I instead maintain the black phase, but achieve a wider bandgap. These considerations have led to a considerable recent focus on 3D perovskites in which the A cation is replaced with Cs^+ , and in which mixed triple cations (Cs/FA/MA) are employed to improve phase/thermal stability and performance in devices²⁸.

Mixed halide perovskites are of interest also in view of their continuous bandgap tunability (approximately 1.7 to 1.9 eV). Unfortunately, photoinduced ion segregation leads to bandgap instabilities even when mixed halides are used in mixed-cation perovskites. Recently, Stranks and co-workers demonstrated substantial mitigation of both non-radiative losses and photoinduced ion migration in perovskite thin films by passivating the surfaces and grain boundaries²⁹. Bandgap instability was substantially suppressed using other interface approaches. Barry and co-workers reported an approach to suppress halide redistribution by self-assembled long-chain organic ammonium capping layers at nanometer-size³⁰. The method was suppressing the halide redistribution/migration by forming nanometer-sized crystallites with self-assembled long-chain organic cation (*e.g.*, *n*-butylammonium (BA)) capping layers.

Substituting Pb with Sn in the organic–inorganic lead halide perovskites have been demonstrated to narrow the bandgap to 1.2–1.4 eV. Mixed Sn/Pb perovskites with the composition

with, $\text{CsPb}_{1-x}\text{Sn}_x\text{IBr}_2$ perovskite alloys fabricated via one-step antisolvent spin-coating methods³¹. Sn substitution would alter the driving force for phase segregation and increase the barrier for ionic diffusion, which might contribute to the enhanced phase stability.

The remarkable performance of 3D perovskite solar cells and LEDs are correlated with their long carrier lifetimes and high photoluminescence (PL) efficiencies. High-quality perovskite films exhibit longer PL lifetimes, and it has been claimed that grain boundaries have a negligible impact on performance. Ginger and co-workers used confocal fluorescence microscopy correlated with scanning electron microscopy to spatially resolve PL decay dynamics from films of nonstoichiometric $\text{MAPbI}_3(\text{Cl})$ perovskites. They observed that PL intensity and lifetime varied between different grains in the same film, even for films that exhibited long bulk lifetimes.

The grain boundaries in the perovskite film were dimmer and exhibited faster nonradiative decay. Chemical treatment with pyridine have proved for activating the dark grain boundaries and passivated to produce a bright state³².

2.2.2 Two-dimensional perovskites

Long-chain alkyl ammonium organic/inorganic lead halide perovskites were fabricated, early in perovskite studies, producing materials with the formula of $\text{A}'_2\text{MX}_4$, and often known as two-dimensional (2D) perovskites. Here A' is the long organic alkylammonium cation, M a divalent metal cation, and X a halide anion. Most reported layered (2-D) perovskite derivatives feature mono- or diammonium cations, with general formula of $(\text{NH}_3\text{RNH}_3)\text{MX}_4$ or $(\text{RNH}_3)_2\text{MX}_4$, where here R represents an organic functional group. The ammonium cations engage in hydrogen bonding with the anionic substructure; and the orientation and conformation of the organic cations is important in determining the crystal structure³³.

The lower-dimensional derivatives of the perovskite structure can be visualized as slices along different crystallographic directions in the parent 3D compounds; given this, the choice of the organic cations, reaction stoichiometry are among the most influential parameters in determining the orientation of the resultant inorganic frameworks. The dimensional reduction also has significant impact on the physical properties of the compounds. The bandgap of the compounds increases as the dimensionality of the structure is lowered, as in thin quantum wells of other semiconductors. Early research on low-dimensional perovskites reported the compound $(\text{C}_4\text{H}_9\text{NH}_3)_2(\text{CH}_3\text{NH}_3)_{n-1}\text{Sn}_n\text{I}_{3n+1}$ ³⁴. The 3D perovskite $\text{CH}_3\text{NH}_3\text{SnI}_3$ is a small-bandgap semiconductor; whereas the $n = 1$ compound $(\text{C}_4\text{H}_9\text{NH}_3)_2\text{SnI}_4$ is a larger bandgap semiconductor³⁴. Unfortunately, $(\text{C}_4\text{H}_9\text{NH}_3)_2\text{SnI}_4$ is sensitive to air, and degradation occurs within several hours. Material synthesis to device testing must be carried out in an inert atmosphere.

These layered materials are natural quantum-well structures, where the inorganic layers act as wells and the organic molecules as barriers. They possess large exciton binding energies (>100 meV) due to enhanced electron–hole interactions originating from the very different dielectric constants of the well and the barrier, while the decreased symmetry diminishes the forbidden electronic transitions and contributes to enhanced photoluminescence intensity, and correspondingly a high quantum yield. As a result of the strong confinement in wide range of structural flexibility, layered perovskites are well-suited to light-emitting applications.

In the early 1990s, electroluminescence (EL) was observed from $(\text{C}_6\text{H}_5\text{C}_2\text{H}_4\text{NH}_3)_2(\text{CH}_3\text{NH}_3)\text{Pb}_2\text{I}_7$; however, this was observed only at 200 K and with the application of a 10 kV/cm electric field³⁵. Thermal quenching of the exciton was the main reason for the reduction of EL near room temperature³⁶.

More recently, low-dimensional perovskites have attracted renewed interest for solid-state lighting applications. Higher-number layered compounds ($A'_2A_{n-1}Pb_nX_{3n+1}$) with $n = 2, 3, 4$, etc. are formed through intercalation of a mixture of cations, capable of forming both the 3D (A' ; $CH_3NH_3^+$, $HN = CHNH_3^+$, or Cs^+) and layered perovskite structure (A)³⁷⁻³⁹. By making films consisting of a range of n , one can produce energy funneling through a collection of grains having different bandgaps. This has been found to enhance luminescence properties at room temperature³⁷⁻⁴¹.

Low-dimensional perovskites with the formula $(A')_2(CH_3NH_3)_{n-1}Pb_nX_{3n+1}$ have also been demonstrated to stabilize solar cell performance against moisture, a finding explained by the increased formation energy compared with their 3D bulk perovskite counterparts^{23,42,43}. Lower dimensional perovskite derivatives typically feature different cuts from the 3-D structure along the $\langle 100 \rangle$, $\langle 110 \rangle$ and $\langle 111 \rangle$ directions. $\langle 100 \rangle$ -oriented perovskites are obtained through the ordered removal of the B-component from the inorganic framework. In contrast to the $\langle 100 \rangle$ -oriented perovskite hybrid that represents today the most richly-explored member of the reduced-dimensional perovskite family, the $\langle 110 \rangle$ - and $\langle 111 \rangle$ - oriented perovskites have rarely been reported. $\langle 110 \rangle$ -oriented organic-inorganic perovskites have the formula $[NH_2-C(I)NH_2]_2(CH_3NH_3)_nSn_nI_{3n+1}$ ($n=1-4$) and were reported by Mitzi and co-workers⁴⁴. These perovskites were stabilized via the incorporation of methylammonium and iodoformamidinium cations. Differently-dimensioned inorganic sheets are obtained by modulating the proportions of the two ligands. When $n > 2$, the methylammonium cations occupy the channel position defined by the corner-sharing metal halide octahedra. The iodoformamidinium cations play an important role in directing the self-assembly of $\langle 110 \rangle$ -oriented perovskites.

The compositions of the <111>-oriented perovskites are of the $A'_2A_{n-1}B_nX_{3n+3}$ formula, where A' and A are interlayer and intralayer organic cations. An example $n=1$ member is $(H_23-AMP)_2PbBr_6$ (AMP= (aminomethyl)pyridinium). These have a higher presence of the more distorted $PbBr_6$ octahedra, increasing the bandgap. Reported $n=2$ members, including $(NH_4)_3Sb_2I_9$, $(CH_3NH_3)_3Bi_2Br_9$, $[NH_2(CH_3)_2]_3Sb_2Cl_9$, $[NH(CH_3)_3]_3Sb_2Cl_9$, and $(CH_3NH_3)_3Sb_2I_9$, also feature small inorganic cations with $Cs_3Sb_2I_9$ ⁴⁵⁻⁴⁸.

2.2.3 Zero-dimensional perovskites

Structurally-distorted perovskites can be considered zero-dimensional (0D) analogs. Karunadasa and co-workers reported $(NMEDA)PbBr_4$ and $(EDBE)PbX_4$ (N-MEDA=N1-methylethane-1,2-diammonium; EDBE=2,2-(ethylenedioxy)bis(ethylammonium)), materials that exhibited white light emission^{49,50}. The wide PL linewidth was heavily influenced by the structural distortion, indicated by the distortion of the $PbBr_6$ octahedron⁵¹. White light emission was attributed to electron-phonon coupling and self-trapped excitons – excitons localized in the inorganic lattice. Mao *et. al.*, reported white light-emitting perovskites with composition $(DMEN)PbBr_4$ (DMEN=2-(dimethylamino)ethylamine); $(DMPA)PbBr_4$ (DMPA=3-(dimethylamino)-1-propylamine); $(DMABA)PbBr_4$ (DMABA = 4-dimethylaminobutylamine)⁵² (Figure 7). Among these compounds, $(DMEN)PbBr_4$ has the largest distortion ($\Delta d_{avg} = 17.4 \times 10^{-4}$) (where Δd_{avg} is the statistical average of Δd for each crystallographically independent octahedron) and showed the broadest emission in this series.

The perovskite-related Cs_4PbBr_6 structure – first synthesized in 1999 by Nikl *et. al.*⁵³ – presents a zero-dimensional (0D) crystalline structure in which adjacent $[PbBr_6]^{4-}$ octahedra do not share any corners (Figure 8). Manna and co-workers pioneered a facile fabrication strategy to produce Cs_4PbBr_6 , starting from $CsPbBr_3$ NCs, to obtain 0D Cs_4PbBr_6 NCs via the simple addition

of different amines at room temperature⁵⁴. The stability of these NCs in solution was rather low – the particles aggregated in a few minutes. Their optical properties, measured immediately following the transformation, were dramatically different from those of the starting CsPbBr₃ NCs, with a sharp absorption peak at 317 nm, no absorption in the visible range, and no significant PL. Cs₄PbBr₆ NCs can also be prepared in a Cs-rich environment through a hot-injection method⁵⁵. Water triggered a chemical transformation of CsPbBr₃ perovskite NCs from non-luminescent Cs₄PbX₆ to highly luminescent CsPbX₃. This was accompanied by encouraging stability in air and tunable optical properties. The extraction of CsX from Cs₄PbX₆ can be achieved either by thermal annealing (physical approach) or by chemical reaction with Prussian Blue (chemical approach)⁵⁶. Alivisatos and co-workers have synthesized another derivative of CsPbBr₃ NCs: they formed lead-halide-depleted perovskite derivative Cs₄PbBr₆ NCs. The transformation is governed by a two-step dissolution-recrystallization mechanism and mediated by the influence of the ligand shell environment on the crystal surface⁵⁷.

Since Cs₄PbBr₆ shows a large bandgap, researchers recently explored the incorporation of perovskite NC emitters into another crystalline transport phase⁵⁸. CsPbBr₃ quantum dots embedded in a robust and air-stable rhombic prism hexabromide Cs₄PbBr₆ microcrystal phase resulted in high luminescence properties, specifically PLQY exceeding 90% in the solid state. The authors demonstrated the role of a lattice match between CsPbBr₃ and the Cs₄PbBr₆ matrix. Chen *et. al.* reported a related study involving CsPbBr₃ embedded in a Cs₄PbBr₆ matrix and reported high efficiency and wide color gamut prototype white light-emitting diodes⁵⁹.

2.3 Lead-free perovskites

The regulated nature of lead (Pb) may limit the application of otherwise-promising perovskites. Therefore, there is considerable interest in identifying promising lead-free alternatives. One such

case is a class of materials known as double perovskites, in which two metals (*e.g.* metals with 1^+ and 3^+ oxidation states) are combined to yield the overall charge balance as seen in conventional single-metal-cation perovskites⁶⁰⁻⁶². One example is the cubic $Fm\bar{3}m$ double perovskite synthesized in the form of $Cs_2AgBiBr_6$, having an estimated indirect bandgap of 1.95 eV (as obtained from UV-Vis spectroscopy)⁶³.

Tin (Sn), closely analogous in many respects to Pb, has been investigated as a possible alternative to produce lead-free perovskites. Pb and Sn have a similar ionic radii (Pb 1.49 Å and Sn 1.35 Å), and analogous relativistic effects⁶⁴. Sn can therefore substitute Pb with no significant perturbation in the lattice structure. However, Sn^{2+} is easily oxidized to Sn^{4+} in air, can progress further to produce unacceptably high free carrier densities. Seok and co-workers reported an approach to bind SnF_2 strongly with pyrazine: the SnF_2 accepts lone pairs from the N atoms in pyrazine, and this combination of SnF_2 -pyrazine reduces Sn vacancies⁶⁵. The additive SnF_2 furthermore prevented Sn^{2+} from being oxidized to Sn^{4+} , reducing the background carrier density in $FASnI_3$ perovskites⁶⁶.

All-inorganic $CsSnX_3$ perovskites have been reported and applied to LEDs⁶⁷. Thin SnX_2 and CsX films were sequentially deposited by vapor deposition then annealed to form uniform $CsSnX_3$ films via interdiffusion. Smooth, uniform films $CsSnBr_3$ exhibiting full coverage and very small grain size (60 nm) were achieved; these exhibited a maximum external quantum efficiency (EQE) of 0.34% in red-emitting LEDs.

The 2D $(PEA)_2SnI_4$ exhibits superior PL properties compared to conventional 3D $CH_3NH_3SnI_3$, as reported by Haque and co-workers. These authors found that the 2D $(PEA)_2SnI_4$ perovskite displays improved stability compared to $CH_3NH_3SnI_3$ when aged in an air ambient in the dark⁶⁸. Kanatzidis and co-workers – using $CsGeI_3$ as their prototype compound – constructed

a series of Ge-based perovskites based on the trigonal pyramidal $[\text{GeI}_3]^-$ building block by tuning A-cations⁶⁹. They also demonstrated that Ge-based perovskites exhibit a large second harmonic generation (SHG) response resulting from the sp-hybrid orbitals of Ge and I.

Ternary Sb^{3+} and Bi^{3+} have also attracted significant attention due to their structural flexibility and low toxicity. The $\text{A}_3\text{Bi}_2\text{I}_9$ perovskites involve a 1/3 bi-deficient layered perovskite with bi-octahedral $(\text{Bi}_2\text{I}_9)^{3-}$ clusters surrounded by A^+ (Cs^+ or MA^+). However, trivalent bismuth and antimony perovskites result in lower dimensionalities and therefore wider bandgaps than their 3D analogues. To maintain the 3D perovskite architecture, an alternative approach was developed based on a combination of a monovalent cation and a trivalent cation in an ordered B-site arrangement, replacing Pb^{2+} to form a double perovskite structure of the formula $\text{A}_2\text{B}^{\text{I}}\text{B}^{\text{III}}\text{X}_6$ ⁷⁰. The perovskite showed the characteristics of an indirect bandgap semiconductor as confirmed by a Tauc plot, indicating that it may not be well-suited for efficient light emission. Diego and co-workers developed a mixed-metal $\langle 111 \rangle$ -oriented layered perovskite, $\text{Cs}_4\text{CuSb}_2\text{Cl}_{12}$, that incorporates Cu^{2+} and Sb^{3+} into layers that are three octahedra thick ($n = 3$)⁷¹. This material was a semiconductor with a direct bandgap 1.0 eV and a conductivity 1 order of magnitude greater than that of MAPbI_3 .

Recently, $\text{MA}_3\text{Bi}_2\text{X}_9$ ($\text{X}=\text{Cl}, \text{Br}, \text{I}$) perovskite quantum dots were synthesized by Jiang and co-workers⁷² (Figure 9). These authors used a ligand-assisted re-precipitation method that enabled them to tune the PL emission peak wavelength from 360 to 540 nm via halide compositional control. The $\text{MA}_3\text{Bi}_2\text{Br}_9$ QDs had diameter circa 3 nm and – for emission at 430 nm – the PLQY was an encouraging 12%.

3. Perovskite Photophysical Properties

The charge-carrier/exciton generation, diffusion, and recombination of free charge carriers/excitons are crucial to the operation of electronic devices. Electron-hole recombination rates are as low as those of the best-known single-crystalline inorganic semiconductors and are five orders of magnitude lower than that predicted by the Langevin model⁷³, as verified by Hall mobility measurements. In perovskites, the polycrystalline thin films have shown remarkably long carrier diffusion length ($L_D > 1 \mu\text{m}$) and long lifetime ($\tau \geq 1 \mu\text{s}$) and relatively modest mobilities ($\mu \approx 1\text{--}100 \text{ cm}^2 \text{ V}^{-1} \text{ s}^{-1}$)⁷³⁻⁷⁶, despite the presence of defects/traps. Here we review the nature of photogenerated exciton/carriers within the perovskites (Figure 22).

3.1 Recombination mechanisms

Transient absorption (TA) and time-resolved photoluminescence (TRPL) measurements have indicated a bimolecular recombination rate and a quadratic dependence of rate on pump fluence⁷⁷⁻⁸¹. In MAPbI_3 perovskites, the results of early spectroscopic investigations were by invoking the charge separated states, or excited charge transfer state⁸¹. It is now widely held that, upon photoexcitation, the excitons formed dissociate spontaneously into free electrons and holes, a fact that contributes to the impressive performance of perovskite devices. Under low excitation fluence with carrier densities $n_0 \approx 10^{13}\text{--}10^{15} \text{ cm}^{-3}$ (i.e., typical photovoltaic conditions), monomolecular processes of trap-assisted recombination or geminate recombination are found to be inefficient, having low first order recombination coefficients, $k_1 \approx 10 \mu\text{s}^{-1}$ ⁸². This agrees well with the low trap densities reported. At higher carrier densities $n_0 \approx 10^{16}\text{--}10^{18} \text{ cm}^{-3}$, multiparticle effects such as nongeminate recombination (bimolecular) and Auger processes (trimolecular) become dominant^{83,84}. The dynamics of charge-carrier recombination through monomolecular and higher-order processes can be written (eq 4):

$$\frac{dn}{dt} = G - k_1 n - k_2 n^2 - k_3 n^3 = G - nR_T(n) \quad (4)$$

where G is the charge-density generation rate, k_1 the monomolecular charge-recombination rate, k_2 the bimolecular electron–hole recombination rate constant, and k_3 the Auger recombination rate constant.

Kamat and co-workers found that MAPbI₃ undergoes strong band-filling effects and bandgap renormalization at higher pump fluence⁷⁷. Ultrafast relaxation processes in thin films of the semiconducting hybrid perovskite MAPbI₃ indicated a carrier-density-dependent blueshift and broadening of the 760 nm photogenerated ground state bleach, indicating charge carrier accumulation and explained on the basis of a dynamic Burstein–Moss shift. As photogenerated carriers thermalize, they fill sites near the conduction and valence band edges. This occupation of band edge states leads to higher-energy optical transitions as a result of the Pauli exclusion principle (Figure 23). The observation of this phenomenon in MAPbI₃ provides vital insight into the relatively unexplored excited-state character of halide perovskites.

Yang *et. al.*, have quantitatively correlated the TA spectra with many photophysical properties, including carrier density, the carrier temperature bandgap renormalization and exciton binding energy, and demonstrated the interplay between free-carrier induced bleaching of the excitonic and continuum transitions near the band edge⁸⁵. The carrier temperature can be extracted from the TA spectra and help to illuminate carrier cooling dynamics. Measurements have indicated slow hot-carrier cooling with high excitation density, attributed to a hot-phonon bottleneck. The observed hot-phonon bottleneck that slows the cooling of hot carriers by three to four orders of magnitude in time above a critical injection carrier density of $\sim 5 \times 10^{17} \text{ cm}^{-3}$.

3.2 Exciton and free carrier dynamics

Since hybrid halide perovskites at room temperature are free charges, rather than excitons, the monomolecular decay component observed for these materials originates from trap-assisted

recombination, which depends on the trap cross section, energetic depth, density, and distribution, which are determined by the crystal formation process and ensuing crystalline quality.

The bimolecular charge-carrier recombination between electrons and holes in a direct semiconductor is intrinsic photon-radiative recombination related to the reverse process of light absorption. Bimolecular recombination rate constants exhibit a lower dependence on material processing than does trap-assisted charge recombination. Values range between 0.6×10^{-10} and $14 \times 10^{-10} \text{ cm}^3 \text{ s}^{-1}$ at room temperature^{73,82,86}, which is comparable with the bimolecular recombination rate constant of $\sim 4 \times 10^{-10} \text{ cm}^3 \text{ s}^{-1}$ for the direct bandgap inorganic semiconductor GaAs^{74,79,87}.

Photoinduced terahertz conductivity measurements of MAPbI₃ and MAPbI_{3-x}Cl_x⁸² showed that one type of species appeared to contribute to the observed behavior, and this was identified as free charge carriers. In the presence of free charges, the measured relative change in THz electric field transmission is proportional to the photoinduced conductivity in the material. The observed dynamics could be explained by invoking the photoconductivity of free charges alone.

Auger recombination of charge-carriers is a many-body process involving recombination of an electron with a hole, accompanied by energy and momentum transfer to another electron or hole⁸⁸. The average range of Auger recombination values in halide perovskite is about $k_3 = (0.2\text{--}1.6) \times 10^{-28} \text{ cm}^6 \text{ s}^{-1}$ ^{73,82,86}, which is on average ~ 25 times higher than the Auger rate constant for GaAs⁸⁹.

A number of studies have sought to clarify the exciton binding energy in perovskites⁹⁰⁻⁹⁸. Coulomb correlations between electrons and holes affect the operation of photovoltaic cells because the resulting bound state (exciton) has an associated exciton binding energy (E_b) that needs to be overcome for electrons and holes to contribute to the photocurrent. For $E_b > kT$, thermal

energy suffices to dissociate the exciton; therefore, exciton binding energies below thermal energies at room temperature (26 meV) are highly desirable. The exciton binding energies for organic molecular semiconductors such as π -conjugated polymers are typically in the range of several 100 meV as a result of the low value of the dielectric function^{99,100}. The exciton binding energy for MAPbI₃ is sufficiently low for excitons to be described within the Wannier-Mott model. Wannier excitons are a hydrogen-like species comprising a conduction band electron of effective mass (m_e^*) and a valence band hole of effective mass (m_h^*) moving in a dielectric medium with relative permittivity (ϵ) as bound states with energies below the relevant band edge as described below (eq 5):

$$E_n = -\frac{m_e^* e^4}{8h^2 \epsilon_0^2 \epsilon^2} \frac{1}{n^2} = -\frac{E_b}{n^2} \quad (5)$$

From the above equation 5, MAPbI₃ with a bandgap energy of (~ 1.6 eV) has an estimated exciton binding energy in the range 2–20 meV. The range of experimentally reported values of E_b for MAPbI₃ is in good agreement with this, spanning 2 to 62 meV^{90-92,94,98}.

The temperature dependence of luminescence can be used to estimate the exciton binding energy. Temperature-activated exciton dissociation induces a decrease in photoluminescence intensity with increasing temperature. Here values have ranged from E_b of 19 meV¹⁰¹ - 32 meV⁹⁶ for MAPbI₃ and a higher 62 meV for MAPbI_{3-x}Cl_x⁹⁷.

An alternative approach to determining the exciton binding energy has leveraged analysis of the absorption spectra near the band edge⁹⁵. The width of the band edge absorption features as a function of temperature in the range 150–290 K suggests an E_b of (55 ± 20) meV from fits to data. Here the modeling assumed the coexistence of both homogeneous excitonic broadening mechanisms and temperature-independent inhomogeneous broadening arising from disorder. The considerable variation of E_b emerged again in this method due to the necessary incorporation of

line shape broadening mechanisms, which add to fitting uncertainties⁹⁸. An alternative approach based on fits to the temperature-dependence of the integrated absorption near the onset, normalized to a value at a particular energy, was used, and is sensitive to lineshape broadening⁹⁸.

A direct evaluation of the exciton binding energy was reported based on high-field interband magneto-absorption measurements⁹⁴ (Figure 24). The measurements give the reduced effective mass and this enables the study of multiple excitonic transitions for added precision.

In single grains of MAPbI₃, strong spatial heterogeneities on the nm length scale are present and associated with simultaneous free-carrier and exciton populations¹⁰². Using spectrally-resolved transient absorption microscopy, Harel and co-workers directly observed both red- and blueshifts of the band edge absorption across individual grains due to a dynamic Stark shift and screening of excitonic transitions by hot carriers. This observation helps to address a long-standing debate on the identity of the charge carriers, showing that both excitons and free carriers coexist, but are spatially segregated on the lengthscale of hundreds of nanometers.

In low-dimensional perovskites, confinement has been attributed to the large difference between the dielectric constants of the large organic barrier and the inorganic well. It is the generation of bound and long-lived excitons with exciton binding energies of several hundreds of meV that renders these materials good candidates for light-emitting applications such as lasers and LEDs. By combining distinct time-resolved microwave conductivity techniques, Grozema and co-workers performed a detailed temperature-dependent study of mobility and exciton dissociation in these materials¹⁰³. These measurements revealed that, at low temperature, the mobility of charges increases but the generation of free charges that are not Coulombically bound (*i.e.*, nonexcitonic) is less efficient – the formation of Coulombically-bound excitons is favored. This is accompanied by an increase in the fluorescence quantum yield that follows the opposite trend regarding the

fraction of free charges, *i.e.*, higher quantum yields at low temperature. This interconversion process is governed by E_b that depends strongly on the number of inorganic layers (n), ranging from ~ 370 meV for $n = 1$ to ~ 80 meV for $n = 4$.

3.3 Photoluminescence quantum yield

Measurements of the photoluminescence quantum yield (PLQY) of high refractive index materials, such as thin films of polymeric semiconductors, must overcome difficulties in determining the angular distribution of the emission, reflectivity, and absorbance. Adding to this complication are optical interference effects and potential photon recycling (reabsorption of emitted photons) that can occur in metal halide perovskites. A quantitative measurement of external PL efficiency is useful for a number of other reasons and was reported by Friend and co-workers¹⁰⁴. The external radiative quantum efficiency, η , is defined as:

$$\eta = \frac{\text{number of photons emitted}}{\text{number of photons absorbed}}$$

The group reported power dependent PLQY for a thin film $\text{MAPbI}_{3-x}\text{Cl}_x$ perovskites on glass¹⁰⁵. The PLQY was relatively low at low fluences (< 25 mW/cm²) but rises rapidly above 50% (by 100 mW/cm²) and reaches a maximum value of 70% at high excitation densities. The lower PLQE at low excitation fluence is attributed to the presence of defects through which nonradiative decay can occur. Radiative recombination becomes dominant over recombination at high fluences after the defects are filled. The rise in the PLQE at higher fluences suggests an excitation-density-dependent radiative recombination in perovskites.

Different approaches have been applied to maximize PLQY, such as the synthesis of lower dimensionality layered perovskites to increase the binding energies and oscillator strengths of the excitons; and also the use of spatial confinement. Charge confinement was introduced in MAPbBr_3 by reducing the grain size, which increased the radiative rate, and 36% PLQY was achieved in the

visible region at 530 nm¹². In the 2D PEA₂PbI₄ perovskites the PLQY was as low as 1% at room temperature, ascribed to thermal quenching of excitons^{36,37}. Mixed-phase low-dimensional perovskites exhibit much higher PLQY and LED EQE at room temperature^{37,38,40}. In perovskite for nanocrystals, surface traps can also hamper PLQY, and passivating halide-ion pair ligands has been shown to improve performance¹⁰⁶. Near unity PLQY for CsPbI₃ perovskite nanocrystals reported by Liu *et.al.* were achieved by improving a synthetic protocol that involves the use of trioctylphosphine–PbI₂ as a precursor – an approach that also leads to a significantly improved stability for the resulting CsPbI₃ nanocrystal solutions¹⁰⁷.

4. Perovskite Light Emitting Diodes (LEDs)

4.1 Perovskite material engineering for LEDs

Material engineering of perovskites is crucial to achieve highly luminescent PL properties: materials crystal structure, composition, domain size and surface chemistry all influence optical properties. Below we discuss the effect of each on fundamental optical properties and also device-level performance.

4.1.1 Modulating dimensionality in perovskite for LEDs

In the early 1990s, the Nurmikko and Saito groups^{10,35,108} reported LEDs based on layered 2D perovskites. The authors used a layered perovskite composition (C₆H₅C₂H₄NH₃)₂PbI₄ and measured the electroluminescence (EL) spectrum at liquid nitrogen temperatures ~ 77 K (Figure 10). An increased scattering rate due to phonons at higher temperatures accounted for the observed thermal quenching.

In 2014, Friend and co-workers¹¹ reported room-temperature perovskite LEDs based on CH₃NH₃PbI_{3-x}Cl_x having an external quantum efficiency (EQE) of 0.76% and radiance of 13.2 W

$\text{sr}^{-1}\text{m}^{-2}$ at a current density of 363 mA cm^{-2} . Lee and co-workers reported perovskite LEDs based on MAPbBr_3 and exhibiting a current efficiency (CE) of 0.577 cd A^{-1} , an EQE of 0.125%, and a maximum luminance of 417 cd m^{-2} (Figure 11)¹⁰⁹. Multicolored LEDs were demonstrated by leveraging the mixing of halides ($\text{CH}_3\text{NH}_3\text{PbCl}_x\text{Br}_y\text{I}_{3-x-y}$). The perovskite layer was designed to be thin enough to confine electrons and holes for bimolecular recombination, enhancing electron-hole capture and increasing radiative recombination. Making pinhole-free films containing crystalline particles, with overall thickness less than 50 nm, was a challenge. One method to overcome this film-formation challenge is to blend the perovskite precursors with a polymer that is also soluble in the solvents needed to process the metal halide and ammonium halide salts. For example, Li *et al.* blended perovskites with insulating polyimide and deposited uniform thin films¹¹⁰. The perovskite grains provided for charge transport and light emission, while the dielectric polymer filled the surrounding pinholes and thus filled potential shunt paths. A similar approach with mixed perovskite/poly(ethylene oxide) films also facilitated perovskite film formation, producing LEDs with relatively high brightness ($4,064 \text{ cd m}^{-2}$)¹¹¹. As the presence of metallic Pb atoms in MAPbBr_3 has been offered as a cause of trap-induced non-radiative recombination, Lee and co-workers addressed the film nonuniformity issue by providing excess MABr , reducing grain size and suppressing exciton quenching (Figure 12)¹². The spatially confined MAPbBr_3 grains (average diameter of $\leq 100 \text{ nm}$) were formed by a nanocrystal pinning process with additional TPBi dissolved in the solvent used for the anti-solvent quench. Perovskite LEDs based on this approach had a maximum current efficiency of 43 cd A^{-1} corresponding to an EQE of 8.5%. Park *et al.* further investigated the introduction of TPBi diluted in a volatile nonpolar solvent during the perovskite nanocrystal pinning process.¹¹²

Mixed Cs and FA cation perovskite LEDs developed by Cho *et. al.* incorporated Cs⁺ cations in FAPbBr₃ to reduce significantly the average grain size (from a wide 100-600 nm distribution to a more tightly-controlled average of 200 nm for FA:Cs = 90:10) and trap density; and increased the PLQY and PL lifetime in FA_{1-x}Cs_xPbBr₃ films and, correspondingly, the device performance increased from 1.7 to 3.1%. Incorporation of Cs also increased photostability of FA_{1-x}Cs_xPbBr₃ films due to the suppression of light-induced metastable states¹¹³.

Further exciton and carrier confinement was achieved using reduced-dimensional perovskites, as reported by Yuan *et. al.*, who used a perovskite mixed material comprising a series of differently quantum-size-tuned grains that funneled photoexcitations to the lowest-bandgap emitters in the mixture³⁷ (Figure 13). Quasi-2D perovskites with a composition of PEA₂(CH₃NH₃)_{n-1}Pb_nI_{3n+1} (PEA=C₈H₉NH₃) were used to tune the average layer numbers $\langle n \rangle$ by changing the ratio between PEA₂I and CH₃NH₃I. Transient absorption (TA) and time-resolved PL spectroscopy enabled characterization of transport and recombination processes at ultrafast timescales, providing a view into the transfer and recombination dynamics of photogenerated excitations. These studies of excitation dynamics revealed how multi-phased perovskite materials channel energy across an inhomogeneous energy landscape, concentrating excitons into the smaller-bandgap emitters (larger n). Perovskite LEDs with $\langle n \rangle = 5$ perovskite exhibited the best performance within this study, with an EQE of 8.8% and radiance of 80 W Sr⁻¹ m⁻², with emission at wavelength 750 nm.

The energy landscape in quasi-2D materials was further engineered by manipulating the crystallization process. Quan *et. al.* tailored the composition of quasi-2D perovskites to direct energy transfer into the lowest-bandgap minority phase – a process that occurred faster than loss due to nonradiative centers, thus helping to increase PLQY⁴⁰. By optimizing the domain

distribution, the authors achieved a high PLQY of 60% at low excitation fluences (1.8 mW cm^{-2}) in materials exhibiting green emission.

Multiple quantum well strategies explored by Wang *et. al.* used a mixture of 1-naphthylmethyllummonium iodide (NMAI) and formamidinium iodide (FAI)^{39,114} (Figure 14). The mixed material showed a high PLQY of 60% since photogenerated excitons in small-*n* QWs were efficiently energy-transferred to large-*n* QWs. The mixed quantum well perovskite LEDs achieved narrow emission peaks at 736 nm, 685 nm, 664 nm, 611 nm or 518 nm via Br:I ratio tuning. The best-performing perovskite LEDs turned on at 1.3 V; and the devices achieved an EQE of 11.7% at 2.6 V with a current density of 38 mA cm^{-2} with an emission peak at 763 nm. Grain size engineering was further explored by Xiao *et. al.*³⁸. Large-group ammonium halides were added to the stoichiometric 3D perovskite precursor solution, and these acted as surfactants that constrained the growth of 3D perovskite grains during film crystallization, producing crystallites with dimensions as small as 10 nm and ultra-smooth films with roughness of less than 1 nm (Figure 15). These nanometer-sized perovskite grains coated with longer-chain organic cations (butylammonium halides) yielded efficient perovskite emitters: the resulting LEDs operated with EQEs of 10.4% and 9.3% for perovskite films based on MAPbI_3 and MAPbBr_3 , respectively. They also featured significantly improved device stability. The long-chain butylammonium cations that self-assemble at the crystallite surface impeded ion migration during device operation, significantly reducing hysteresis.

For pure red-emitting ($\lambda \approx 650 \text{ nm}$) perovskite LEDs, mixed halides (Br/I) allow the needed tuning of the electronic bandgap. However, because of instability of MA and FA iodide/bromide perovskites,¹¹⁵ new approaches have been sought to suppress halide redistribution. These include the use of self-assembled large group ammonium capping layers at nanometer-sized grain

surfaces³⁰. The formation of stable mixed-halide perovskite films addresses the phase instability caused by lattice inconsistency when using mixed MA/Cs cations; they suppressed halide redistribution and migration by forming nanometer-sized crystallites with self-assembled long organic chain organic cation (butylammonium) capping layers. Using stable mixed-halide perovskite films, researchers have been able to fabricate efficient and wavelength-tunable perovskite LEDs spanning the infrared to the green. Sneha *et. al.* tailored 3D perovskites to provide a near-monodispersed nanoparticle film prepared using a one-step *in situ* deposition method¹¹⁶. Partially replacing MABr with OABr (octylammonium bromide; $\text{CH}_3(\text{CH}_2)_7\text{NH}_3\text{Br}$) in the perovskite precursor solution enabled controlled nanoparticle formation. An improved maximum brightness of $L_{\text{max}}=4578 \text{ cd m}^{-2}$ was achieved using this strategy.

4.1.2 Colloidally-synthesized perovskite nanocrystals for LEDs

Kovalenko and co-workers pioneered all-inorganic cesium lead halide (CsPbX_3 ; X = Cl, Br, and I) nanocrystals, which exhibited excellent optical properties, with tunable bandgap and high PLQY¹¹⁷ (Figure 16).

Tan and co-workers applied a trimethylaluminum vapor-based crosslinking method to render the nanocrystal films insoluble, thereby allowing the deposition of subsequent charge-injection layers without the need for orthogonal solvents¹¹⁸. The near-complete nanocrystal film coverage, coupled with the natural confinement of injected charges within the perovskite crystals, facilitate electron–hole capture and give rise to a remarkable electroluminescence yield of 5.7%.

Song *et. al.* then reported perovskite LEDs that utilized CsPbX_3 nanocrystals. High-quality CsPbX_3 nanocrystals were synthesized via the hot injection of the cesium precursor into a PbBr_2 precursor solution at high temperature¹¹⁹. The emission wavelength was tuned through both perovskite nanocrystal size and halide composition (Cl, Br, and I). Quantum yields were

impressive, in the range 60%–90%, especially strong in the case of the CsPbBr₃ films. In the blue, green, and orange spectral regions, LEDs based on a ITO/ PEDOT:PSS/PVK/QDs/TPBi/LiF/Al (PVK:Poly(9-vinylcarbazole), TPBi: 2,2',2''-(1,3,5-Benzinetriyl)-tris(1-phenyl-1-H-benzimidazole), PEDOT:PSS(poly(ethylenedioxythiophene):polystyrene sulfonate)) stack led to perovskite nanocrystal LEDs having luminances of 742 cd m⁻², 946 cd m⁻², and 528 cd m⁻², with EQE of 0.07%, 0.12%, and 0.09%, respectively. The insulating organic ligands on the surface of nanocrystals suppressed – in these early studies – the efficient injection of current, accounting for these initial device performance levels.

Replacing these long ligands (usually oleylamine (OAm) and oleic acid (OA), used for protecting the surface of CsPbX₃) with shorter ligands remains a challenge: it is imperative to achieve this without degrading or destabilizing perovskite nanocrystal films. Pan *et. al.* realized increased-stability films of CsPbX₃ NCs capped with a halide ion pair (di-dodecyl dimethyl ammonium bromide (DDAB)), a relatively short ligand that facilitates carrier transport in NC films and enhances thereby LED device performance¹⁰⁶. The ligand-exchange strategy included an intermediate step to desorb protonated OAm. As a result of new ligand-exchange strategies, halide-ion-pair-capped CsPbBr₃ NCs have enabled fabrication of LEDs with the device structure indium tin oxide (ITO)/ PEDOT:PSS/poly(9-vinlycarbazole)/NCs/TPBi/LiF/Al and achieved a maximum EQE and luminance of 3% and 330 cd m⁻², respectively.

Further progress toward CsPbBr₃ perovskite nanocrystal LEDs was made by Zeng and co-workers, who balanced surface passivation and carrier injection via ligand density control on perovskite nanocrystals¹²⁰. Using a hexane/ethyl acetate mixed solvent system, the authors controlled the surface ligand density: excess ligands had previously led to films with poor carrier injection and transport in device; while insufficient ligands caused the nanocrystals to have low

PLQY and poor stability. The mixture of hexane/ethyl acetate was found to achieve improved control over the ligand density on nanocrystal surfaces, mainly due to the relationship between the polarity of solvents and the ionicity of perovskites. Perovskite nanocrystal LED performance reached > 6% in EQE and an emission peak of 512 nm. Mixed-cation strategies in perovskites have also employed nanocrystals based on $\text{FA}_{(1-x)}\text{Cs}_x\text{PbBr}_3$ ¹²¹. An optimized composition of $\text{FA}_{0.8}\text{Cs}_{0.2}\text{PbBr}_3$, with LEDs exhibiting an increased luminance of 55,000 cd m^{-2} and a current efficiency exceeding 10 cd A^{-1} .

Most recently, extremely uniform and flat CsPbBr_3 film composing of self-assembly core-shell structured QDs based on one-step precursor coating¹²². The QDs size in the CsPbBr_3 film is around 4.5 nm (smaller than the Bohr radius), which significantly confines injected carriers and leads to an ultrahigh exciton binding energy (E_b) of 198 meV. This enables the resulting green perovskite LEDs to deliver an excellent device performance over 15% in EQE.

Red-emitting CsPbI_3 nanocrystals have been shown to suffer from a delayed phase transformation into a non-luminescent, wide-bandgap 1D polymorph, and MAPbI_3 exhibits very limited chemical durability. Seeking to overcome this issue, Kovalenko and co-workers pursued a facile colloidal synthesis that led to FAPbI_3 and FA-doped CsPbI_3 nanocrystals that are uniform in size (10–15 nm) and nearly cubic in shape. These exhibited dramatically higher robustness than the corresponding MA and Cs only perovskites having similar sizes and morphologies¹²³. Structural analysis indicated that the FAPbI_3 nanocrystals had a cubic crystal structure, while the $\text{FA}_{0.1}\text{Cs}_{0.9}\text{PbI}_3$ nanocrystals had a 3D orthorhombic structure that was isostructural to the structure of CsPbBr_3 nanocrystals. The PLQY reached 70% and spanned the red (690 nm, $\text{FA}_{0.1}\text{Cs}_{0.9}\text{PbI}_3$) and near-infrared (780 nm, FAPbI_3) regions. The PLQY was stable for several months both in the

colloidal state and in films. An EQE of 2.3% at current density 0.67 mA cm^{-2} was achieved in these FAPbI₃ nanocrystal LEDs.

Organic-inorganic hybrid perovskite nanocrystals also developed as promising candidates for LEDs. Formamidinium lead bromide perovskite (FAPbBr₃) nanoparticles have synthesized by Kim *et.al.*, by engineering the surface ligand of nanoparticles¹²⁴. Ligand engineering can improve the charge injection and transport capability in FAPbBr₃ films. With this ligand engineering method, maximum current efficiency of 9.16 cd/A in LEDs achieved. The perovskite nanocrystals film also reported on MAPbBr₃ with the dimension larger than exciton Bohr diameter (DB, regime beyond quantum size) by using a multifunctional buffer hole injection layer¹²⁵. With above strategies, the perovskite nanocrystal film exhibited a high PLQY of 60.5% without any complex post-treatments and multilayers and a high current efficiency of 15.5 cd/A.

Self-assembly of 3D FAPbBr₃ nanocrystals of graded size – mixed micro-platelets of octylammonium lead bromide perovskites – were synthesized by Chin *et. al.*, enabling an energy cascade that yielded high efficiencies in green-emitting LEDs¹²⁶ (Figure 17). Transient optical spectroscopy revealed an energy cascade from high-bandgap 2D (OA)₂(FA)_{n-1}Pb_nBr_{3n+1} platelets into progressively lower-bandgap FAPbBr₃ NCs, giving rise to high luminescence efficiency. Mesoscopic thin films comprising large plate-like domains of (OA)₂(FA)_{n-1}Pb_nBr_{3n+1} were sandwiched between electron and hole transporting layers that enabled an EQE of 13.4% and 56,000 cd m⁻² luminance.

4.2 Engineering perovskite LEDs towards high efficiency

Numerous approaches used to improve perovskite LED efficiency, besides those focused on enhancing PLQY and/or film morphology or composition, have relied on improving electron and/or hole injection. We discuss strategies that improve perovskite LEDs by engineering

interfacial layers in device structures, and differences of perovskite LEDs compared with alternative thin film quantum dot LEDs (QLEDs) and organic LEDs (OLEDs).

4.2.1 Engineering interfacial layers

In the early stage of developing perovskite LEDs, device architectures were inspired from perovskite solar cells: they often employed ITO/TiO₂/perovskite/F8 (poly(9,9'-dioctylfluorene)/MoO₃/Ag; and also leveraged inverted structures such as ITO/PEDOT:PSS/perovskite/TPBi/LiF/Al (Figure 18). Wide-bandgap ZnO nanocrystals have been employed as electron-transporting / hole-blocking layers in solar cells and LEDs because of the combination of high electron mobility, excellent optical transparency, and a deep valence-band energy level. However, perovskites deposited atop ZnO decompose due to the residual hydroxyl groups and acetate ligands on the surface of alkaline ZnO¹²⁷.

Wang *et. al.* developed perovskite LED structures that incorporate a multifunctional polyethyleneimine (PEI) interlayer between the oxide electron transporting layer and the perovskite layer¹²⁸. Deposition of the PEI interlayer on top of ZnO following washing with N, N-dimethylformamide (DMF) enhanced the quality of the perovskite film during crystallization. The structure ultimately combined (ITO)/PEI-modified zinc oxide (ZnO, 20 nm)/ CH₃NH₃PbI_{3-x}Cl_x (50 nm)/poly(9,9-dioctyl-fluorene-co-N-(4-butylphenyl)diphenylamine)(TFB, 25 nm)/molybdenum oxide (MoO_x, 8 nm)/gold (Au, 100 nm). Using this interfacial engineering approach, the authors achieved green-emitting perovskite LEDs exhibiting a maximum luminous efficiency of 4.0 lm W⁻¹ at a maximum luminance of 20 000 cd m⁻² and a low voltage of 2.8 V.

The low efficiency observed in perovskite LEDs was traced to high leakage current due to poor perovskite morphology, and also to high nonradiative recombination at interfaces and perovskite grain boundaries that led to imbalanced charge injection. Zhang *et. al.* incorporated a

small amount of MA into the CsPbBr₃ lattice; and also deposited a hydrophilic and insulating polyvinylpyrrolidone atop the ZnO electron-injection layer; all to overcome these issues¹²⁹.

Perovskite LEDs that used this strategy exhibited a high brightness of 91,000 cd m⁻² and an EQE of 10.4% when the mixed-cation perovskite Cs_{0.87}MA_{0.13}PbBr₃ was used as the emitting layer. The polymer buffer layer and the MABr additive significantly reduced the injection current in device, suppressed current leakage, and enhanced charge injection balance. The turn-on voltage was also slightly increased after inserting a (thin but insulating) polymer buffer layer.

A suitably-designed *n*-type semiconductor consisting of Ca-doped ZnO nanoparticles was then developed for use as the electron transport layer in perovskite nanocrystal LEDs. The bandstructure of ZnO was modulated via Ca doping, creating a cascade of conduction energy levels from the cathode to the perovskite. The electron mobility was observed to increase progressively with increased doping of Ca in the ZnO nanoparticles. The carrier mobility in undoped ZnO was found to be $2.4 \times 10^{-3} \text{ cm}^2 \text{ V}^{-1} \text{ s}^{-1}$, and increased with the Ca doping level to a peak value of $\mu_{\text{max}} = 5.7 \times 10^{-2} \text{ cm}^2 \text{ V}^{-1} \text{ s}^{-1}$ at 50% doping. Red-emitting perovskite LEDs exhibited significantly improved luminance with 19 cd A⁻¹ and EQE of 5.8%.

In the inverted device structure, TPBi is a widely-employed electron injection layer. Yan and co-workers used the blended electron injection layer B3PYMPM (4,6-bis(3,5-di(pyridin-3-yl)phenyl)-2-methylpyrimidine) and TPBi to tune the energy barrier between the ETL and the perovskite¹³⁰. In devices with TPBi as an ETL, the low electron conductivity ($4.2 \times 10^{-10} \text{ S cm}^{-1}$) and high energy barrier for electron injection caused by the high LUMO level of TPBi led to a higher driving voltage than in the B3PYMPM ETL device. PeLEDs with mixed ETLs showed reduced driving current density and an EQE_{max} of 12.9%, with a high η_{max} of 30.4 lm W⁻¹ at high brightness above 1000 cd m⁻².

The proper selection of hole transporting layers is important to balance charge injection and to form an ohmic contact with the active layer. The polymer F8, which has a deep ionization potential and a shallow electron affinity, was used to confine holes within the perovskite active layer, blocking electron egress. The high-work function MoO₃/Ag anode provided ohmic hole injection into the device¹³¹. Many perovskite LEDs and solar cells rely on expensive, unstable, and low-conductivity fluorenes for charge transport, such as spiro-OMeTAD (2,2',7,7'-tetrakis(N, N-di- p -methoxyphenylamine)-9,9'-spiro-bifluorene) or F8¹³². Exploring new electrode materials that overcome these limitations is an important challenge. Dan and co-workers used atomic layer-deposited ZnO films that formed at 60 °C and were deposited directly onto MAPbBr₃ perovskite¹³³. The electron injection barrier with the perovskite was reduced by incorporating Mg into ZnO to produce Zn_{1-x}Mg_xO. This decreased the electron affinity from -3.6 to -3.35 eV relative to vacuum and reduced the LED turn-on voltage.

Insertion of a buffer layer between electrode and semiconducting layers is a widely-employed strategy to control interfacial properties and ultimately improve device characteristics. Perovskite nanocrystal films on conventional PEDOT:PSS hole injection layers (HILs) often led to an inhomogeneous surface morphology. Pinholes and aggregated nanoplatelets reduced LED device efficiency. Also, exciton quenching by PEDOT:PSS at the PEDOT:PSS/perovskite film interface needed to be addressed – and interface engineering provided an attractive approach. Kim *et. al.* used a multifunctional HTL to minimize exciton quenching at the perovskite/HTL interface¹²⁵. With the above strategies, a high PLQY (~60%) in compact perovskite particle films was achieved without further post-treatment; and LEDs based on colloidal perovskite nanocrystals reached a high current efficiency of 15.5 cd/A.

Other attempts at transport layers include the use of inorganic NiO_x as an hole injection layer. Chih *et. al.* reported that a NiO_x electrode interlayer enhances emission from a MAPbBr₃ film active layer, this finding attributed to suitable hole level alignment and improved electron blocking – together, that increased the probability of radiative recombination in the active layer¹³⁴. Conjugated polyelectrolytes have been employed as the hole injection layer by Friend and co-workers¹³⁵. PCPDT-K (poly[2,6-(4,4- bis-potassium butanylsulfonate)-4H-cyclopenta-[2,1-b;3,4-b']-dithiophene)]) polyelectrolytes transfer holes efficiently, block electrons, and reduce luminescence quenching at the perovskite/PCPDT-K interface. Perovskite LEDs with PCPDT-K demonstrated a factor of approximately 4 increase in EQE compared to control devices that used PEDOT:PSS, reaching EQE of 5.7%, and with improved device stability.

4.2.2 Comparison of perovskite LED with QLED and OLEDs

We turn now to a discussion of quantum dots compared to perovskites in light-emitting applications. Quantum dots' tunable bandgap, as governed by the quantum size effect, simultaneously, and it's also among its disadvantages quite interestingly. This is owing to the need for a monodisperse population of dots. The confinement of electron–hole pairs (excitons) on the order of the bulk semiconductor's exciton Bohr radius (*e.g.*, 5.6 nm for CdSe) leads to quantization of the bulk energy levels, resulting in tunable spectra.

A precisely tailored spectrum can be used to generate a specific color temperature of white light. The quality of white light is measured in terms of a correlated color temperature (CCT) and color rendering index (CRI). For lower-CCT illumination at high temperature, it is particularly difficult to maintain high luminous efficiency and high color quality simultaneously because the required red luminophores must have relatively narrow emission spectra to avoid photon loss as infrared emission. Conventional red phosphors have emission spectra that are very broad (>60 nm

FWHM). The narrow spectral emission (~30 nm FWHM) of QDs offer more selective optical down-conversion of a portion of a backlight's bluer emission into redshifted light, leading to a CRI of >90% and a superior CCT of 2,700 K while maintaining a high luminance efficiency¹³⁶. This allows QDs to increase color quality while lowering power consumption in solid state light sources. QDs can also be utilized as backlights in high-color-quality liquid-crystal displays.

QDs do come with challenges. The importance of monodispersity in QDs for electronic is due to a rough energy landscape not only can it impede transport but it can also create “quantum traps” in which the presence of a small-bandgap inclusion could lead to enhanced recombination.

Charging can occur when under current injection – and this charging retards further injection, reducing electroluminescence (EL). The timescales associated with QD charging range from minutes to days¹³⁷. While the PLQY of QDs solution routinely often exceeds 95%, QDs deposited in a close-packed thin film exhibit lower – often by one order of magnitude – luminescence efficiency. Embedding QDs in an insulating polymer matrix decreases QD luminescence quenching^{138,139}; however, the electrical conductivity through these QD-polymer composites is impeded by the low conductance of the wide bandgap polymers. Förster resonant energy transfer (FRET) between closed-packed QDs can also reduce the PLQY of QD films¹⁴⁰.

While QDs are beginning to be deployed in applications such backlights in displays, organic LEDs (OLEDs) are already a multibillion dollar industry, with applications in displays, lighting, and consumer devices¹⁴¹. Most applications of OLEDs could benefit from a solution-processed approach, (instead of the prevailing vacuum sublimation process) where roll-to-roll solution-processing and inkjet printing could potentially be employed¹⁴²⁻¹⁴⁵. To achieve this, new high-performance active materials that are solution-processable would accelerate adoption. Efficiency roll-off represents another remaining area for improvement in OLEDs. This

corresponds to both a lowered power conversion efficiency as well as added electrical stress to achieve a given brightness, which works against device lifetime.

Perovskites offer pathways to color-saturated emission in view of their narrow emission linewidths (<30 nm) and manifest the possibility for future high-color purity emitters. The easy wavelength tuning, and efficient charge injection/transport property with perovskites have been intensively studied as promising candidates for future light emitters. Perovskite LEDs also have shown sub-bandgap turn-on voltages, implying the possibility of achieving low operating voltages and high power conversion efficiencies in display applications. Perovskite LEDs, since they can be processed from the solution phase, can potentially be inkjet printed. Processing temperatures will likely be quite low (less than 150 °C), making fabrication compatible with flexible and lightweight plastic substrates.

4.3 Stability of perovskite LEDs

The device stability in QD LEDs exhibit on the order of 100-1,000 hours when operated at relatively modest brightness (1000 cd m⁻²)¹⁴⁶. This is below the stringent requirements of commercial displays over $>10,000$ hours at higher brightness of 3000 cd m⁻². In contrast, the lifetime of state-of-the-art OLEDs is in the range of 10,000 to 100,000 hours. For early generations of OLEDs, instability was triggered by dark-spot effects, but device encapsulation and manufacturing optimization overcame these issues¹⁴⁷. The stability of lead halide based perovskite LEDs remains a major issue in this early-stage materials platform¹⁴⁸. Here we will discuss this challenge including recent studies towards increased device stability.

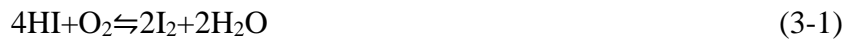
4.3.1 Status and mechanisms underpinning stability in perovskite LEDs

Perovskite solar cells' device lifetimes now exceeds one thousand hours under continuous operation while biased at the maximum power point.¹⁴⁹ Perovskite LEDs are at a less mature stage

from the point of view of reliability: often devices have ~ sub-hour consistent operation under continuous electrical stress before degradation becomes observable at a brightness level higher than 100 cd m⁻².

Some issues in perovskite LEDs are likely shared with perovskite solar cells. From PV it became clear that some compositions of thin films lack chemical and structural stability; and are prone to rapid degradation in the presence of moisture or heat. The strong ionic character of perovskites is linked to phase segregation and ion migration as well as to various electrochemical reactions¹⁵⁰⁻¹⁵³ (Figure 19).

In early 2014, stability issues in perovskites for PV gained the attention of a number of research groups. Fundamental studies on instability in perovskite thin films in the presence of moisture and the surrounding environment were reported by Niu *et. al*¹⁵⁴. Device fabrication needs to be carried out under controlled atmospheric conditions and with a humidity of <1% as shown by Gratzel and co-workers¹⁵⁵. The degradation process was proposed to follow this route:



In reaction (1), MAPbI₃ decomposes into MAI and PbI₂ in the presence of H₂O (Figure 20). In this process, the equilibrium constant is $k(1) = c(\text{MAI})$ and the Gibbs free energy is $\Delta G(1) = -RT \ln k(1)$. In reaction (2), MAI solution decomposes into MA solution and HI solution. Then the equilibrium constant is $k(2) = c(\text{MA}) \times c(\text{HI})/c(\text{MAI})$ and Gibbs free energy is $\Delta G(2) = -RT \ln k(1)$. In reaction (3), there are two ways for HI to react. (3-1) represents the redox reaction and can move forward readily. (3-2) represents the photochemical reaction - experimental evidence

revealed that HI can easily decompose into H_2 and I_2 under optical excitation. Ab initio molecular dynamics simulations further predicted surface reconstruction and light-assisted formation of hydrated species of $MAPbI_3 \cdot H_2O$ – a finding that agrees with the observation that exposure to water and light accelerates the degradation of perovskites^{156,157}.

Charge trapping at the interface between perovskites and charge extraction materials are responsible for irreversible degradation due to moisture¹⁵⁸. To understand charge-driven degradation mechanisms, it was important to develop controlled stability experiments both for commonly used $MAPbI_3$, which is known to form structurally distorted tetragonal crystals, and also for mixed perovskite materials having more enhanced structural stability. It was found that the mixed perovskite $MA_{0.6}FA_{0.4}PbI_{2.9}Br_{0.1}$ still degraded, although its degradation speed was slower than that of conventional $MAPbI_3$. It was further shown that the irreversible degradation of the perovskites was triggered by trapped charges.

Oxygen, in addition to moisture, can also trigger degradation¹⁵⁹. Darkening in PL also involved interaction with photogenerated carriers. The dynamics of PL in $MAPbI_3$ films were studied under continuous optical excitation. A competition between activation and darkening of PL was observed, and this was found to depend strongly on optical pump characteristics. Both photoactivation and photodarkening were strongly dependent on the intensity of the optical pump. When the optical photoexcitation intensity was increased, the perovskites PL increased linearly, and both activation and darkening dynamics in perovskite film is increased.

Photoactivation is likely related to the filling of sub-gap trap states, which limit the PL of the perovskite¹⁶⁰. The nature of these traps, which can be shallow or deep, depends on the kind of defect that produce the traps. Photoactivation is more efficient in the presence of O_2 than N_2 . If the activation process is in fact related to the filling of charge traps, oxygen plays a role in the process.

Photodarkening in perovskite films under prolonged optical excitation may arise from the degradation of the perovskite crystal structure under illumination. This moisture-related photodarkening is likely related to the formation of hydrated compounds whose formation is favored by photoexcited carriers, weakening hydrogen bonds between organic cations and PbI_6 octahedra and promoting the formation of complexes with H_2O molecules^{161,162}. While previous reports of perovskite hydration have been presented in the context of degradation of the material, these observations correspond to a reversible process when the sample is illuminated in O_2 . Further research is required to understand the detailed role of H_2O and O_2 in the photoactivated processes.

The mechanistic process of degradation investigated has been investigated using super-resolution luminescence micro spectroscopy¹⁶³. The MAPbI_3 crystal structure collapses to the two-dimensional layered PbI_2 structure; and degradation starts locally and then spreads across the entire crystal. The structural collapse is primarily due to migration of methylammonium ions, which distorts the lattice structure and causes alterations to the Pb-I-Pb bond angle and in turn changes the bandgap.

In addition to instabilities in perovskite materials, device instabilities can also come from interfacial layers and electrical stress during operation of device. Ionic processes, such as halide segregation, can destroy perovskites and generate defects,¹⁶⁴ some of which are voltage-induced and others spontaneous. Some examples include the corrosion/oxidation of electrodes¹⁶⁵⁻¹⁶⁸, degradation of charge-transport layers¹⁶⁹, and the formation of charge-accumulated interfaces¹⁵⁸ and $p-i-n$ junctions¹⁷⁰⁻¹⁷³. Furthermore, the diffusion of metallic species from electrodes, the origin of which is still unclear, can cause a significant decrease in device efficiency and accelerate the degradation of perovskite LEDs.

4.3.2 Strategies to improve LED stability

To improve LED stability, several approaches have been used. Inorganic CsPbX₃ based perovskites have been shown to improve LED stability compared with MA based perovskites¹⁷⁴, a finding associated with their enhanced thermal, structural, and chemical stability. The high thermal stability of CsPbBr₃ may improve the operational stability of perovskite LEDs, by suppressing degradation caused by thermal stresses, including Joule heating. Schaller and co-workers reported that the resilience of perovskite PL at temperatures below 450 K depends strongly on halide composition¹⁷⁵.

Another strategy to improve perovskite stability involves the use of layered perovskite structures. Perovskites of composition (PEA)₂(MA)₂[Pb₃I₁₀] have shown increased stability against moisture, attributed in part to the hydrophobic nature of the PEA layers. Using a density functional theory (DFT) approach, Quan *et. al.* proposed that the intercalation of PEA between perovskite layers introduces quantitatively appreciable van der Waals interactions. These drive an increased formation energy corresponding to improved materials stability.

Recently, quasi-2D perovskite/poly(ethylene oxide) (PEO) composite thin films were reported as the light-emitting layer in work by Ma and co-workers¹⁷⁶ (Figure 21 a). Controlling the molar ratios of organic (benzylammonium iodide) to inorganic salts (CsI and PbI₂), the group obtained luminescent quasi-2D perovskite thin films exhibiting tunable emission colors from red to deep red. LEDs with an emission peaking at 680 nm exhibited a brightness of 1392 cd m⁻² and an EQE of 6.2%. The EL intensity dropped by 20% relative following 4 hours of continuous operation; and these devices exhibited enhanced spectral stability.

Kim *et.al.*, reported the charge carrier recombination and ion migration induced by photo-excitation by analyzing steady-state and transient PL and photo-responsivity in perovskite nanoparticle films¹⁷⁷. These results indicate organic ligands in perovskite nanoparticle films

efficiently prevent ion migration and ion-migration-induced defects. These efficient confinement of electron-hole pairs and prevention of ion migration in perovskite nanoparticle films induced high photo-stability, PLQY of the perovskite films.

5. Perovskites for Lasing

5.1 Optical amplification using perovskites

Stimulated emission is the process by which photons induce radiative emission from excited state electrons coherently. Early evidence of stimulated emission in methylammonium lead trihalide perovskites was observed while studying the charge-transfer dynamics of efficient perovskite solar cells using ultrafast pump-probe spectroscopy².

Optical amplification, measured via gain per unit length (in cm^{-1}), can be studied by photoexciting the gain medium and measuring its spectral absorption over time. In perovskite thin films, optical gains have been reported¹⁷⁸ in the range $3200 \pm 800 \text{ cm}^{-1}$. This value is comparable to that of single-crystal GaAs, and agrees with the known high absorption coefficient of perovskite. Gain has been shown to be as long as 200 ps, with a threshold of $\sim 16 \mu\text{J cm}^{-2}$.

Varying the pump fluence while measuring the emitted spectral intensity profile yields the threshold for amplified spontaneous emission (ASE). Above the threshold for ASE, the luminescence spectrum greatly narrows and sharply increases in output intensity. Reported ASE thresholds range from $12 \mu\text{J cm}^{-2}$ under 150-fs excitation¹⁷⁹ to $60 \mu\text{J cm}^{-2}$ under 2 ns pumping conditions¹⁸⁰ with halide perovskites, and $7.6 \mu\text{J cm}^{-2}$ at pulse durations as long as 5 ns with the aid of a liquid crystal reflector¹⁸¹.

5.1.1 Original reports of perovskite lasing

Solution processed MAPbX₃ perovskite films were studied in the context of prospects for lasing by Xing *et. al*¹⁷⁹ (Figure 25). The transition from spontaneous emission (SE) to ASE was

observed with increasing pump fluence in a 65-nm-thick MAPbI₃ film spin-coated on a quartz substrate. Using the measured threshold fluence ($12 \pm 2 \mu\text{J cm}^{-2}$) and absorption coefficient ($\alpha = 5.7 \times 10^4 \text{ cm}^{-1}$ at 600 nm), the ASE threshold carrier density was calculated to be $\sim 1.7 \times 10^{18} \text{ cm}^{-3}$. The Auger recombination process in perovskites, which manifests under high pump fluence (nonlinear regime), typically yields Auger lifetimes from a few ps to ns, depending on the photogenerated charge carrier density. Auger recombination in MAPbI₃ is efficient ($\tau \sim 300 \text{ ps}$) compared with SE ($4.5 \pm 0.3 \text{ ns}$) because of the long-range electron-hole diffusion lengths. However, the timescale for the occurrence of ASE ($< 10 \text{ ps}$) signifies that the carrier build-up time for population inversion, and the subsequent avalanche, out-competes the Auger processes in these perovskite thin films. The low ASE threshold and the long-range balanced charge carrier diffusion length stems from the low bulk defect density in MAPbI₃ films.

The PLQY as a function of excitation fluence in CH₃NH₃PbI_{3-x}Cl_x perovskite film shown 70% at high excitation density. To exemplify the high luminescence yield of the CH₃NH₃PbI_{3-x}Cl_x perovskite, Friend and co-workers has constructed and demonstrated the operation of an optically pumped vertical cavity laser comprising a layer of perovskite between a dielectric mirror and evaporated gold top mirror¹⁰⁵.

The relation between the phase-transition of the perovskite film, and ASE mechanisms, was investigated by studying behavior in different phase states¹⁸². A sharp ASE peak with the maximum spectral intensity occurs at the temperature of 120 K. PL emission spectra show a notable variation of the spectral characteristics when moving from temperatures 120 K to 160 K. This is the temperature range in which the structural phase transition from orthorhombic to tetragonal occurs. As the temperature exceeds 120 K, the lasing threshold continues to increase because of the thermal broadening of the gain peak.

Low-threshold ASE and lasing has also been reported from 10 nm monodisperse colloidal nanocrystals of cesium lead halide perovskites CsPbX_3 ¹⁸³. Room-temperature optical amplification was obtained across the entire visible spectral range (440–700 nm) with low pump thresholds down to $5 \pm 1 \text{ mJ cm}^{-2}$ and high values of modal net gain of at least $450 \pm 30 \text{ cm}^{-1}$. Whispering-gallery-mode lasing using silica microspheres as high-finesse resonators, conformally coated with CsPbX_3 nanocrystals, as well as random lasing in films of CsPbX_3 nanocrystals, have been observed.

5.1.2 Effects of perovskite crystal structures

MAPbI_3 undergoes a reversible phase transition between its tetragonal and cubic phases at $\sim 330 \text{ K}$, and is sensitive to oxygen, moisture and heat. As a result, all-inorganic CsPbX_3 has also been explored as an optical gain medium that has the attractive properties of wide size-dependent color tunability and spectrally narrow gain profiles and ease of fabrication¹⁸³⁻¹⁸⁶.

A film consisting of close-packed CsPbBr_3 nanocrystals was photoexcited using a wavelength 400 nm in a stripe configuration. A narrower emission band located at 524.5 nm with FWHM of $\approx 5 \text{ nm}$ appears on the longer wavelength side when the pump intensity exceeds $\approx 22 \mu\text{J cm}^{-2}$. These optical gain properties in CsPbBr_3 nanocrystals suggest a material of interest in lasing, especially in the green and blue spectral range, where II–VI group quantum dots show lower gain performance than their red counterparts¹⁸⁷. Nonradiative Auger recombination occurring at high excitation intensities has been recognized to be the main channel dissipating population inversion in quantum dots, hindering optical amplification. Excitation-intensity-dependent time-resolved PL measurements were performed on CsPbBr_3 nanocrystals to explore Auger recombination¹⁸⁴. The PL decay of the CsPbBr_3 is relatively slow single-exciton recombination under low excitation

intensities ($<4.5 \mu\text{J cm}^{-2}$), then a fast decay process emerges as the excitation intensity increases, corresponding to the Auger recombination, on the ~ 100 ps timescale.

ASE in the optically-pumped FAPbI_3 and MABr -stabilized FAPbI_3 films showed an ultralow threshold of $1.6 \mu\text{J/cm}^2$. FAPbI_3 films displayed more durable lasing emission than MAPbI_3 ¹⁸⁸. The improvements in low lasing threshold and high stability in the FAPbI_3 film were reported and expected to stem from its low trap density, smooth film morphology, high thermal stability, and its excitonic emission. In contrast to polycrystalline thin films, low-dimensional single-crystals exhibit higher crystalline quality, and this may provide lower defect densities and reduced scattering that can support further threshold lowering.

The solution growth of high-quality single-crystal phase FAPbI_3 nanowires led to black-phase FAPbI_3 alloy nanowires in the cubic perovskite phase. These were made by incorporating a small amount of MABr into FAPbI_3 ¹⁸⁹. Optically pumped lasing was reported from MABr -stabilized FAPbI_3 perovskites at room temperature with near-infrared (NIR) emission at ~ 800 nm, low lasing thresholds of a few $\mu\text{J/cm}^2$, and high quality factors of ~ 1500 . These FA-based perovskite NWs displayed improved photostability and wavelength tunability compared to MA-based perovskite NWs¹⁸⁹.

Solution-processed lead-free Sn-based halide perovskites such as CsSnX_3 exhibit relatively poor photovoltaic performance¹⁹⁰⁻¹⁹³; however, they possess remarkable optical gain properties in the NIR up to $\approx 1 \mu\text{m}$. Ultralow-threshold ($\approx 6 \mu\text{J cm}^{-2}$), large-gain (200 cm^{-1}) stimulated emission from 20% SnF_2 - CsSnI_3 samples was demonstrated with performance comparable to Pb counterparts. Transient spectroscopy provides direct evidence that SnF_2 addition suppresses trap states in CsSnI_3 , and that lasing originates from free-electron-hole bimolecular recombination with a high rate of $\approx 10^{-8} \text{ cm}^3 \text{ s}^{-1}$ (*i.e.*, 1–2 orders larger than MAPbI_3). Ultrastable (>20 h), room-

temperature NIR coherent light emission (700–1000 nm) was achieved. The ASE wavelength was tuned from 700 to 950 nm by varying bromide:iodide composition to obtain CsSnBr₃, CsSnBr₂I, CsSnBrI₂, and CsSnI₃ thin films.

2D layered perovskite counterparts with natural multiple quantum well structures exhibit strong light–matter interactions and intense excitonic luminescence. However, despite such promising traits, there have been no reports of room temperature optical gain in 2D layered perovskites, a consequence of efficient nonradiative trapping of free excitons and/or biexcitons¹⁹⁴.

Recently, (OA)₂(MA)_{n-1}Pb_nBr_{3n+1} based mixed lower-dimensional perovskite layers (with larger bandgaps and smaller refractive index acting as cladding layers) provided enhanced exciton and photon confinement for higher-dimensional perovskite layers (the active layers)¹⁹⁵ (Figure 27). The achievement of low-threshold ($\sim 7.8 \mu\text{J cm}^{-2}$) lasing from near-3D to quasi-2D perovskites is related to efficient exciton localization from lower-dimensional perovskite layers to the active layers in microplatelets.

5.2 Laser cavity structures in perovskite lasers

In semiconducting nanowires, waveguiding is provided along the axial direction, and the two end facets form a Fabry–Perot cavity. The growth of high-quality single-crystal nanowires from low-temperature solution-processing of MAPbX₃ perovskites was reported by Zhu and co-workers¹⁹⁶. The perovskite nanowires exhibited low lasing thresholds (200 nJ/cm²); high quality factors ($Q \sim 3,600$); near-unity quantum yield; and broad tunability covering the near-infrared to visible wavelength region (Figure 26).

Perovskite nanoplatelets were grown on mica substrates by chemical vapor deposition and formed whispering-gallery-mode (WGM) cavities as a result of the growth procedure¹⁹⁷. Individual perovskite nanoplatelets were photoexcited using a femtosecond-pulsed laser, and a

lasing threshold of $37 \mu\text{J cm}^{-2}$ was achieved in MAPbI_3 nanoplatelets. Solution growth of MAPbBr_3 perovskite micro-disks – also a means to WGM microresonators – exhibited a quality factor of ≈ 430 ¹⁹⁸. Single-mode lasing at 557.5 nm was achieved in a $2 \times 2 \times 0.6 \mu\text{m}^3$ square micro-disk and exhibited a threshold of $3.6 \pm 0.5 \mu\text{J cm}^{-2}$. Whispering-gallery type planar perovskite nanoplatelet lasers exhibit pronounced optical gain and tunable optical modes, and offer a pathway to integration with Si technologies.

In distributed feedback (DFB) cavity structures, optical feedback is provided via Bragg scattering from an interference grating built either directly into the active medium, or in the vicinity of the resonator through periodic alternation of the refractive index. Jia *et.al.*, reported a metal-clad, second order DFB perovskite laser constructed on a silicon substrate that achieves threshold at optical pump intensities of 5 kW/cm^2 for durations $\leq 25 \text{ ns}$. The work demonstrated by use of a high thermal conductivity substrate for efficient heat rejection, establishing low threshold in an electrically accessible architecture¹⁹⁹. Saliba *et.al.*, reported perovskite DFB cavities made by nanoimprinting a corrugated structure onto a polymer template, followed by evaporation of a conformal perovskite layer²⁰⁰. Significant narrowing of the linewidth of the ASE peak was observed with increased excitation fluence, and the wavelength redshifted as the grating periodicity of the DFB cavity increased. The fluence threshold diminished from 2.1 to $0.3 \mu\text{J cm}^{-2}$ as the grating period decreased from 420 to 400 nm.

A new hybrid perovskite vertical cavity surface-emitting laser (VCSEL) was microfabricated based on a uniform perovskite thin ($\approx 300 \text{ nm}$) film placed between two high-reflectivity ($\approx 99.5\%$) distributed Bragg reflectors (DBRs)²⁰¹. This work leveraged gallium nitride semiconductor process innovations wherein a nanoporous-GaN (NP-GaN) provides the low-index layers in a NP-GaN/GaN (electrically conducting) multilayer stack. The perovskite VCSEL device

enabled the study of gain dynamics on excitation timescales that are much longer than typically reported in femtosecond experiments in the perovskite literature. VCSEL lasing output as a function of pumping fluence indicated a lasing threshold of $7.6 \mu\text{J cm}^{-2}$.

Continuous-wave (c.w.) operation of a perovskite methylammonium lead iodide (MAPbI_3)²⁰² laser was recently reported (Figure 28). Under constant blue optical photoexcitation, devices emitted near-infrared (785 nm wavelength) laser light over the course of an hour when operated at 100 K. To achieve c.w. lasing, the authors sought a strategy to dynamically generate exciton/charge-trapping sites in the material. They took advantage of the phase transition in MAPbI_3 : when cooled below 160 K, the lattice structure of MAPbI_3 changes from tetragonal to orthorhombic, with the latter having a slightly larger optical bandgap. The researchers fabricated a distributed feedback laser structure based on MAPbI_3 and cooled it to around 100 K, i.e. into its orthorhombic phase. On excitation with intense blue light ($> 17 \text{ kW cm}^{-2}$), tetragonal phase inclusions formed inside the orthorhombic lattice within a few 100 ns, presumably due to local heating.

6. Conclusions and Outlook

The efficiencies of perovskite solar cells have advanced from single digits to a certified 23.3% in less than a decade of concerted worldwide effort. The materials rely upon facile low-temperature processing. Their structural flexibility and excellent optoelectronic properties have yielded efficient LEDs as well as lasers.

In relation to applications in optical sources, one central theme in perovskite light emission has been the move from the bulk (3D) materials widely used in solar cells towards instead the application of reduced-dimensional structures. Taken together with judicious compositional engineering, this has taken perovskites across a wide range of emission wavelengths to near-unity

PLQY. The same defect-tolerance that serves these materials so well in photovoltaics is a major factor enabling their bright PL. The photostability of reduced-dimensional perovskites need to be improved as the material composed with thin flaks in solid film.

Among these reduced-dimensional perovskite emitters, colloidally-synthesized nanometer-scale nanocrystals have shown excellent quantum yield, and have the further benefit that they combine readily with other classes of solution-processed materials such as polymers and small molecules to produce composites with enhanced optical and electronic functionalities. To bring the high PLQY nanocrystals and apply them successfully in displays, it is of interest to identify Pb-free materials that exhibit the same excellent emission properties. Options based upon Sn, Ge, Cu, Bi, and Sb have been explored, but lead-free perovskites today perform well below Pb-based device levels. Accelerated computational-experimental approaches could potentially contribute to addressing this important challenge.

Given the soft nature of the hybrid perovskite materials, their stability against moisture, heat, oxygen and electric field will continue to be an area of intense activity. Here the versatile chemistry of hybrid organic-inorganic perovskites will be leveraged on the path to further progress. Recent advances on this front are encouraging, including operating stability of 1,000 hours under 1 sun illumination. Integrated encapsulation strategies have increased stability against external humidity and heat. Compared with solar cells, though, LEDs still rely on charge injection rather than extraction; and also see higher fields in light of the > 3 V often used to drive devices. In sum, further progress in enhancing considerable the operational stability of perovskite LEDs is urgently needed.

Progress in perovskite LEDs has been uneven as a function of emission wavelength: the EQE in the green rapidly exceeded 20%^{39,129,203,204}, but in the blue emission resides in the 3% and below

range²⁰⁵. Recent reports of blue luminescence quantum yields of 80%²⁰⁶ are certainly encouraging, but such materials need to be married with enhanced carrier transport and suitable interlayer band alignment to translate into high device performance. Exploring highly emissive, stable and conductive blue emitting perovskite materials is thus an urgent mandate for the field.

On lasing, room-temperature CW performance is a next frontier. Perovskite single crystals exhibit further slowing of Auger recombination and lower thresholds, giving encouragement on this path. This indicates promise for perovskite lasers with reduced heat generation under the required high-power continuous-wave optical pumping. Electrically-driven lasing is a next challenge after that. A high-quality gain medium with slow Auger recombination pathways at the carrier density levels required for population inversion is first required. Electrical excitation demands high charge carrier mobilities as well as improved thermal stability, a large gain cross-section at the lasing wavelength, and sharp band tails marked by a low Urbach energy. Perovskites have shown encouraging properties on many of these fronts, except that thermal stability and carrier mobility will likely need further improvement.

Table 1. Comparison of perovskite LED, QD LED and OLEDs.

	PeLEDs	QD LEDs	OLEDs
FWHM (nm)	~20	~28	>70
ELQY ^{red} (%)	13 ²⁰⁷	20.5 ¹⁴⁶	29 ²⁰⁸
L _{max} ^{red} (cd/m ²)	82Wsr ⁻¹ m ⁻² 39	42,000 ¹⁴⁶	1,000,000 ²⁰⁸
ELQY ^{green} (%)	14 ²⁰⁹	14.5 ²¹⁰	73,100 ²¹¹
L _{max} ^{green} (cd/m ²)	9120 ²⁰⁹	10,000 ²¹⁰	27.5 ²¹¹
ELQY ^{blue} (%)	1.5 ²⁰⁵	10.7 ²¹⁰	36.7 ²¹²
L _{max} ^{blue} (cd/m ²)	2480 ²⁰⁵	4,000 ²¹⁰	10,000 ²¹²
Operational stability (h)	10 ²¹³	100,000 ¹⁴⁶	600,000 ²¹⁴
Color tunability	400 nm ~ near IR		400 nm~700nm

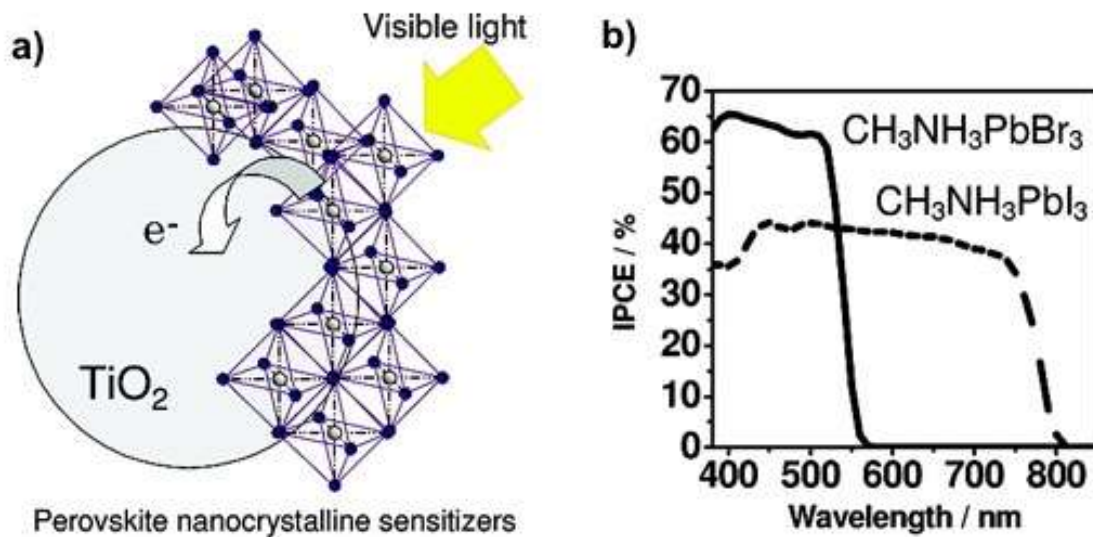


Figure 1. Perovskites a) sensitizers of TiO_2 in solid-state dye-sensitized solar cells. b) Internal power conversion efficiency spectra of $\text{CH}_3\text{NH}_3\text{PbBr}_3$ and $\text{CH}_3\text{NH}_3\text{PbI}_3$ ¹. Reproduced from ref 1. Copy right 2009, American Chemical Society.

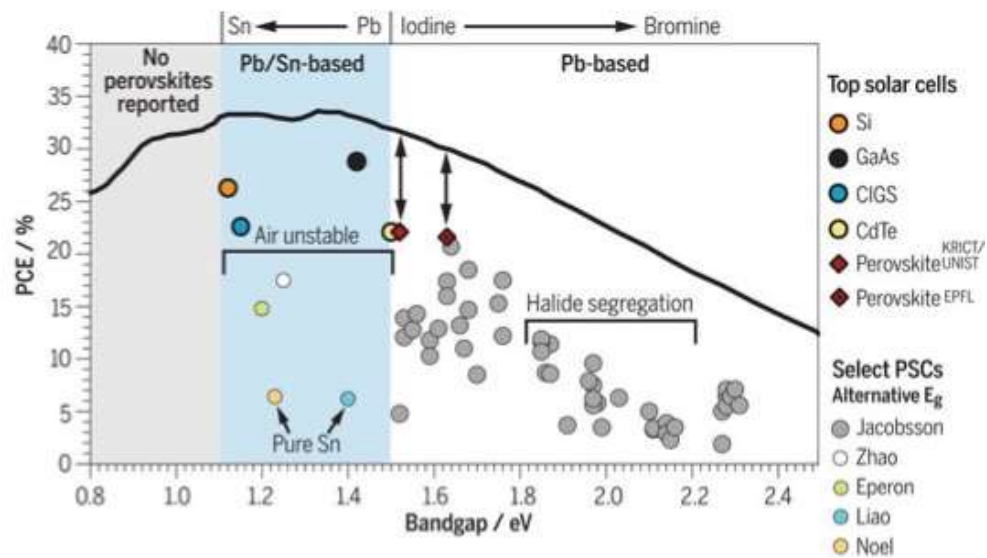


Figure 2. State-of-art perovskite solar cell efficiencies as a function of bandgap energy²¹⁵.

Reprinted with permission from ref 215. Copy right 2017, AAAS.

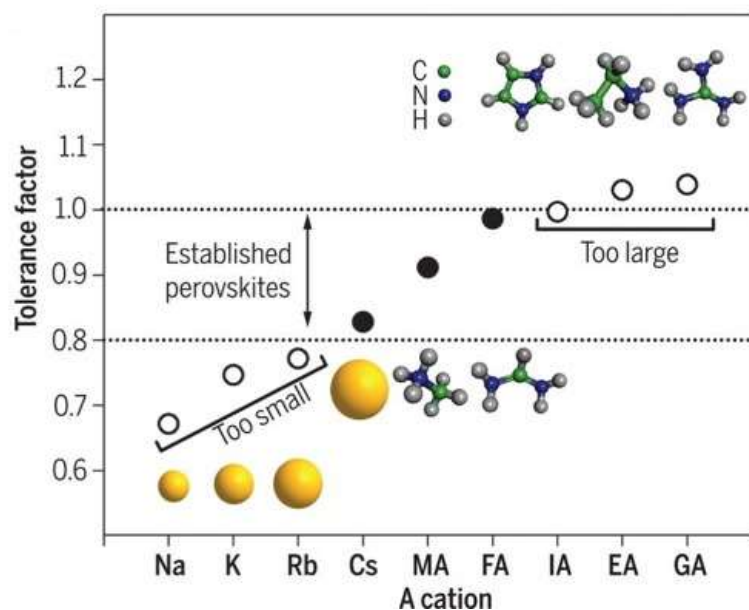


Figure 3. Tolerance factor of APbI₃ perovskite with A cations that are too small (Na, K, Rb); are widely utilized (Cs, MA, FA); or too large [imidazolium (IA), ethylamine (EA), guanidinium (GA)]. The inset images depict the cation structures. Empirically, perovskites with a tolerance factor between 0.8 and 1.0 (dotted lines) show a photoactive black phase (solid circles) as opposed to non-photoactive phases (open circles). Rb is very close to this limit, making it a candidate for modification of the perovskite lattice via a multi cation approach²¹⁶. Reprinted with permission from ref 216. Copy right 2016, AAAS.

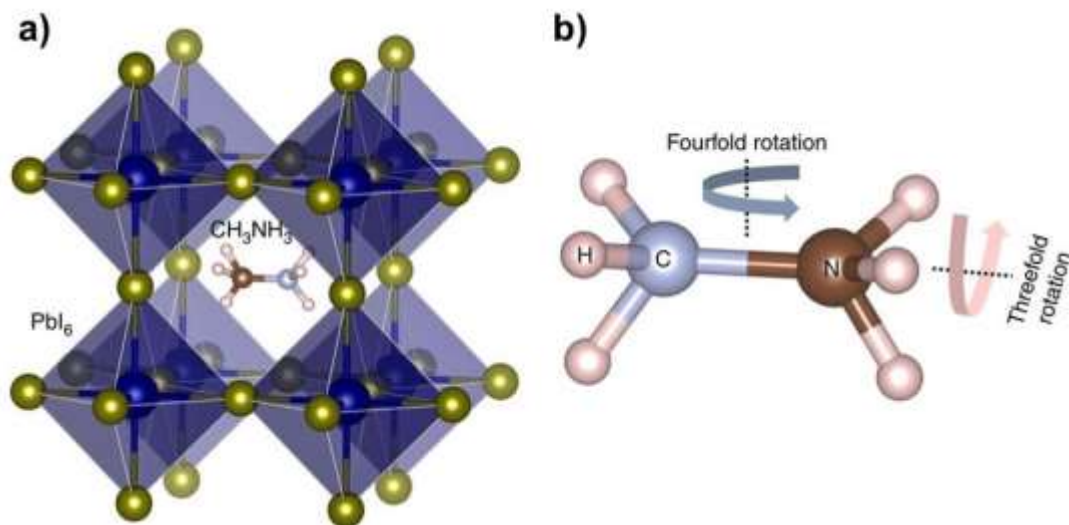


Figure 4. a) Schematic of the perovskite crystal structure. The organic cation is located in the centre of PbI₆ octahedral cage. Actual structures also reflect orientational disorder of organic cations. b) Geometry of methylammonium illustrating threefold and fourfold jumping rotational modes²¹⁷. Reprinted with permission from ref 217. Copy right 2017, Nature Publishing Group.

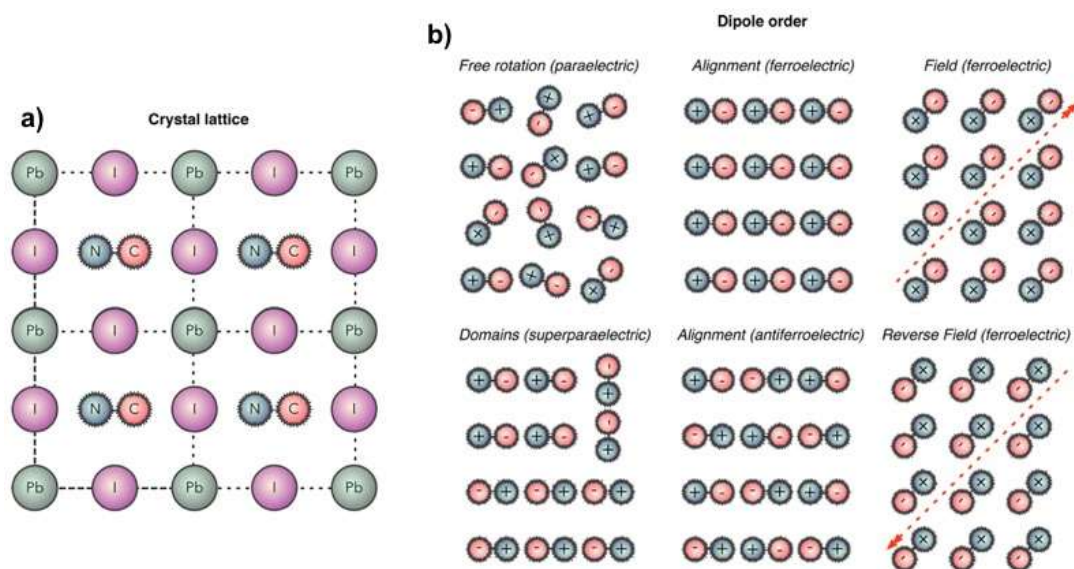


Figure 5. Schematic perovskite crystal structure of MAPbI_3 a), and the possible orientations of molecular dipoles within the lattice b). MA has an associated molecular dipole of 2.3 D, distinguishing it from spherical / symmetric cations in inorganic perovskites such as CsSnI_3 ¹⁴.

Reproduced from ref 14. Copy right 2014, American Chemical Society.

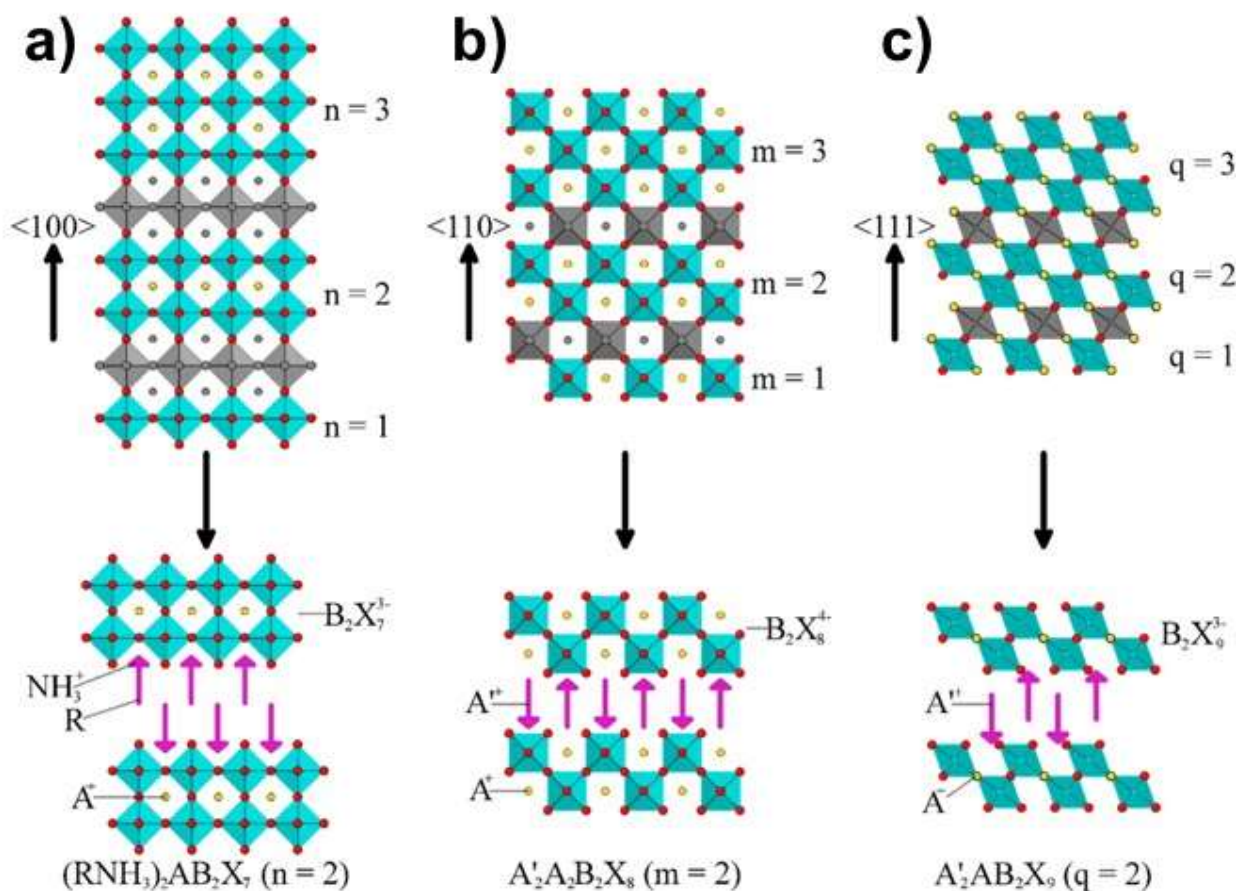


Figure 6. Lower dimensional organic–inorganic perovskites obtained from different cuts of the 3D perovskite structure. a) The family of $\langle 100 \rangle$ -oriented layered perovskites with a general formula of $(\text{RNH}_3)_2\text{A}_{n-1}\text{B}_n\text{X}_{3n+1}$ are obtained by taking n layers from along the $\langle 100 \rangle$ direction of the parent structure. b) Cuts along the $\langle 110 \rangle$ direction of the 3D perovskite structure provide the $\langle 110 \rangle$ -oriented family, $\text{A}'_2\text{A}_m\text{B}_m\text{X}_{3m+2}$, which includes 1D chain ($m = 1$) and 2-D layered ($m > 1$) members. c) The $\langle 111 \rangle$ -oriented family, $\text{A}'_2\text{A}_{q-1}\text{B}_q\text{X}_{3q+3}$, is formed by excising along the $\langle 111 \rangle$ direction of the 3-D parent, and features 0-D isolated cluster ($q = 1$) and 2-D layered ($q > 1$) members. In each of these layered structures, the perovskite framework is separated by a layer of typically larger organic cations²¹⁸. Reproduced from ref 218. Copy right 2016, American Chemical Society.

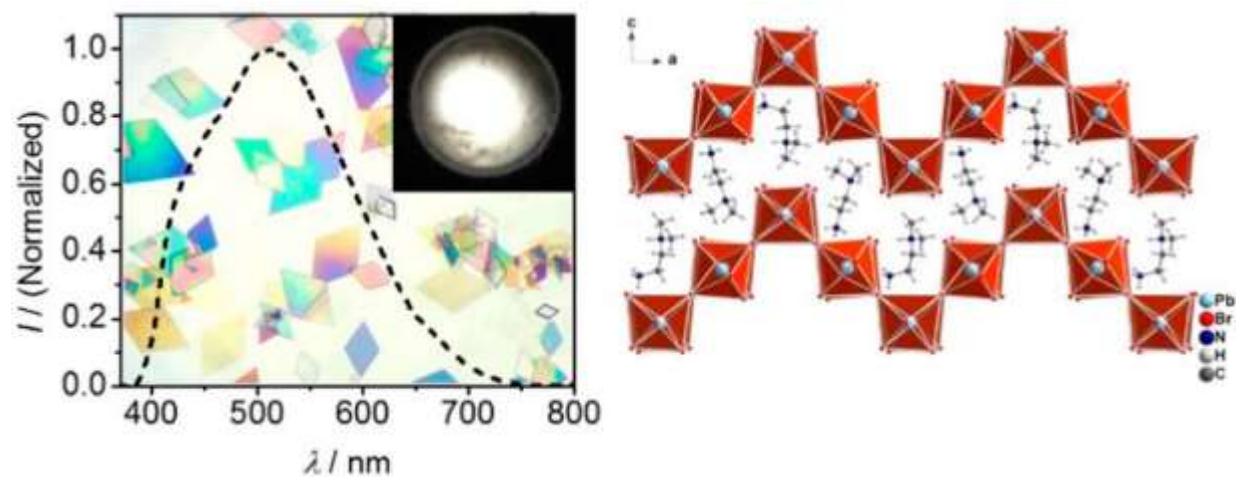


Figure 7. Structural distortion induced 0D perovskites with white light emission ²¹⁹. Reproduced from ref 219. Copy right 2017, American Chemical Society.

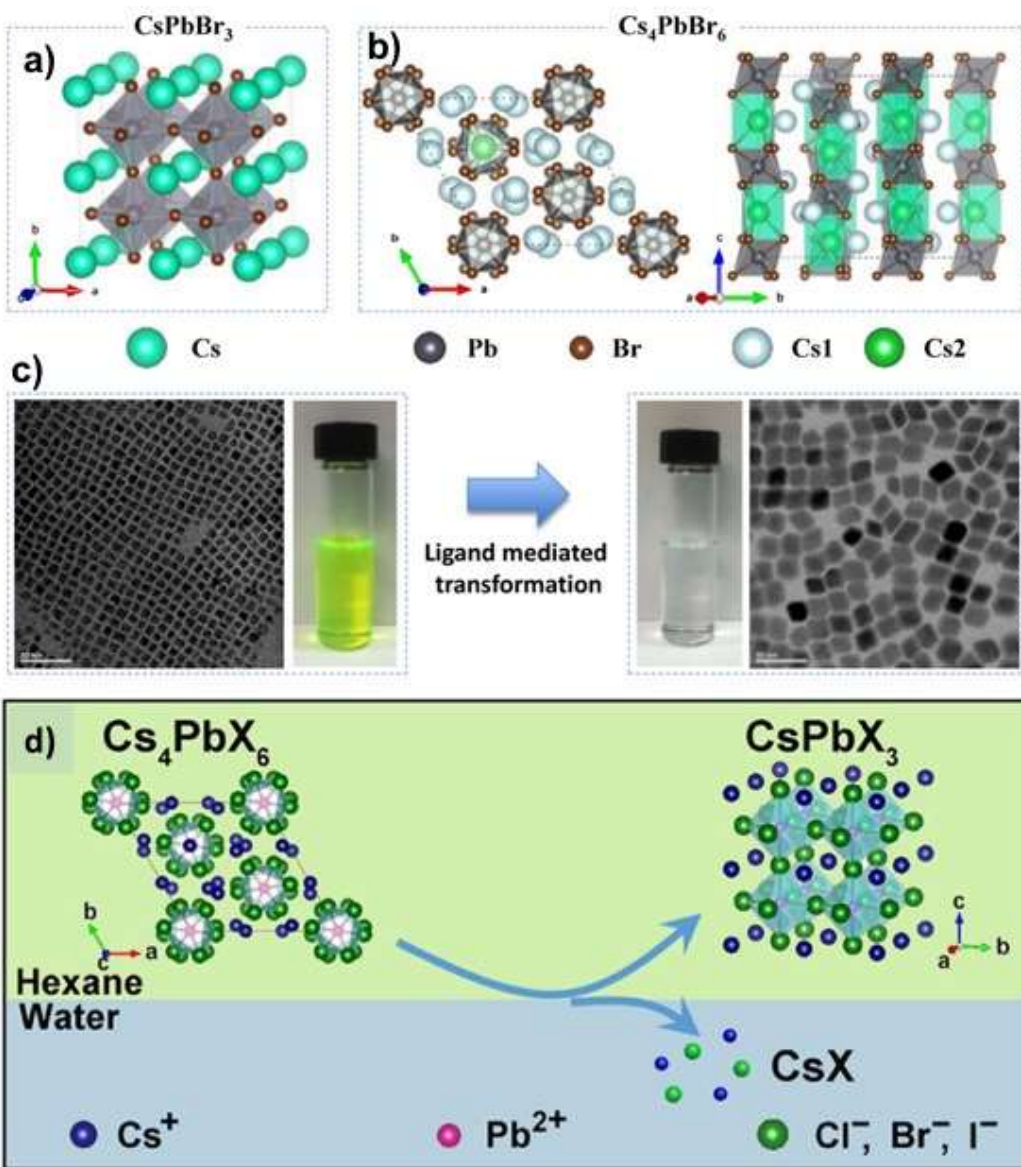


Figure 8. Schematic crystal structure of a) CsPbBr_3 and 0D Cs_4PbBr_6 (b) along and perpendicular to c axis. c) Typical TEM image of CsPbBr_3 and Cs_4PbBr_6 nanocrystals, and images of nanocrystals dispersed in hexane⁵⁷. Reproduced from ref 57. Copy right 2017, American Chemical Society. d) Schematic illustration of crystal structure change and transformation process from Cs_4PbX_6 to CsPbX_3 after water treatment⁵⁵. Reproduced from ref 55. Copy right 2017, American Chemical Society.

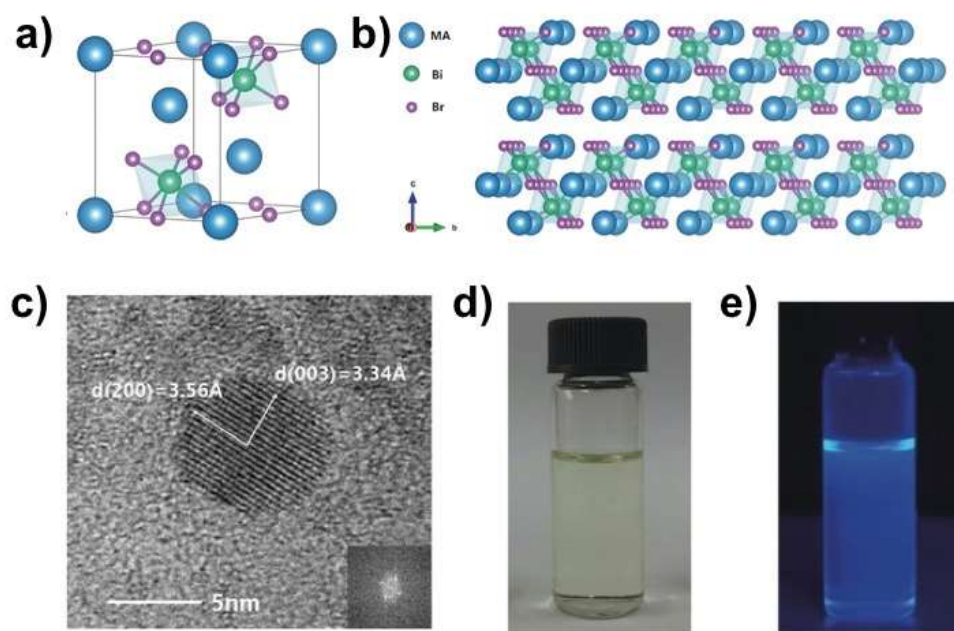


Figure 9. a, b) Schematic structure of single-crystalline $\text{MA}_3\text{Bi}_2\text{Br}_9$, c) HRTEM image of $\text{MA}_3\text{Bi}_2\text{Br}_9$ nanocrystal, d) photograph images of dispersed nanocrystals in solution and e) illuminated under UV light⁷². Reprinted with permission from ref 72. Copy right 2016, Wiley-VCH.

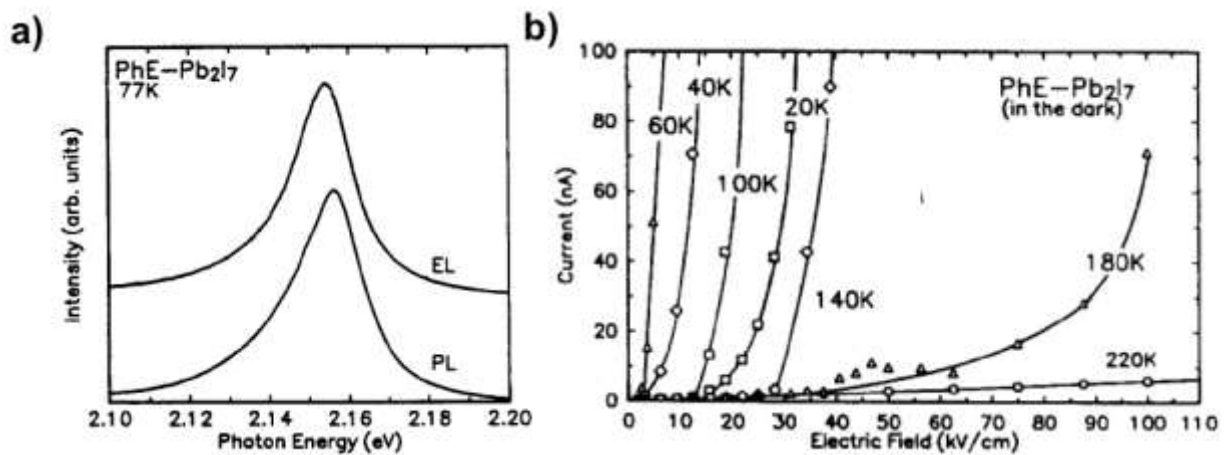


Figure 10. a) Electroluminescence and photoluminescence spectra of perovskite LEDs with $n=2$ layered perovskites. b) Current along the well plane as function of electric field for PhE-Pb₂I₇ perovskite at different temperatures³⁵. Reprinted with permission from ref 35. Copyright 1992, Elsevier.

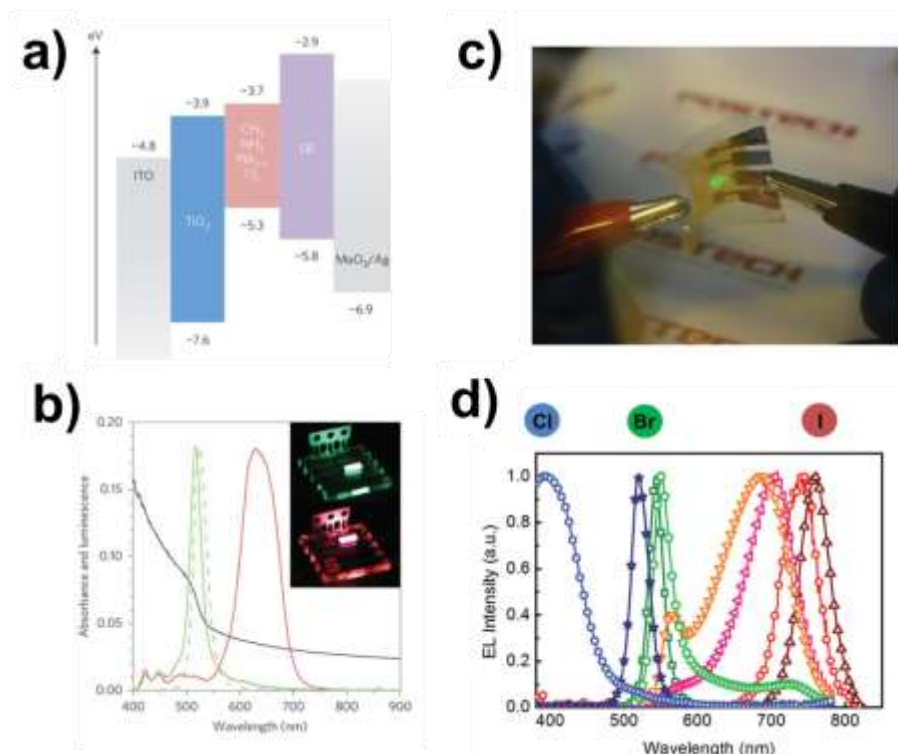


Figure 11. a) Device architecture of $\text{CH}_3\text{NH}_3\text{PbI}_{3-x}\text{Cl}_x$ perovskite LEDs. b) Normalized electroluminescence spectrum of $\text{CH}_3\text{NH}_3\text{PbBr}_2\text{I}$ mixed halide perovskite is shown in red. Inset image: Uniform green and red electroluminescence from ITO/PEDOT:PSS/ $\text{CH}_3\text{NH}_3\text{PbBr}_3$ /F8/Ca/Ag and ITO/PEDOT:PSS/ $\text{CH}_3\text{NH}_3\text{PbBr}_2\text{I}$ /F8/Ca/Ag perovskite LEDs, respectively¹¹. Reprinted with permission from ref 11. Copy right 2014, Nature Publishing Group. c) Photograph of flexible green-emitting perovskite LEDs on PET substrate during bending. d) Electroluminescence spectra of perovskite LEDs with $\text{CH}_3\text{NH}_3\text{PbCl}_x\text{Br}_y\text{I}_{3-x-y}$ ¹⁰⁹. Reprinted with permission from ref 109. Copy right 2015, Wiley-VCH.

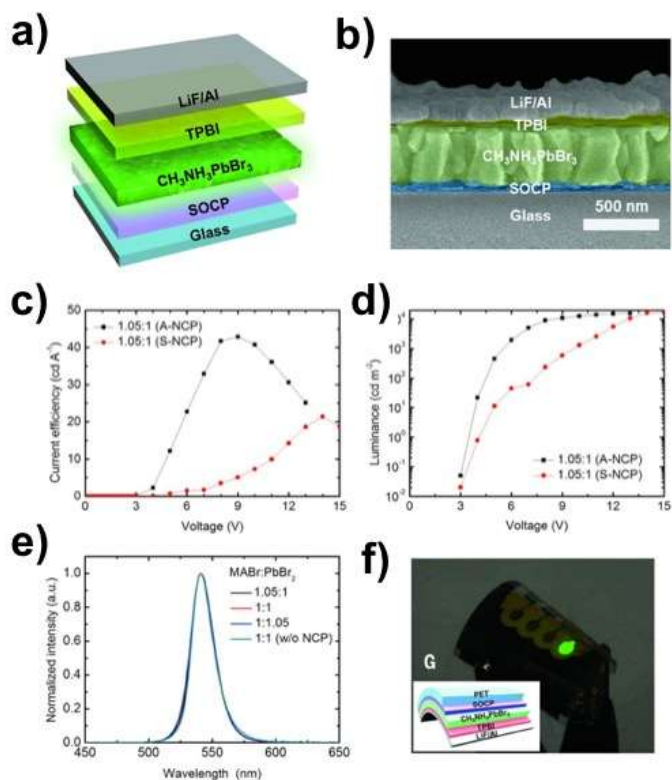


Figure 12. a) Device structure of perovskite LEDs and b) cross-sectional SEM image of perovskite LEDs. c, d) current efficiency and luminance efficiency as a function of voltage in perovskite LEDs based on grainsized controlled MAPbBr₃. e) EL spectra of perovskite LEDs. f) photograph of a flexible perovskite LEDs, and (g) its device structure¹². Reprinted with permission from ref 12. Copy right 2015, AAAS.

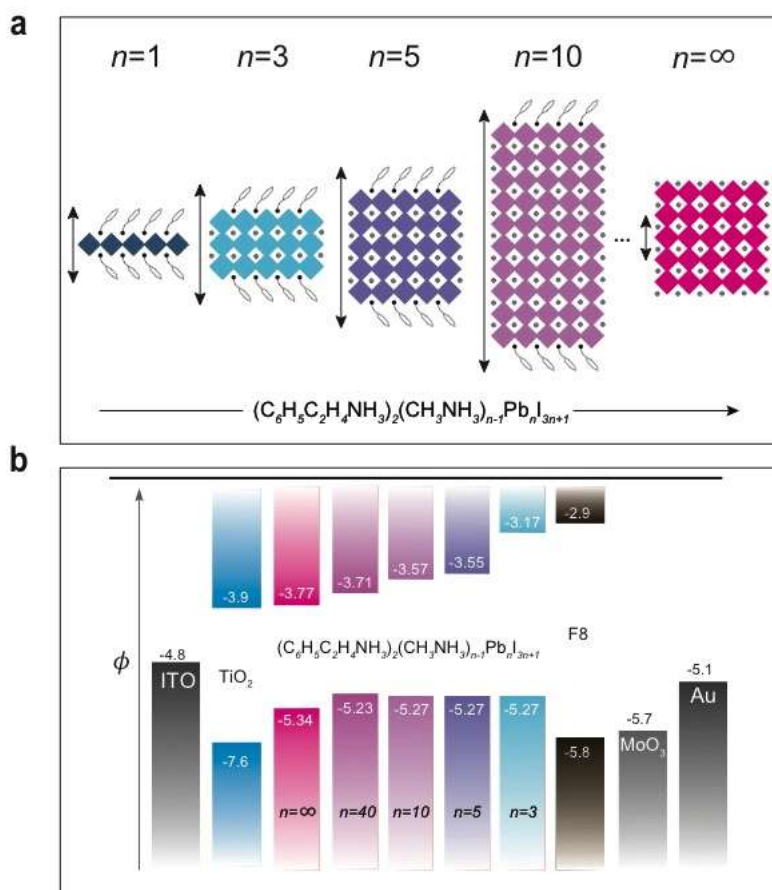


Figure 13. Unit cell structure of $(\text{C}_8\text{H}_9\text{NH}_3)_2(\text{CH}_3\text{NH}_3)_{n-1}\text{Pb}_n\text{I}_{3n+1}$ perovskites with different $\langle n \rangle$ values, showing the evolution of dimensionality from 2D ($n = 1$) to 3D ($n = \infty$). b, Electronic bandstructure of perovskites with different $\langle n \rangle$ values, combined with the band structure of ITO, TiO_2 , F8, MoO_3 and the Au electrode. ϕ , electric potential³⁷. Reprinted with permission from ref 37. Copy right 2016, Nature Publishing Group.

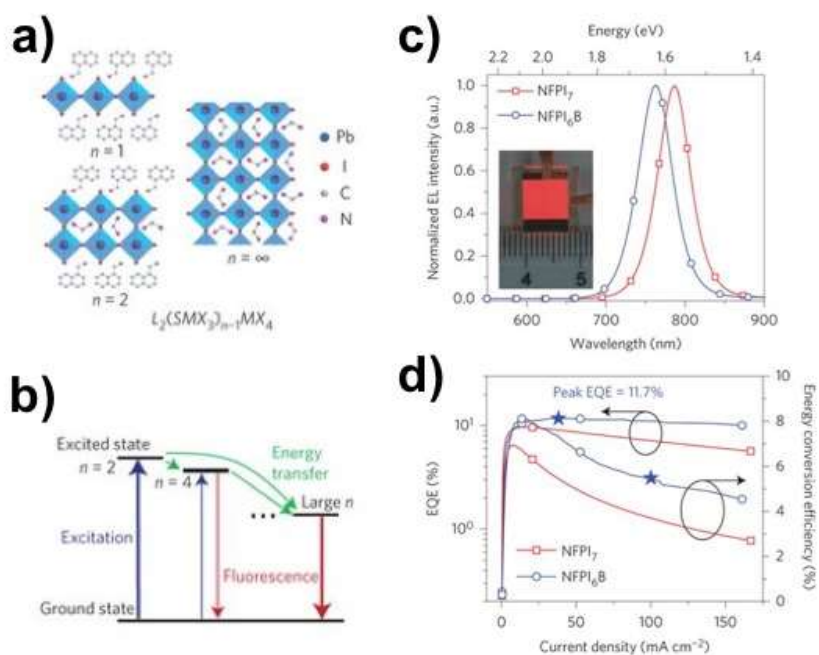


Figure 14. a) Schematic representation of layered lead halide perovskites with $n = 1$, $n = 2$ and $n = \infty$. b) Schematic of cascade energy transfer in multi-quantum well perovskites. Excitation energy is transferred downhill from smaller- n quantum wells to larger- n quantum wells, and the emission is mainly from larger- n quantum wells c), EL spectra of the devices under 3 V. Inset, photograph of a 64 mm² NFPI₆B device. d) EQE and energy conversion efficiency versus current density³⁹. Reprinted with permission from ref 39. Copy right 2016, Nature Publishing Group.

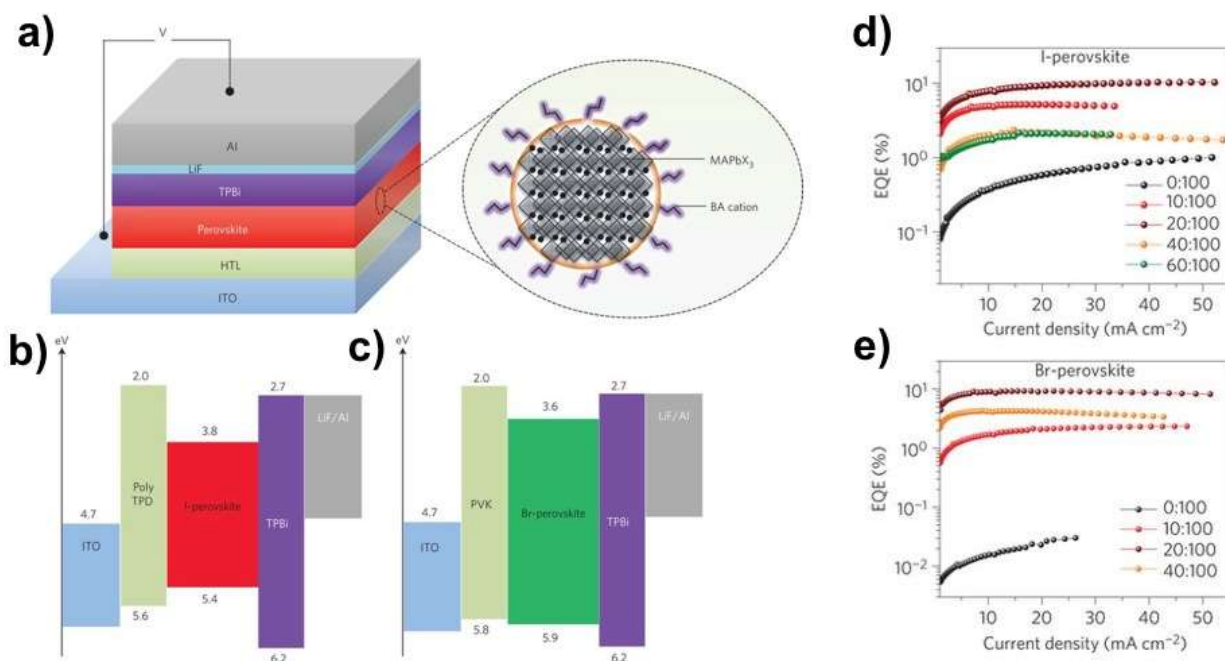


Figure 15. a) Device structure of perovskite LEDs with a nanometre-sized grain with BA cations decorating its surface. b, c) Energy diagram of I-perovskite and Br-perovskite LEDs. d) Device performance of I-perovskite LEDs with different BAI:MAPbI₃ molar ratios. e) Device performance of Br-perovskite LEDs with different BABr:MAPbBr₃ molar ratios³⁸. Reprinted with permission from ref 38. Copy right 2016, Nature Publishing Group.

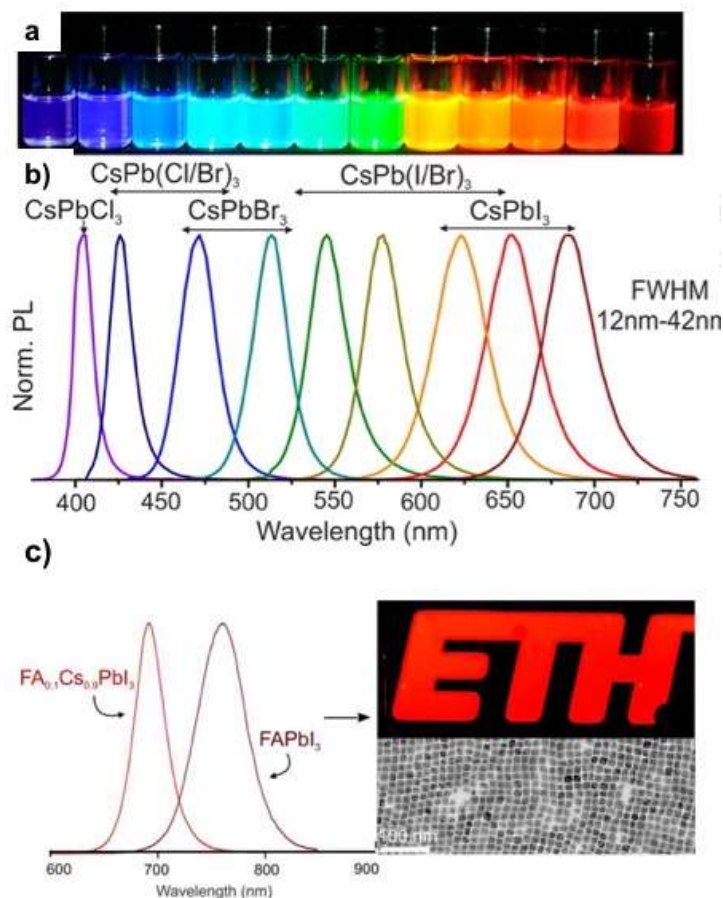


Figure 16. a) Colloidal perovskite nanocrystal solutions in toluene, under UV lamp ($\lambda = 365$ nm), b) representative PL spectra of different halide perovskite nanocrystals¹¹⁷. Reproduced from ref 117. Copy right 2015, American Chemical Society. c) Electroluminescence from $\text{FA}_{0.1}\text{Cs}_{0.9}\text{PbI}_3$ and FAPbI_3 perovskite nanocrystals²²⁰. Reproduced from ref 220. Copy right 2017, American Chemical Society.

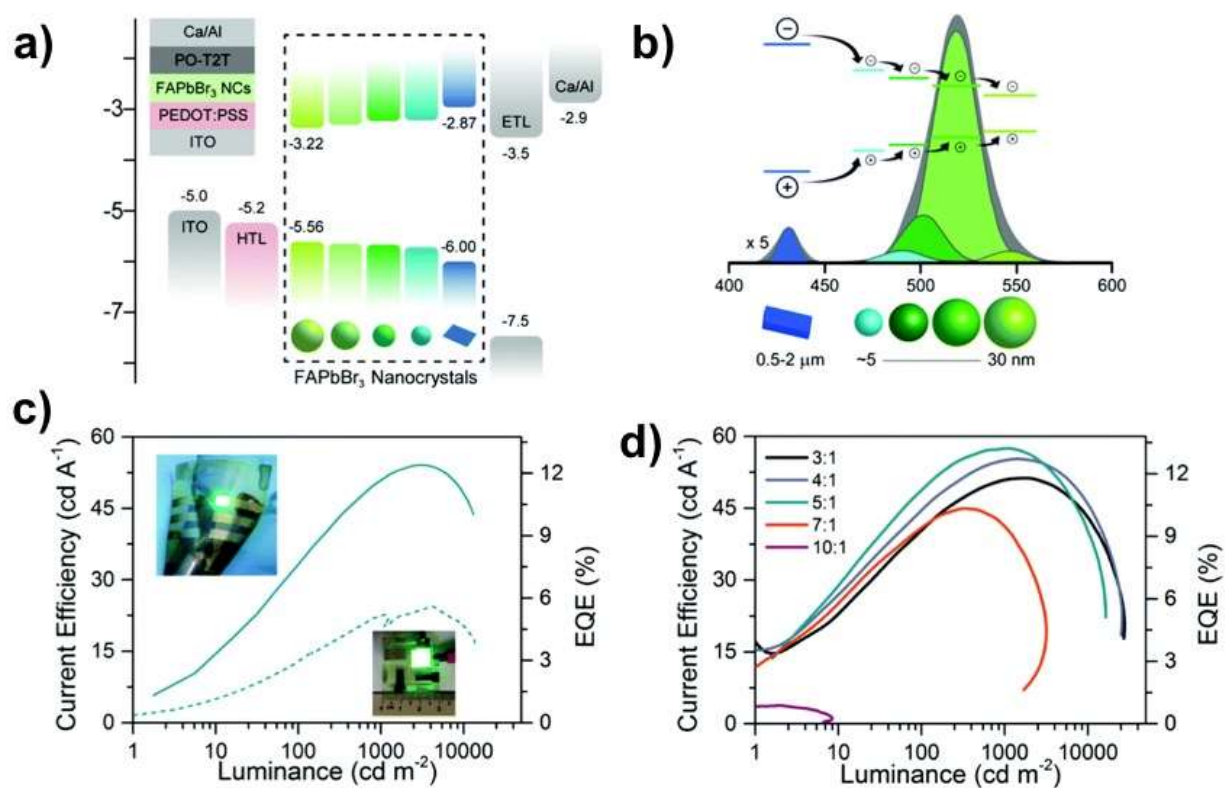


Figure 17. a) Band diagram of perovskite nanocrystal LEDs with energy cascade materials. b) The energy cascade from 2D microplatelets to FAPbBr₃ nanocrystals of graded size, where the deconvolution of the steady-state PL spectrum clearly displays the different PL contribution at varying nanocrystal sizes. c) Current efficiency/EQE versus luminance of flexible (3 mm²) and large area (95.2 mm²) LED devices. d) Characteristic current efficiency/EQE versus luminance¹²⁶. Reprinted with permission from ref 126. Copy right 2018, Royal Society of Chemistry.

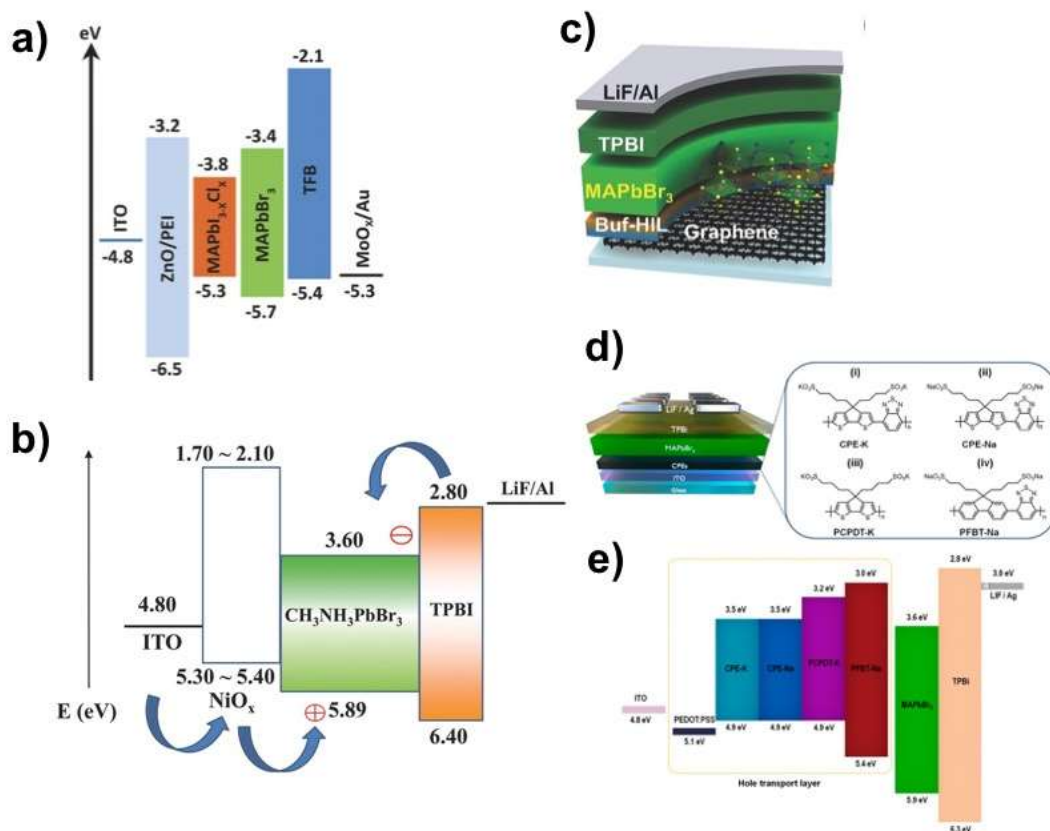


Figure 18. a) Flat-band energy level diagram of perovskite LEDs using modified ZnO using PEI¹²⁸. Reprinted with permission from ref 128. Copy right 2015, Wiley-VCH. b) Energy diagram of perovskite devices using NiO_x as a HIL²²¹. Reprinted with permission from ref 221. Copy right 2016, Wiley-VCH. c) Device structure of perovskite LED with graphene electrode and MAPbBr₃ emitter²²². Reprinted with permission from ref 222. Copy right 2017, Wiley-VCH. d) Schematic illustrations of perovskite LED devices with various conjugate polymers as HIL and e) related energy diagrams¹³⁵. Reproduced from ref 135. Copy right 2018, American Chemical Society.

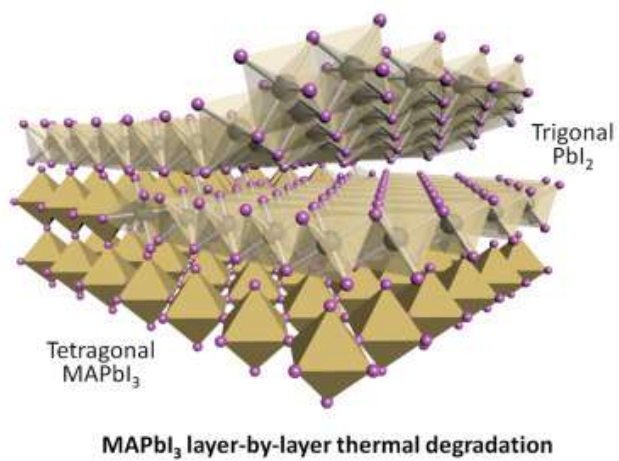


Figure 19. Structural degradation in MAPbI₃²²³. Reprinted with permission from ref 223. Copyright 2017, Wiley-VCH.

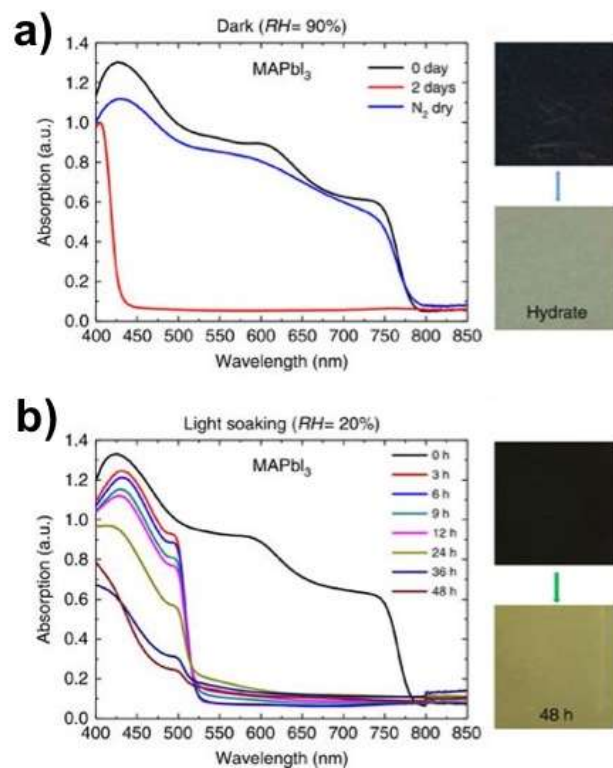


Figure 20. Hydration and light-induced degradation of perovskite materials. a) Absorption spectra and pictures of the MAPbI₃ perovskite film. Time evolution of absorption spectra and pictures of MAPbI₃ (h) before and (i) after degradation under light soaking at 20% RH¹⁵⁸. Reprinted with permission from ref 158. Copy right 2016, Nature Publishing Group.

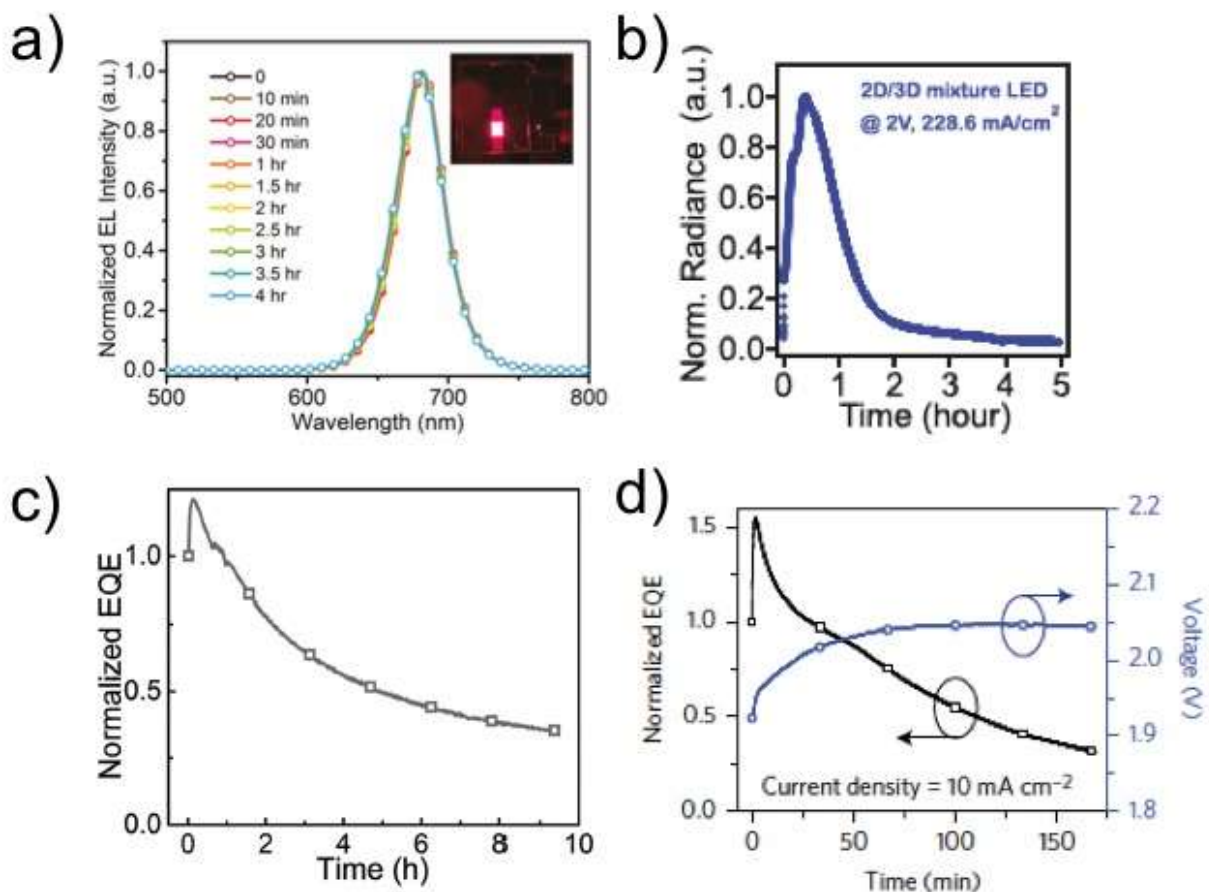


Figure 21. a) Perovskite LED spectral stability¹⁷⁶ and b-d) device operational stability under constant bias^{39,114,224}. Reprinted with permission from ref 176. Copy right 2018, Wiley-VCH. Reprinted with permission from ref 39. Copy right 2018, Wiley-VCH. Reprinted with permission from ref 114. Copy right 2016, Nature Publishing Group. Reprinted with permission from ref 224. Copy right 2017, Wiley-VCH.

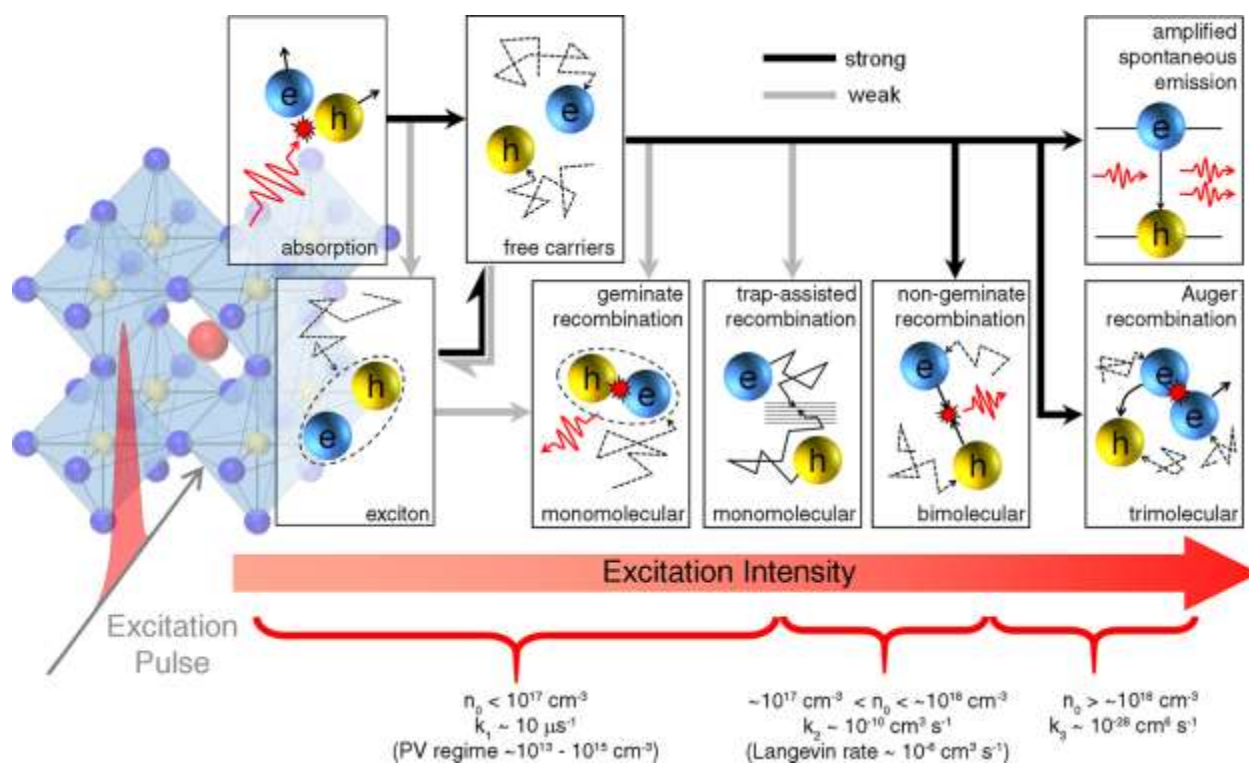


Figure 22. Photophysical processes and recombination rates in MAPbI₃ over a range of photoexcited carrier densities, n_0 . The background schematic shows the typical MAPbI₃ perovskite structure²²⁵. Reproduced from ref 225. Copy right 2016, American Chemical Society.

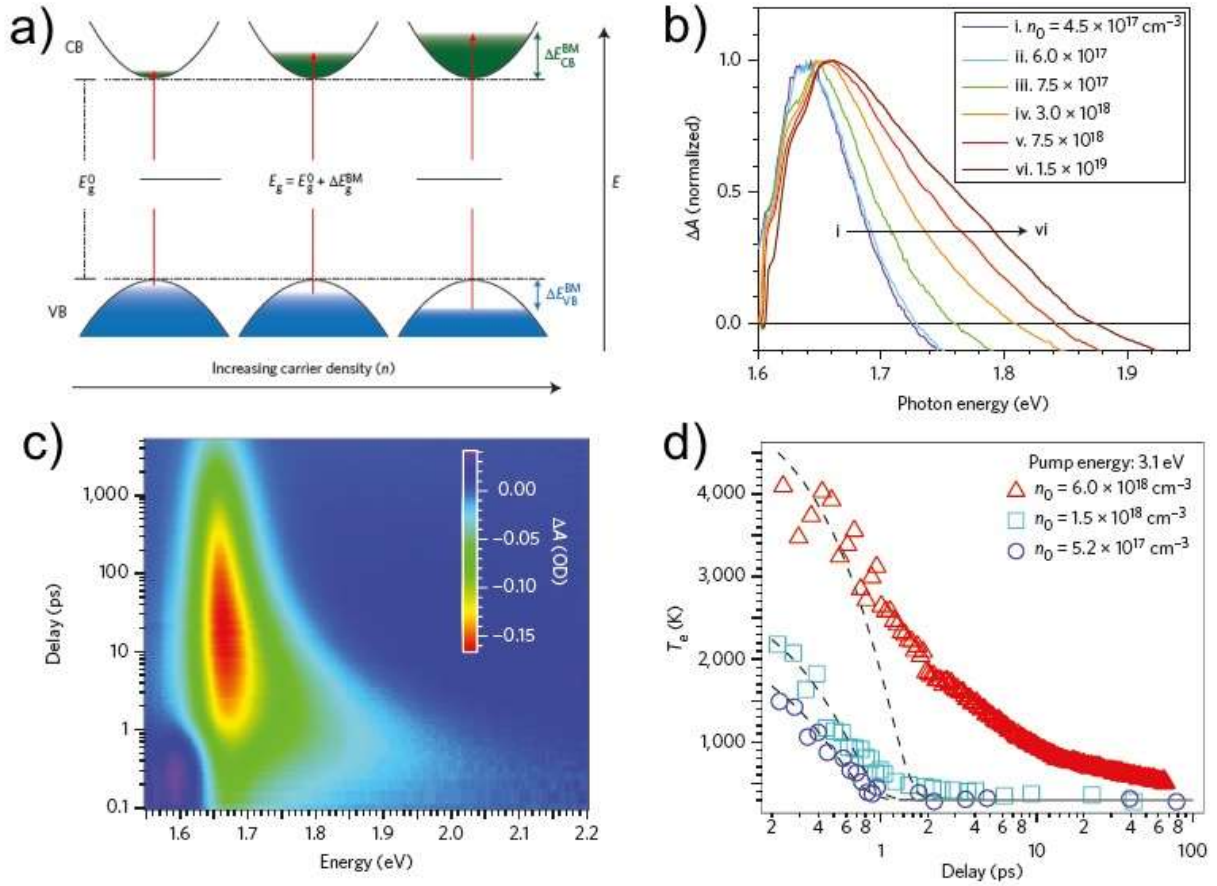


Figure 23. a) The Burstein–Moss effect, showing contributions from both electrons in the conduction band (CB) and holes in the valence band (VB) due to their similar effective masses in MAPbI₃ perovskites⁷⁷. Reprinted with permission from ref 77. Copy right 2014, Nature Publishing Group. b) Normalized transient absorption spectra of the band-edge transition in MAPbI₃ recorded at the maximum bleach signal (5 ps) after 387 nm pump excitation of varying intensity⁷⁷. c) Pseudocolour representation TA spectra shows hot carrier thermalization in MAPbI₃⁸⁵. Reprinted with permission from ref 85. Copy right 2015, Nature Publishing Group. d) Time-dependent T_e with the same n_0 but varying $\hbar\omega_{\text{pump}}$, dashed lines are calculated cooling curves⁸⁵. Reprinted with permission from ref 85. Copy right 2015, Nature Publishing Group.

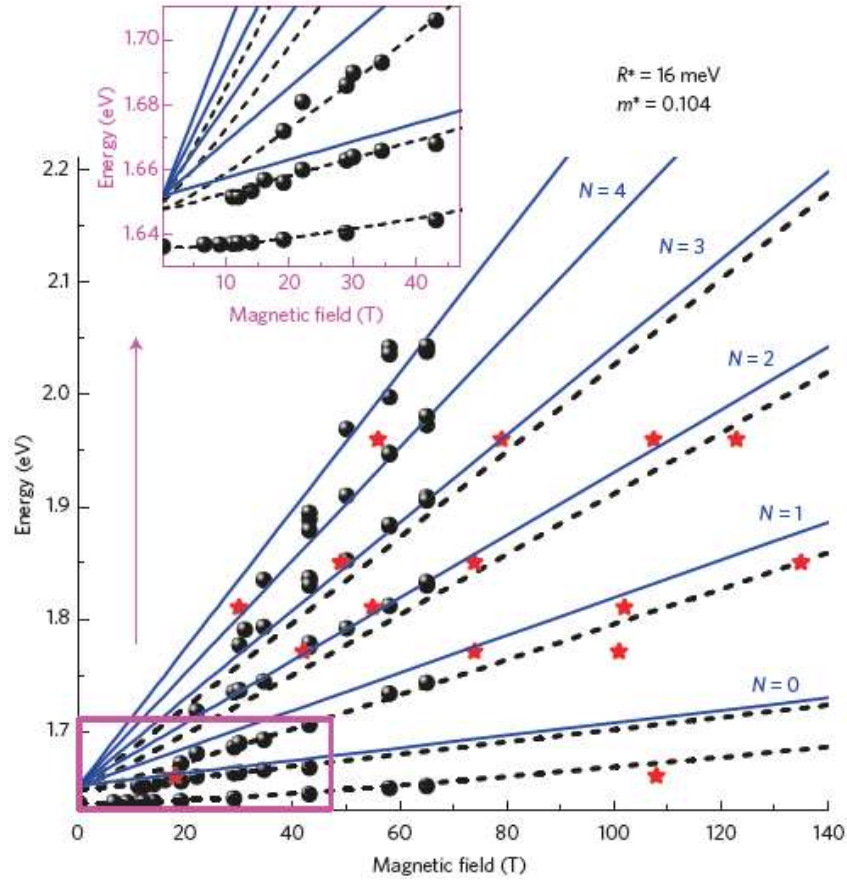


Figure 24. Full fan using data from long-pulse fixed-field spectra (black circles) and fixed-energy fast-field-sweep data (red stars). The calculated transition energies are shown for the free-electron and hole levels (solid lines) and the excitonic transitions (dashed lines). Inset to a, lower fields measured using fixed-field spectra⁹⁴. Reprinted with permission from ref 94. Copy right 2015, Nature Publishing Group.

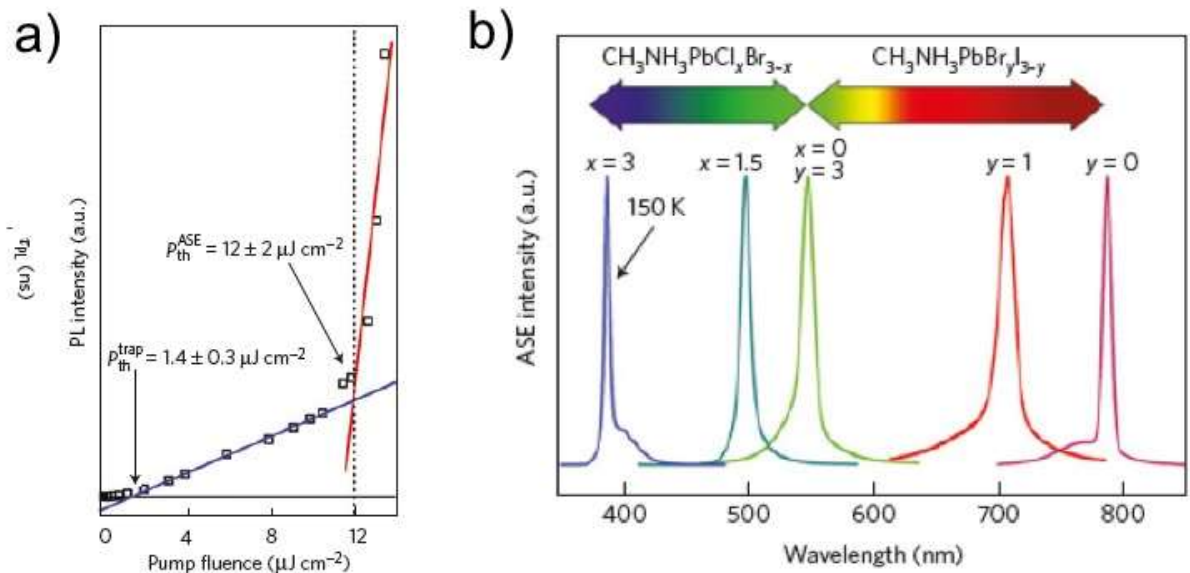


Figure 25. a) PL intensity of MAPbI_3 film as a function of pump fluence. The arrows indicate the trap state saturation threshold fluence and the ASE threshold fluence. The blue and red lines represent the linear fits to experimental data in the two linear regimes of SE and ASE, respectively. b) Wide wavelength tunability of ASE wavelengths from low-temperature solution-processed organic–inorganic halide perovskite films fabricated by mixing the precursor solutions¹⁷⁹. Reprinted with permission from ref 179. Copy right 2014, Nature Publishing Group.

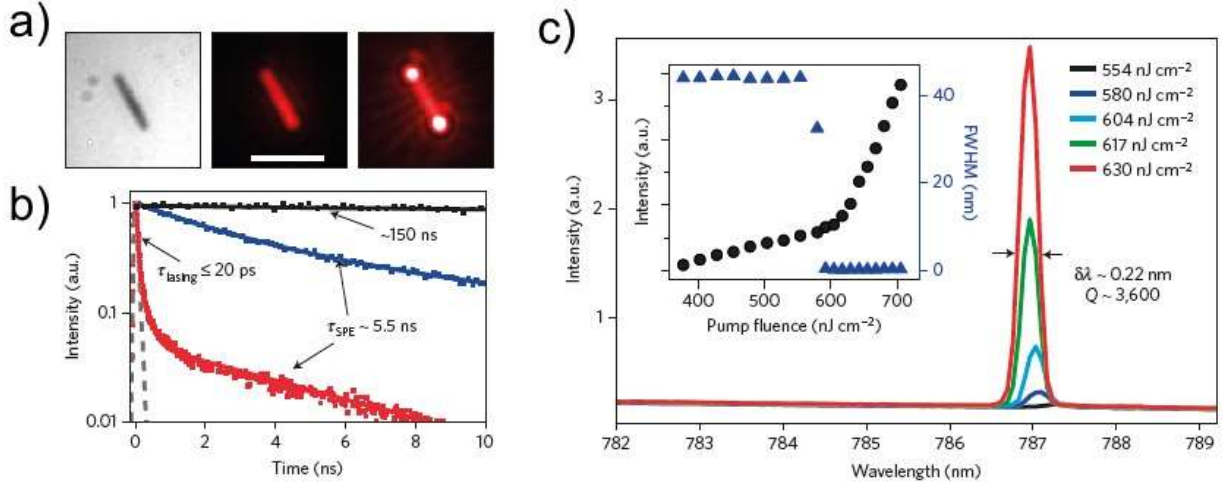


Figure 26. a) Image of single nanowire (NW) with a length of 8.5 μm . The middle and right images show the NW emission (scale bar, 10 μm). The emission is uniform below P_{Th} but mostly comes from the two end facets with coherent interference under lasing operation. b) TRPL decay kinetics after photoexcitation with fluence below ($P \sim 0.85P_{\text{Th}}$, blue) and above ($P \sim 1.1P_{\text{Th}}$, red) the threshold, showing a 5.5 ns SPE decay process below P_{Th} and a 20 ps lasing process above P_{Th} . c) NW emission spectra around the lasing threshold. Inset: Integrated emission intensity and FWHM as a function of P showing the lasing threshold at $\sim 600 \text{ nJ cm}^{-2}$. The FWHM of the lasing peak at 630 nJ cm^{-2} is 0.22 nm, corresponding to a Q factor $\sim 3,600$ ¹⁹⁶. Reprinted with permission from ref 196. Copy right 2015, Nature Publishing Group.

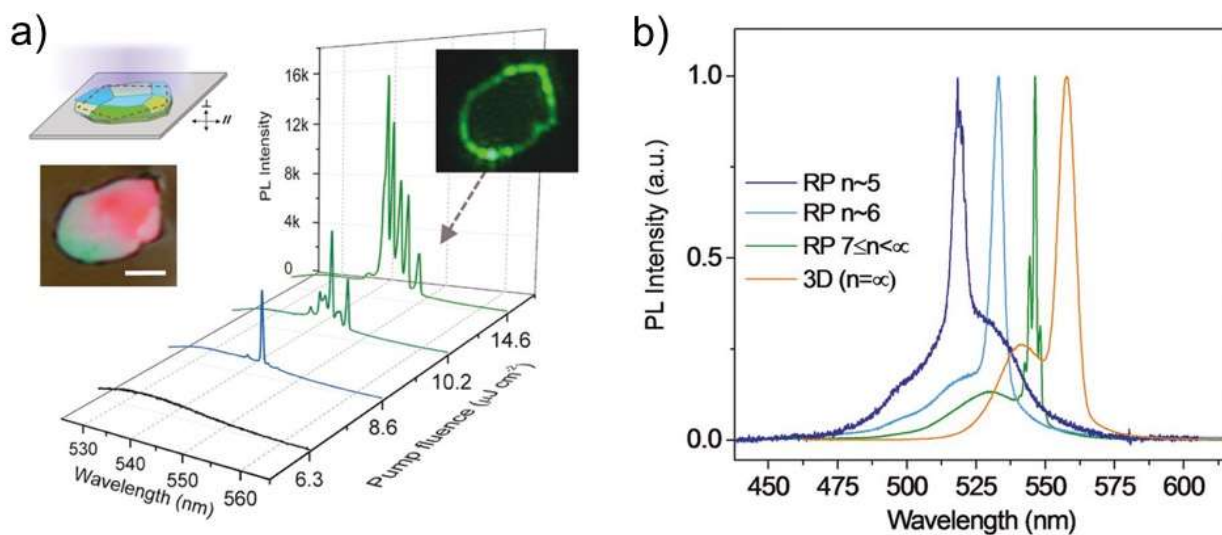


Figure 27. a) Lasing from a single low-dimensional perovskite microplate. Pump-fluence-dependent PL spectra of a single microplate. Left inset: Optical image, scale bar: 5 μm , and schematic illustration of lasing measurements of microplate on a substrate pumped by a 400 nm laser excitation (≈ 150 fs, 1 kHz). b) Normalized lasing spectra from 3D perovskite film to quasi-2D perovskite microplates¹⁹⁵. Reprinted with permission from ref 195. Copy right 2018, Wiley-VCH.

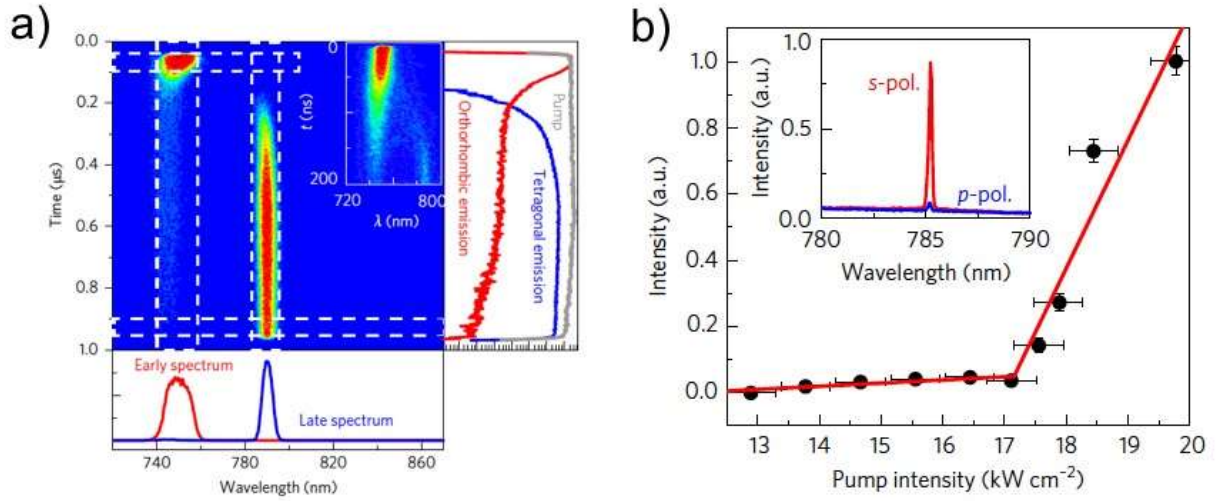


Figure 28. a) Streak camera image of emission from the MAPbI₃ film under the pump intensity 37.5 kWcm⁻² with InGaN diode laser with instantaneous intensity. The substrate temperature is lowered to T = 106 K. In this case, ASE from the orthorhombic phase of MAPbI₃ is observed at early times but evolves within ~200 ns. b) Input–output characteristic of the laser under continuous excitation by a $\lambda = 445$ nm InGaN pump diode at a substrate temperature of 102 K, demonstrating a clear threshold at IP ≈ 17 kW cm⁻² ²⁰². Reprinted with permission from ref 202. Copy right 2017, Nature Publishing Group.

References

- (1) Kojima, A.; Teshima, K.; Shirai, Y.; Miyasaka, T. Organometal halide perovskites as visible-light sensitizers for photovoltaic cells. *J. Am. Chem. Soc.* **2009**, *131*, 6050-6051.
- (2) Kim, H. S.; Lee, C. R.; Im, J. H.; Lee, K. B.; Moehl, T.; Marchioro, A.; Moon, S. J.; Humphry-Baker, R.; Yum, J. H.; Moser, J. E. et al. Lead iodide perovskite sensitized all-solid-state submicron thin film mesoscopic solar cell with efficiency exceeding 9%. *Sci. Rep.* **2012**, *2*, 591.
- (3) Lee, M. M.; Teuscher, J.; Miyasaka, T.; Murakami, T. N.; Snaith, H. J. Efficient hybrid solar cells based on meso-superstructured organometal halide perovskites. *Science* **2012**, *338*, 643.
- (4) Abrusci, A.; Stranks, S. D.; Docampo, P.; Yip, H. L.; Jen, A. K.; Snaith, H. J. High-performance perovskite-polymer hybrid solar cells via electronic coupling with fullerene monolayers. *Nano Lett.* **2013**, *13*, 3124-3128.
- (5) Burschka, J.; Pellet, N.; Moon, S. J.; Humphry-Baker, R.; Gao, P.; Nazeeruddin, M. K.; Gratzel, M. Sequential deposition as a route to high-performance perovskite-sensitized solar cells. *Nature* **2013**, *499*, 316.
- (6) Liu, M.; Johnston, M. B.; Snaith, H. J. Efficient planar heterojunction perovskite solar cells by vapour deposition. *Nature* **2013**, *501*, 395-398.
- (7) <http://www.nrel.gov/ncpv>.
- (8) Stranks, S. D.; Eperon, G. E.; Grancini, G.; Menelaou, C.; Alcocer, M. J. P.; Leijtens, T.; Herz, L. M.; Petrozza, A.; Snaith, H. J. Electron-Hole Diffusion Lengths Exceeding 1 Micrometer in an Organometal Trihalide Perovskite Absorber. *Science* **2013**, *342*, 341-344.
- (9) Sutherland, B. R.; Sargent, E. H. Perovskite photonic sources. *Nat. Photonics* **2016**, *10*, 295.
- (10) Era, M.; Morimoto, S.; Tsutsui, T.; Saito, S. Organic - inorganic heterostructure electroluminescent device using a layered perovskite semiconductor (C₆H₅C₂H₄NH₃)₂PbI₄. *Appl. Phys. Lett.* **1994**, *65*, 676-678.
- (11) Tan, Z. K.; Moghaddam, R. S.; Lai, M. L.; Docampo, P.; Higler, R.; Deschler, F.; Price, M.; Sadhanala, A.; Pazos, L. M.; Credgington, D. et al. Bright light-emitting diodes based on organometal halide perovskite. *Nat. Nanotechnol.* **2014**, *9*, 687.
- (12) Cho, H.; Jeong, S. H.; Park, M. H.; Kim, Y. H.; Wolf, C.; Lee, C. L.; Heo, J. H.; Sadhanala, A.; Myoung, N.; Yoo, S. et al. Overcoming the electroluminescence efficiency limitations of perovskite light-emitting diodes. *Science* **2015**, *350*, 1222.
- (13) Ptak, M.; Mączka, M.; Gaḡor, A.; Sieradzki, A.; Stroppa, A.; Di Sante, D.; Perez-Mato, J. M.; Macalik, L. Experimental and theoretical studies of structural phase transition in a novel polar perovskite-like [C₂H₅NH₃][Na_{0.5}Fe_{0.5}(HCOO)₃] formate. *Dalton transactions* **2016**, *45*, 2574-2583.
- (14) Frost, J. M.; Butler, K. T.; Brivio, F.; Hendon, C. H.; Van Schilfgaarde, M.; Walsh, A. Atomistic origins of high-performance in hybrid halide perovskite solar cells. *Nano Lett.* **2014**, *14*, 2584-2590.
- (15) Anusca, I.; Balčiūnas, S.; Gemeiner, P.; Svirskas, Š.; Sanlialp, M.; Lackner, G.; Fettkenhauer, C.; Belovickis, J.; Samulionis, V.; Ivanov, M. Dielectric response: Answer to many questions in the methylammonium lead halide solar cell absorbers. *Adv. Energy Mater.* **2017**, *7*, 1700600.

- (16) Tan, H.; Che, F.; Wei, M.; Zhao, Y.; Saidaminov, M. I.; Todorović, P.; Broberg, D.; Walters, G.; Tan, F.; Zhuang, T. Dipolar cations confer defect tolerance in wide-bandgap metal halide perovskites. *Nat. commun.* **2018**, *9*, 3100.
- (17) Druzbicki, K.; Pinna, R. S.; Rudić, S.; Jura, M.; Gorini, G.; Fernandez-Alonso, F. Unexpected cation dynamics in the low-temperature phase of methylammonium lead iodide: the need for improved models. *J. Phys. Chem. Lett.* **2016**, *7*, 4701-4709.
- (18) Brivio, F.; Frost, J. M.; Skelton, J. M.; Jackson, A. J.; Weber, O. J.; Weller, M. T.; Goni, A. R.; Leguy, A. M.; Barnes, P. R.; Walsh, A. Lattice dynamics and vibrational spectra of the orthorhombic, tetragonal, and cubic phases of methylammonium lead iodide. *Phys. Rev. B* **2015**, *92*, 144308.
- (19) Pérez-Osorio, M. A.; Milot, R. L.; Filip, M. R.; Patel, J. B.; Herz, L. M.; Johnston, M. B.; Giustino, F. Vibrational properties of the organic-inorganic halide perovskite CH₃NH₃PbI₃ from theory and experiment: factor group analysis, first-principles calculations, and low-temperature infrared spectra. *J. Phys. Chem. C* **2015**, *119*, 25703-25718.
- (20) Mattoni, A.; Filippetti, A.; Saba, M.; Caddeo, C.; Delugas, P. Temperature evolution of methylammonium trihalide vibrations at the atomic scale. *J. Phys. Chem. Lett.* **2016**, *7*, 529-535.
- (21) Leguy, A. M.; Goñi, A. R.; Frost, J. M.; Skelton, J.; Brivio, F.; Rodríguez-Martínez, X.; Weber, O. J.; Pallipurath, A.; Alonso, M. I.; Campoy-Quiles, M. Dynamic disorder, phonon lifetimes, and the assignment of modes to the vibrational spectra of methylammonium lead halide perovskites. *Phys. Chem. Chem. Phys.* **2016**, *18*, 27051-27066.
- (22) Lotsch, B. V. New light on an old story: perovskites go solar. *Angew. Chem. Int. Ed.* **2014**, *53*, 635-637.
- (23) Quan, L. N.; Yuan, M.; Comin, R.; Voznyy, O.; Beauregard, E. M.; Hoogland, S.; Buin, A.; Kirmani, A. R.; Zhao, K.; Amassian, A. et al. Ligand-Stabilized Reduced-Dimensionality Perovskites. *J. Am. Chem. Soc.* **2016**, *138*, 2649-2655.
- (24) De Wolf, S.; Holovsky, J.; Moon, S.-J.; Löper, P.; Niesen, B.; Ledinsky, M.; Haug, F.-J.; Yum, J.-H.; Ballif, C. Organometallic halide perovskites: sharp optical absorption edge and its relation to photovoltaic performance. *J. Phys. Chem. Lett.* **2014**, *5*, 1035-1039.
- (25) Shi, D.; Adinolfi, V.; Comin, R.; Yuan, M.; Alarousu, E.; Buin, A.; Chen, Y.; Hoogland, S.; Rothenberger, A.; Katsiev, K. et al. Low trap-state density and long carrier diffusion in organolead trihalide perovskite single crystals. *Science* **2015**, *347*, 519-522.
- (26) Senanayak, S. P.; Yang, B.; Thomas, T. H.; Giesbrecht, N.; Huang, W.; Gann, E.; Nair, B.; Goedel, K.; Guha, S.; Moya, X. Understanding charge transport in lead iodide perovskite thin-film field-effect transistors. *Science Advances* **2017**, *3*, e1601935.
- (27) Philippe, B.; Jacobsson, T. J.; Correa-Baena, J.-P.; Jena, N. K.; Banerjee, A.; Chakraborty, S.; Cappel, U. B.; Ahuja, R.; Hagfeldt, A.; Odelius, M. Valence Level Character in a Mixed Perovskite Material and Determination of the Valence Band Maximum from Photoelectron Spectroscopy: Variation with Photon Energy. *J. Phys. Chem. C* **2017**, *121*, 26655-26666.
- (28) Saliba, M.; Matsui, T.; Seo, J. Y.; Domanski, K.; Correa-Baena, J. P.; Nazeeruddin, M. K.; Zakeeruddin, S. M.; Tress, W.; Abate, A.; Hagfeldt, A. et al. Cesium-containing triple cation perovskite solar cells: improved stability, reproducibility and high efficiency. *Energy Environ. Sci.* **2016**, *9*, 1989-1997.

- (29) Abdi-Jalebi, M.; Andaji-Garmaroudi, Z.; Cacovich, S.; Stavrakas, C.; Philippe, B.; Richter, J. M.; Alsari, M.; Booker, E. P.; Hutter, E. M.; Pearson, A. J. Maximizing and stabilizing luminescence from halide perovskites with potassium passivation. *Nature* **2018**, *555*, 497.
- (30) Xiao, Z.; Zhao, L.; Tran, N. L.; Lin, Y. L.; Silver, S. H.; Kerner, R. A.; Yao, N.; Kahn, A.; Scholes, G. D.; Rand, B. P. Mixed-halide perovskites with stabilized bandgaps. *Nano Lett.* **2017**, *17*, 6863-6869.
- (31) Li, N.; Zhu, Z.; Li, J.; Jen, A. K. Y.; Wang, L. Inorganic CsPb1- xSnxIBr2 for Efficient Wide - Bandgap Perovskite Solar Cells. *Adv. Energy Mater.* **2018**, 1800525.
- (32) Vorpahl, S. M.; Stranks, S. D.; Nagaoka, H.; Eperon, G. E.; Ziffer, M. E.; Snaith, H. J.; Ginger, D. S. Impact of microstructure on local carrier lifetime in perovskite solar cells. *Science* **2015**, aaa5333.
- (33) Mitzi, D. B. Synthesis, structure, and properties of organic - inorganic perovskites and related materials. *Prog. Inorg. Chem.* **1999**, 1-121.
- (34) Mitzi, D. B.; Feild, C.; Harrison, W.; Guloy, A. Conducting tin halides with a layered organic-based perovskite structure. *Nature* **1994**, *369*, 467.
- (35) Hong, X.; Ishihara, T.; Nurmikko, A. Photoconductivity and electroluminescence in lead iodide based natural quantum well structures. *Solid State Commun.* **1992**, *84*, 657-661.
- (36) Chondroudis, K.; Mitzi, D. B. Electroluminescence from an organic- inorganic perovskite incorporating a quaterthiophene dye within lead halide perovskite layers. *Chem. Mater.* **1999**, *11*, 3028.
- (37) Yuan, M.; Quan, L. N.; Comin, R.; Walters, G.; Sabatini, R.; Voznyy, O.; Hoogland, S.; Zhao, Y.; Beauregard, E. M.; Kanjanaboos, P. et al. Perovskite energy funnels for efficient light-emitting diodes. *Nat. Nanotechnol.* **2016**, *11*, 872.
- (38) Xiao, Z.; Kerner, R. A.; Zhao, L.; Tran, N. L.; Lee, K. M.; Koh, T.-W.; Scholes, G. D.; Rand, B. P. Efficient perovskite light-emitting diodes featuring nanometre-sized crystallites. *Nat. Photonics* **2017**, *11*, 108.
- (39) Wang, N.; Cheng, L.; Ge, R.; Zhang, S.; Miao, Y.; Zou, W.; Yi, C.; Sun, Y.; Cao, Y.; Yang, R. et al. Perovskite light-emitting diodes based on solution-processed self-organized multiple quantum wells. *Nat. Photonics* **2016**, *10*, 699-704.
- (40) Quan, L. N.; Zhao, Y.; Garcia de Arquer, F. P.; Sabatini, R.; Walters, G.; Voznyy, O.; Comin, R.; Li, Y.; Fan, J. Z.; Tan, H. et al. Tailoring the Energy Landscape in Quasi-2D Halide Perovskites Enables Efficient Green-Light Emission. *Nano Lett.* **2017**, *17*, 3701.
- (41) Byun, J.; Cho, H.; Wolf, C.; Jang, M.; Sadhanala, A.; Friend, R. H.; Yang, H.; Lee, T. W. Efficient Visible Quasi - 2D Perovskite Light - Emitting Diodes. *Adv. Mater.* **2016**, *28*, 7515-7520.
- (42) Tsai, H.; Nie, W.; Blancon, J. C.; Stoumpos, C. C.; Asadpour, R.; Harutyunyan, B.; Neukirch, A. J.; Verduzco, R.; Crochet, J. J.; Tretiak, S. et al. High-efficiency two-dimensional Ruddlesden-Popper perovskite solar cells. *Nature* **2016**, *536*, 312-316.
- (43) Cao, D. H.; Stoumpos, C. C.; Farha, O. K.; Hupp, J. T.; Kanatzidis, M. G. 2D homologous perovskites as light-absorbing materials for solar cell applications. *J. Am. Chem. Soc.* **2015**, *137*, 7843.
- (44) Mitzi, D.; Wang, S.; Feild, C.; Chess, C.; Guloy, A. Conducting layered organic-inorganic halides containing < 110 >-oriented perovskite sheets. *Science* **1995**, *267*, 1473-1476.

- (45) Li, Y.; Zheng, G.; Lin, C.; Lin, J. Synthesis, structure and optical properties of different dimensional organic-inorganic perovskites. *Solid State Sciences* **2007**, *9*, 855-861.
- (46) Sun, S.; Tominaka, S.; Lee, J.-H.; Xie, F.; Bristowe, P. D.; Cheetham, A. K. Synthesis, crystal structure, and properties of a perovskite-related bismuth phase, $(\text{NH}_4)_3\text{Bi}_2\text{I}_9$. *Applied Physics Letter Materials* **2016**, *4*, 031101.
- (47) Zaleski, J.; Pietraszko, A. Structure at 200 and 298 K and X - ray investigations of the phase transition at 242 K of $[\text{NH}_2(\text{CH}_3)_2]_3\text{Sb}_2\text{Cl}_9$ (DMACA). *Acta Crystallographica Section B* **1996**, *52*, 287-295.
- (48) Kallel, A.; Bats, J. Tris (trimethylammonium) nonachlorodiantimonate (III), $[\text{NH}(\text{CH}_3)_3]_3[\text{Sb}_2\text{Cl}_9]$. *Acta Crystallographica Section C* **1985**, *41*, 1022-1024.
- (49) Dohner, E. R.; Hoke, E. T.; Karunadasa, H. I. Self-assembly of broadband white-light emitters. *J. Am. Chem. Soc.* **2014**, *136*, 1718-1721.
- (50) Dohner, E. R.; Jaffe, A.; Bradshaw, L. R.; Karunadasa, H. I. Intrinsic white-light emission from layered hybrid perovskites. *J. Am. Chem. Soc.* **2014**, *136*, 13154-13157.
- (51) Hu, T.; Smith, M. D.; Dohner, E. R.; Sher, M.-J.; Wu, X.; Trinh, M. T.; Fisher, A.; Corbett, J.; Zhu, X.-Y.; Karunadasa, H. I. Mechanism for broadband white-light emission from two-dimensional (110) hybrid perovskites. *J. Phys. Chem. Lett.* **2016**, *7*, 2258-2263.
- (52) Mao, L.; Wu, Y.; Stoumpos, C. C.; Wasielewski, M. R.; Kanatzidis, M. G. White-Light Emission and Structural Distortion in New Corrugated Two-Dimensional Lead Bromide Perovskites. *Journal of American Chemical Society* **2017**, *139*, 5210-5215.
- (53) Nikl, M.; Mihokova, E.; Nitsch, K.; Somma, F.; Giampaolo, C.; Pazzi, G.; Fabeni, P.; Zazubovich, S. Photoluminescence of Cs_4PbBr_6 crystals and thin films. *Chem. Phys. Lett.* **1999**, *306*, 280-284.
- (54) Palazon, F.; Almeida, G.; Akkerman, Q. A.; De Trizio, L.; Dang, Z.; Prato, M.; Manna, L. Changing the dimensionality of cesium lead bromide nanocrystals by reversible postsynthesis transformations with Amines. *Chem. Mater.* **2017**, *29*, 4167-4171.
- (55) Wu, L.; Hu, H.; Xu, Y.; Jiang, S.; Chen, M.; Zhong, Q.; Yang, D.; Liu, Q.; Zhao, Y.; Sun, B. From nonluminescent Cs_4PbX_6 ($\text{X} = \text{Cl}, \text{Br}, \text{I}$) nanocrystals to highly luminescent CsPbX_3 nanocrystals: water-triggered transformation through a CsX -stripping mechanism. *Nano Lett.* **2017**, *17*, 5799-5804.
- (56) Palazon, F.; Urso, C.; De Trizio, L.; Akkerman, Q.; Marras, S.; Locardi, F.; Nelli, I.; Ferretti, M.; Prato, M.; Manna, L. Postsynthesis Transformation of insulating Cs_4PbBr_6 nanocrystals into bright perovskite CsPbBr_3 through physical and chemical extraction of CsBr . *ACS Energy Lett.* **2017**, *2*, 2445-2448.
- (57) Liu, Z.; Bekenstein, Y.; Ye, X.; Nguyen, S. C.; Swabeck, J.; Zhang, D.; Lee, S.-T.; Yang, P.; Ma, W.; Alivisatos, A. P. Ligand mediated transformation of cesium lead bromide perovskite nanocrystals to lead depleted Cs_4PbBr_6 nanocrystals. *J. Am. Chem. Soc.* **2017**, *139*, 5309-5312.
- (58) Quan, L. N.; Quintero - Bermudez, R.; Voznyy, O.; Walters, G.; Jain, A.; Fan, J. Z.; Zheng, X.; Yang, Z.; Sargent, E. H. Highly emissive green perovskite nanocrystals in a solid state crystalline matrix. *Adv. Mater.* **2017**, *29*, 1605945.
- (59) Chen, X.; Zhang, F.; Ge, Y.; Shi, L.; Huang, S.; Tang, J.; Lv, Z.; Zhang, L.; Zou, B.; Zhong, H. Centimeter - Sized Cs_4PbBr_6 Crystals with Embedded CsPbBr_3 Nanocrystals Showing Superior Photoluminescence: Nonstoichiometry Induced Transformation and Light - Emitting Applications. *Adv. Funct. Mater.* **2018**, *28*, 1706567.

- (60) Savory, C. N.; Walsh, A.; Scanlon, D. O. Can Pb-free halide double perovskites support high-efficiency solar cells? *ACS Energy Lett.* **2016**, *1*, 949-955.
- (61) Xiao, Z.; Zhou, Y.; Hosono, H.; Kamiya, T. Intrinsic defects in a photovoltaic perovskite variant Cs₂SnI₆. *Phys. Chem. Chem. Phys.* **2015**, *17*, 18900-18903.
- (62) Jain, A.; Voznyy, O.; Sargent, E. H. High-throughput screening of lead-free perovskite-like materials for optoelectronic applications. *J. Phys. Chem. C* **2017**, *121*, 7183-7187.
- (63) Slavney, A. H.; Hu, T.; Lindenberg, A. M.; Karunadasa, H. I. A bismuth-halide double perovskite with long carrier recombination lifetime for photovoltaic applications. *J. Am. Chem. Soc.* **2016**, *138*, 2138-2141.
- (64) Shi, Z.; Guo, J.; Chen, Y.; Li, Q.; Pan, Y.; Zhang, H.; Xia, Y.; Huang, W. Lead - Free Organic-Inorganic Hybrid Perovskites for Photovoltaic Applications: Recent Advances and Perspectives. *Adv. Mater.* **2017**, *29*, 1605005.
- (65) Lee, S. J.; Shin, S. S.; Kim, Y. C.; Kim, D.; Ahn, T. K.; Noh, J. H.; Seo, J.; Seok, S. I. Fabrication of efficient formamidinium tin iodide perovskite solar cells through SnF₂-pyrazine complex. *J. Am. Chem. Soc.* **2016**, *138*, 3974-3977.
- (66) Gupta, S.; Cahen, D.; Hodes, G. How SnF₂ Impacts the Material Properties of Lead-Free Tin Perovskites. *J. Phys. Chem. C* **2018**, *122*, 13926-13936.
- (67) Yuan, F.; Xi, J.; Dong, H.; Xi, K.; Zhang, W.; Ran, C.; Jiao, B.; Hou, X.; Jen, A. K. Y.; Wu, Z. All - Inorganic Hetero - Structured Cesium Tin Halide Perovskite Light - Emitting Diodes With Current Density Over 900 A cm⁻² and Its Amplified Spontaneous Emission Behaviors. *physica status solidi (RRL)*-*Rapid Research Letters* **2018**, *12*, 1800090.
- (68) Lanzetta, L.; Marin-Beloqui, J. M.; Sanchez-Molina, I.; Ding, D.; Haque, S. A. Two-dimensional organic tin halide perovskites with tunable visible emission and their use in light-emitting devices. *ACS Energy Lett.* **2017**, *2*, 1662-1668.
- (69) Stoumpos, C. C.; Frazer, L.; Clark, D. J.; Kim, Y. S.; Rhim, S. H.; Freeman, A. J.; Ketterson, J. B.; Jang, J. I.; Kanatzidis, M. G. Hybrid germanium iodide perovskite semiconductors: active lone pairs, structural distortions, direct and indirect energy gaps, and strong nonlinear optical properties. *J. Am. Chem. Soc.* **2015**, *137*, 6804-6819.
- (70) Filip, M. R.; Hillman, S.; Haghighirad, A. A.; Snaith, H. J.; Giustino, F. Band gaps of the lead-free halide double perovskites Cs₂BiAgCl₆ and Cs₂BiAgBr₆ from theory and experiment. *J. Phys. Chem. Lett.* **2016**, *7*, 2579-2585.
- (71) Vargas, B.; Ramos, E.; Pérez-Gutiérrez, E.; Alonso, J. C.; Solis-Ibarra, D. A Direct Bandgap Copper-Antimony Halide Perovskite. *J. Am. Chem. Soc.* **2017**, *139*, 9116-9119.
- (72) Leng, M.; Chen, Z.; Yang, Y.; Li, Z.; Zeng, K.; Li, K.; Niu, G.; He, Y.; Zhou, Q.; Tang, J. Lead - Free, Blue Emitting Bismuth Halide Perovskite Quantum Dots. *Angew. Chem. Int. Ed.* **2016**, *55*, 15012-15016.
- (73) Wehrenfennig, C.; Liu, M.; Snaith, H. J.; Johnston, M. B.; Herz, L. M. Charge-carrier dynamics in vapour-deposited films of the organolead halide perovskite CH₃NH₃PbI_{3-x}Cl_x. *Energy Environ. Sci.* **2014**, *7*, 2269-2275.
- (74) Stranks, S. D.; Eperon, G. E.; Grancini, G.; Menelaou, C.; Alcocer, M. J.; Leijtens, T.; Herz, L. M.; Petrozza, A.; Snaith, H. J. Electron-hole diffusion lengths exceeding 1 micrometer in an organometal trihalide perovskite absorber. *Science* **2013**, *342*, 341-344.

- (75) Brenner, T. M.; Egger, D. A.; Rappe, A. M.; Kronik, L.; Hodes, G.; Cahen, D. Are Mobilities in Hybrid Organic-Inorganic Halide Perovskites Actually "High"? *J. Phys. Chem. Lett.* **2015**, *6*, 4754-4757.
- (76) Oga, H.; Saeki, A.; Ogomi, Y.; Hayase, S.; Seki, S. Improved understanding of the electronic and energetic landscapes of perovskite solar cells: high local charge carrier mobility, reduced recombination, and extremely shallow traps. *J. Am. Chem. Soc.* **2014**, *136*, 13818-13825.
- (77) Manser, J. S.; Kamat, P. V. Band filling with free charge carriers in organometal halide perovskites. *Nat. Photonics* **2014**, *8*, 737-743.
- (78) Saba, M.; Cadelano, M.; Marongiu, D.; Chen, F.; Sarritzu, V.; Sestu, N.; Figus, C.; Aresti, M.; Piras, R.; Lehmann, A. G. Correlated electron-hole plasma in organometal perovskites. *Nat. commun.* **2014**, *5*, 5049.
- (79) Yamada, Y.; Nakamura, T.; Endo, M.; Wakamiya, A.; Kanemitsu, Y. Photocarrier recombination dynamics in perovskite CH₃NH₃PbI₃ for solar cell applications. *J. Am. Chem. Soc.* **2014**, *136*, 11610-11613.
- (80) Manger, L. H.; Rowley, M. B.; Fu, Y.; Foote, A. K.; Rea, M. T.; Wood, S. L.; Jin, S.; Wright, J. C.; Goldsmith, R. H. Global Analysis of Perovskite Photophysics Reveals Importance of Geminate Pathways. *J. Phys. Chem. C* **2017**, *121*, 1062-1071.
- (81) Stampelcoskie, K. G.; Manser, J. S.; Kamat, P. V. Dual nature of the excited state in organic-inorganic lead halide perovskites. *Energy Environ. Sci.* **2015**, *8*, 208-215.
- (82) Wehrenfennig, C.; Eperon, G. E.; Johnston, M. B.; Snaith, H. J.; Herz, L. M. High charge carrier mobilities and lifetimes in organolead trihalide perovskites. *Adv. Mater.* **2014**, *26*, 1584-1589.
- (83) Johnston, M. B.; Herz, L. M. Hybrid perovskites for photovoltaics: charge-carrier recombination, diffusion, and radiative efficiencies. *Acc. Chem. Res.* **2015**, *49*, 146-154.
- (84) Richter, J. M.; Abdi-Jalebi, M.; Sadhanala, A.; Tabachnyk, M.; Rivett, J. P.; Pazos-Outón, L. M.; Gödel, K. C.; Price, M.; Deschler, F.; Friend, R. H. Enhancing photoluminescence yields in lead halide perovskites by photon recycling and light out-coupling. *Nat. commun.* **2016**, *7*, 13941.
- (85) Yang, Y.; Ostrowski, D. P.; France, R. M.; Zhu, K.; van de Lagemaat, J.; Luther, J. M.; Beard, M. C. Observation of a hot-phonon bottleneck in lead-iodide perovskites. *Nat. Photonics* **2015**, *10*, 53-59.
- (86) Rehman, W.; Milot, R. L.; Eperon, G. E.; Wehrenfennig, C.; Boland, J. L.; Snaith, H. J.; Johnston, M. B.; Herz, L. M. Charge - carrier dynamics and mobilities in formamidinium lead mixed - halide perovskites. *Adv. Mater.* **2015**, *27*, 7938-7944.
- (87) Ponseca Jr, C. S.; Savenije, T. J.; Abdellah, M.; Zheng, K.; Yartsev, A.; Pascher, T. r.; Harlang, T.; Chabera, P.; Pullerits, T.; Stepanov, A. Organometal halide perovskite solar cell materials rationalized: ultrafast charge generation, high and microsecond-long balanced mobilities, and slow recombination. *J. Am. Chem. Soc.* **2014**, *136*, 5189-5192.
- (88) Beattie, A.; Landsberg, P. Auger effect in semiconductors. *Proc. R. Soc. London, Ser. A* **1959**, *249*, 16-29.
- (89) Sheik-Bahae, M.; Epstein, R. I. Can laser light cool semiconductors? *Phys. Rev. Lett.* **2004**, *92*, 247403.

- (90) Even, J.; Pedesseau, L.; Katan, C. Analysis of multivalley and multibandgap absorption and enhancement of free carriers related to exciton screening in hybrid perovskites. *J. Phys. Chem. C* **2014**, *118*, 11566-11572.
- (91) Tanaka, K.; Takahashi, T.; Ban, T.; Kondo, T.; Uchida, K.; Miura, N. Comparative study on the excitons in lead-halide-based perovskite-type crystals CH₃NH₃PbBr₃ CH₃NH₃PbI₃. *Solid State Commun.* **2003**, *127*, 619-623.
- (92) Hirasawa, M.; Ishihara, T.; Goto, T.; Uchida, K.; Miura, N. Magnetoabsorption of the lowest exciton in perovskite-type compound (CH₃NH₃) PbI₃. *Physica B: Condensed Matter* **1994**, *201*, 427-430.
- (93) Lin, Q.; Armin, A.; Nagiri, R. C. R.; Burn, P. L.; Meredith, P. Electro-optics of perovskite solar cells. *Nat. Photonics* **2015**, *9*, 106.
- (94) Miyata, A.; Mitiglu, A.; Plochocka, P.; Portugall, O.; Wang, J. T.-W.; Stranks, S. D.; Snaith, H. J.; Nicholas, R. J. Direct measurement of the exciton binding energy and effective masses for charge carriers in organic-inorganic tri-halide perovskites. *Nat. Phys.* **2015**, *11*, 582-587.
- (95) D'Innocenzo, V.; Grancini, G.; Alcocer, M. J.; Kandada, A. R.; Stranks, S. D.; Lee, M. M.; Lanzani, G.; Snaith, H. J.; Petrozza, A. Excitons versus free charges in organo-lead tri-halide perovskites. *Nat. commun.* **2014**, *5*, 3586.
- (96) Savenije, T. J.; Ponseca Jr, C. S.; Kunneman, L.; Abdellah, M.; Zheng, K.; Tian, Y.; Zhu, Q.; Canton, S. E.; Scheblykin, I. G.; Pullerits, T. Thermally activated exciton dissociation and recombination control the carrier dynamics in organometal halide perovskite. *J. Phys. Chem. Lett.* **2014**, *5*, 2189-2194.
- (97) Wu, K.; Bera, A.; Ma, C.; Du, Y.; Yang, Y.; Li, L.; Wu, T. Temperature-dependent excitonic photoluminescence of hybrid organometal halide perovskite films. *Phys. Chem. Chem. Phys.* **2014**, *16*, 22476-22481.
- (98) Sestu, N.; Cadelano, M.; Sarritzu, V.; Chen, F.; Marongiu, D.; Piras, R.; Mainas, M.; Quochi, F.; Saba, M.; Mura, A. Absorption F-sum rule for the exciton binding energy in methylammonium lead halide perovskites. *J. Phys. Chem. Lett.* **2015**, *6*, 4566-4572.
- (99) Kersting, R.; Lemmer, U.; Deussen, M.; Bakker, H.; Mahrt, R.; Kurz, H.; Arkhipov, V. I.; Bäessler, H.; Göbel, E. Ultrafast field-induced dissociation of excitons in conjugated polymers. *Phys. Rev. Lett.* **1994**, *73*, 1440.
- (100) Knupfer, M. Exciton binding energies in organic semiconductors. *Appl. Phys. A* **2003**, *77*, 623-626.
- (101) Sun, S.; Salim, T.; Mathews, N.; Duchamp, M.; Boothroyd, C.; Xing, G.; Sum, T. C.; Lam, Y. M. The origin of high efficiency in low-temperature solution-processable bilayer organometal halide hybrid solar cells. *Energy Environ. Sci.* **2014**, *7*, 399-407.
- (102) Nah, S.; Spokoyny, B.; Stoumpos, C.; Soe, C. M. M.; Kanatzidis, M.; Harel, E. Spatially segregated free-carrier and exciton populations in individual lead halide perovskite grains. *Nat. Photonics* **2017**, *11*, 285-288.
- (103) Gélvez-Rueda, M. C.; Hutter, E. M.; Cao, D. H.; Renaud, N.; Stoumpos, C. C.; Hupp, J. T.; Savenije, T. J.; Kanatzidis, M. G.; Grozema, F. C. Interconversion between free charges and bound excitons in 2D hybrid lead halide perovskites. *J. Phys. Chem. C* **2017**, *121*, 26566-26574.
- (104) de Mello, J. C.; Wittmann, H. F.; Friend, R. H. An improved experimental determination of external photoluminescence quantum efficiency. *Adv. Mater.* **1997**, *9*, 230-232.

- (105) Deschler, F.; Price, M.; Pathak, S.; Klintberg, L. E.; Jarausch, D.-D.; Higler, R.; Hüttner, S.; Leijtens, T.; Stranks, S. D.; Snaith, H. J. et al. High photoluminescence efficiency and optically pumped lasing in solution-processed mixed halide perovskite semiconductors. *J. Phys. Chem. Lett.* **2014**, *5*, 1421-1426.
- (106) Pan, J.; Quan, L. N.; Zhao, Y.; Peng, W.; Murali, B.; Sarmah, S. P.; Yuan, M.; Sinatra, L.; Alyami, N. M.; Liu, J. et al. Highly Efficient Perovskite-Quantum-Dot Light-Emitting Diodes by Surface Engineering. *Adv. Mater.* **2016**, *28*, 8718-8725.
- (107) Liu, F.; Zhang, Y.; Ding, C.; Kobayashi, S.; Izuishi, T.; Nakazawa, N.; Toyoda, T.; Ohta, T.; Hayase, S.; Minemoto, T. Highly luminescent phase-stable CsPbI₃ perovskite quantum dots achieving near 100% absolute photoluminescence quantum yield. *ACS nano* **2017**, *11*, 10373-10383.
- (108) Hattori, T.; Taira, T.; Era, M.; Tsutsui, T.; Saito, S. Highly efficient electroluminescence from a heterostructure device combined with emissive layered-perovskite and an electron-transporting organic compound. *Chem. Phys. Lett.* **1996**, *254*, 103-108.
- (109) Kim, Y. H.; Cho, H.; Heo, J. H.; Kim, T. S.; Myoung, N.; Lee, C. L.; Im, S. H.; Lee, T. W. Multicolored organic/inorganic hybrid perovskite light-emitting diodes. *Adv. Mater.* **2015**, *27*, 1248.
- (110) Li, G.; Tan, Z. K.; Di, D.; Lai, M. L.; Jiang, L.; Lim, J. H.; Friend, R. H.; Greenham, N. C. Efficient light-emitting diodes based on nanocrystalline perovskite in a dielectric polymer matrix. *Nano Lett.* **2015**, *15*, 2640.
- (111) Li, J.; Bade, S. G.; Shan, X.; Yu, Z. Single-Layer Light-Emitting Diodes Using Organometal Halide Perovskite/Poly(ethylene oxide) Composite Thin Films. *Adv. Mater.* **2015**, *27*, 5196.
- (112) Park, M.-H.; Jeong, S.-H.; Seo, H.-K.; Wolf, C.; Kim, Y.-H.; Kim, H.; Byun, J.; Kim, J. S.; Cho, H.; Lee, T.-W. Unravelling additive-based nanocrystal pinning for high efficiency organic-inorganic halide perovskite light-emitting diodes. *Nano Energy* **2017**, *42*, 157-165.
- (113) Cho, H.; Kim, J. S.; Wolf, C.; Kim, Y.-H.; Yun, H. J.; Jeong, S.-H.; Sadhanala, A.; Venugopalan, V.; Choi, J. W.; Lee, C.-L. et al. High-Efficiency Polycrystalline Perovskite Light-Emitting Diodes Based on Mixed Cations. *ACS nano* **2018**, *12*, 2883-2892.
- (114) Zhang, S.; Yi, C.; Wang, N.; Sun, Y.; Zou, W.; Wei, Y.; Cao, Y.; Miao, Y.; Li, R.; Yin, Y. et al. Efficient Red Perovskite Light-Emitting Diodes Based on Solution-Processed Multiple Quantum Wells. *Adv. Mater.* **2017**, *29*.
- (115) Rehman, W.; McMeekin, D. P.; Patel, J. B.; Milot, R. L.; Johnston, M. B.; Snaith, H. J.; Herz, L. M. Photovoltaic mixed-cation lead mixed-halide perovskites: links between crystallinity, photo-stability and electronic properties. *Energy Environ. Sci.* **2017**, *10*, 361-369.
- (116) Kulkarni, S. A.; Muduli, S.; Xing, G.; Yantara, N.; Li, M.; Chen, S.; Sum, T. C.; Mathews, N.; White, T. J.; Mhaisalkar, S. G. Modulating Excitonic Recombination Effects through One - Step Synthesis of Perovskite Nanoparticles for Light - Emitting Diodes. *ChemSusChem* **2017**, *10*, 3818-3824.
- (117) Protesescu, L.; Yakunin, S.; Bodnarchuk, M. I.; Krieg, F.; Caputo, R.; Hendon, C. H.; Yang, R. X.; Walsh, A.; Kovalenko, M. V. Nanocrystals of Cesium Lead Halide Perovskites (CsPbX₃, X = Cl, Br, and I): Novel Optoelectronic Materials Showing Bright Emission with Wide Color Gamut. *Nano Lett.* **2015**, *15*, 3692-3696.

- (118) Li, G.; Rivarola, F. W.; Davis, N. J.; Bai, S.; Jellicoe, T. C.; de la Pena, F.; Hou, S.; Ducati, C.; Gao, F.; Friend, R. H. et al. Highly Efficient Perovskite Nanocrystal Light-Emitting Diodes Enabled by a Universal Crosslinking Method. *Adv. Mater.* **2016**, *28*, 3528-3534.
- (119) Song, J.; Li, J.; Li, X.; Xu, L.; Dong, Y.; Zeng, H. Quantum Dot Light-Emitting Diodes Based on Inorganic Perovskite Cesium Lead Halides (CsPbX₃). *Adv. Mater.* **2015**, *27*, 7162-7167.
- (120) Li, J.; Xu, L.; Wang, T.; Song, J.; Chen, J.; Xue, J.; Dong, Y.; Cai, B.; Shan, Q.; Han, B. et al. 50-Fold EQE Improvement up to 6.27% of Solution Processed All-Inorganic Perovskite CsPbBr₃ QLEDs via Surface Ligand Density Control. *Adv. Mater.* **2017**, *29*, 1603885.
- (121) Zhang, X.; Liu, H.; Wang, W.; Zhang, J.; Xu, B.; Karen, K. L.; Zheng, Y.; Liu, S.; Chen, S.; Wang, K. et al. Hybrid Perovskite Light-Emitting Diodes Based on Perovskite Nanocrystals with Organic-Inorganic Mixed Cations. *Adv. Mater.* **2017**, *29*.
- (122) Yuan, S.; Wang, Z.-K.; Zhuo, M.-P.; Tian, Q.; Jin, Y.; Liao, L.-S. Self-Assembled High Quality CsPbBr₃ Quantum Dot Films Toward Highly Efficient Light-Emitting Diodes. *ACS nano* **2018**.
- (123) Protesescu, L.; Yakunin, S.; Kumar, S.; Bär, J.; Bertolotti, F.; Masciocchi, N.; Guagliardi, A.; Grotevent, M.; Shorubalko, I.; Bodnarchuk, M. I. Dismantling the “red wall” of colloidal perovskites: highly luminescent formamidinium and formamidinium–cesium lead iodide nanocrystals. *ACS nano* **2017**, *11*, 3119-3134.
- (124) Kim, Y.-H.; Lee, G.-H.; Kim, Y.-T.; Wolf, C.; Yun, H. J.; Kwon, W.; Park, C. G.; Lee, T.-W. High efficiency perovskite light-emitting diodes of ligand-engineered colloidal formamidinium lead bromide nanoparticles. *Nano Energy* **2017**, *38*, 51-58.
- (125) Kim, Y.-H.; Wolf, C.; Kim, Y.-T.; Cho, H.; Kwon, W.; Do, S.; Sadhanala, A.; Park, C. G.; Rhee, S.-W.; Im, S. H. Highly efficient light-emitting diodes of colloidal metal–halide perovskite nanocrystals beyond quantum size. *ACS nano* **2017**, *11*, 6586-6593.
- (126) Chin, X. Y.; Perumal, A.; Bruno, A.; Yantara, N.; Veldhuis, S. A.; Martínez-Sarti, L.; Chandran, B.; Chirvony, V.; Lo, A. S.-Z.; So, J. Self-assembled hierarchical nanostructured perovskites enable highly efficient LEDs via an energy cascade. *Energy Environ. Sci.* **2018**, DOI:10.1039/C7EE03543H 10.1039/C7EE03543H.
- (127) Yang, J.; Siempelkamp, B. D.; Mosconi, E.; De Angelis, F.; Kelly, T. L. Origin of the thermal instability in CH₃NH₃PbI₃ thin films deposited on ZnO. *Chem. Mater.* **2015**, *27*, 4229-4236.
- (128) Wang, J.; Wang, N.; Jin, Y.; Si, J.; Tan, Z. K.; Du, H.; Cheng, L.; Dai, X.; Bai, S.; He, H. et al. Interfacial control toward efficient and low-voltage perovskite light-emitting diodes. *Adv. Mater.* **2015**, *27*, 2311.
- (129) Zhang, L.; Yang, X.; Jiang, Q.; Wang, P.; Yin, Z.; Zhang, X.; Tan, H.; Yang, Y. M.; Wei, M.; Sutherland, B. R. et al. Ultra-bright and highly efficient inorganic based perovskite light-emitting diodes. *Nat. commun.* **2017**, *8*, 15640.
- (130) Yan, F.; Xing, J.; Xing, G.; Quan, L.; Tan, S. T.; Zhao, J.; Su, R.; Zhang, L.; Chen, S.; Zhao, Y. Highly efficient visible colloidal lead-halide perovskite nanocrystal light-emitting diodes. *Nano Lett.* **2018**, *18*, 3157-3164.
- (131) Lu, L. P.; Kabra, D.; Johnson, K.; Friend, R. H. Charge - Carrier Balance and Color Purity in Polyfluorene Polymer Blends for Blue Light - Emitting Diodes. *Adv. Funct. Mater.* **2012**, *22*, 144-150.

- (132) Nguyen, W. H.; Bailie, C. D.; Unger, E. L.; McGehee, M. D. Enhancing the hole-conductivity of spiro-OMeTAD without oxygen or lithium salts by using spiro (TFSI) 2 in perovskite and dye-sensitized solar cells. *J. Am. Chem. Soc.* **2014**, *136*, 10996-11001.
- (133) Hoyer, R. L.; Chua, M. R.; Musselman, K. P.; Li, G.; Lai, M. L.; Tan, Z. K.; Greenham, N. C.; MacManus-Driscoll, J. L.; Friend, R. H.; Credgington, D. Enhanced performance in fluorene-free organometal halide perovskite light-emitting diodes using tunable, low electron affinity oxide electron injectors. *Adv. Mater.* **2015**, *27*, 1414-1419.
- (134) Chih, Y. K.; Wang, J. C.; Yang, R. T.; Liu, C. C.; Chang, Y. C.; Fu, Y. S.; Lai, W. C.; Chen, P.; Wen, T. C.; Huang, Y. C. NiOx Electrode Interlayer and CH₃NH₂/CH₃NH₃PbBr₃ Interface Treatment to Markedly Advance Hybrid Perovskite - Based Light - Emitting Diodes. *Adv. Mater.* **2016**, *28*, 8687-8694.
- (135) Lee, B. R.; Yu, J. C.; Park, J. H.; Lee, S.; Mai, C.-K.; Zhao, B.; Wong, M. S.; Jung, E. D.; Nam, Y. S.; Park, S. Y. Conjugated Polyelectrolytes as Efficient Hole Transport Layers in Perovskite Light-Emitting Diodes. *ACS nano* **2018**, *12*, 5826-5833.
- (136) Wood, V.; Bulović, V. Colloidal quantum dot light-emitting devices. *Nano reviews* **2010**, *1*, 5202.
- (137) Morgan, N. Y.; Leatherdale, C.; Drndić, M.; Jarosz, M. V.; Kastner, M. A.; Bawendi, M. Electronic transport in films of colloidal CdSe nanocrystals. *Phys. Rev. B* **2002**, *66*, 075339.
- (138) Lee, J.; Sundar, V. C.; Heine, J. R.; Bawendi, M. G.; Jensen, K. F. Full color emission from II-VI semiconductor quantum dot-polymer composites. *Adv. Mater.* **2000**, *12*, 1102-1105.
- (139) Wood, V.; Panzer, M. J.; Chen, J.; Bradley, M. S.; Halpert, J. E.; Bawendi, M. G.; Bulović, V. Inkjet - printed quantum dot - polymer composites for full - color ac - driven displays. *Adv. Mater.* **2009**, *21*, 2151-2155.
- (140) Kagan, C.; Murray, C.; Bawendi, M. Long-range resonance transfer of electronic excitations in close-packed CdSe quantum-dot solids. *Phys. Rev. B* **1996**, *54*, 8633.
- (141) Borchardt, J. K. Developments in organic displays. *Mater. Today* **2004**, *7*, 42-46.
- (142) Reineke, S.; Lindner, F.; Schwartz, G.; Seidler, N.; Walzer, K.; Lüssem, B.; Leo, K. White organic light-emitting diodes with fluorescent tube efficiency. *Nature* **2009**, *459*, 234.
- (143) Kabra, D.; Lu, L. P.; Song, M. H.; Snaith, H. J.; Friend, R. H. Efficient Single - Layer Polymer Light - Emitting Diodes. *Adv. Mater.* **2010**, *22*, 3194-3198.
- (144) Shimada, Y.; Ishino, J.; Shirasaki, S.; Irie, T.; Kikuchi, A. Effect of MgZnO-bilayer/BA-CH₃ combination interlayer on emission characteristics of MoO₃/F8BT/ZnO hybrid light emitting diodes fabricated on ZnO/Ag/ZnO transparent cathode. *Displays* **2013**, *34*, 437-441.
- (145) Bharathan, J.; Yang, Y. Polymer electroluminescent devices processed by inkjet printing: I. Polymer light-emitting logo. *Appl. Phys. Lett.* **1998**, *72*, 2660-2662.
- (146) Dai, X.; Zhang, Z.; Jin, Y.; Niu, Y.; Cao, H.; Liang, X.; Chen, L.; Wang, J.; Peng, X. Solution-processed, high-performance light-emitting diodes based on quantum dots. *Nature* **2014**, *515*, 96.
- (147) Aziz, H.; Popovic, Z. D.; Hu, N.-X.; Hor, A.-M.; Xu, G. Degradation mechanism of small molecule-based organic light-emitting devices. *Science* **1999**, *283*, 1900.

- (148) Cho, H.; Kim, Y. H.; Wolf, C.; Lee, H. D.; Lee, T. W. Improving the Stability of Metal Halide Perovskite Materials and Light - Emitting Diodes. *Adv. Mater.* **2018**, 1704587.
- (149) Arora, N.; Dar, M. I.; Hinderhofer, A.; Pellet, N.; Schreiber, F.; Zakeeruddin, S. M.; Grätzel, M. Perovskite solar cells with CuSCN hole extraction layers yield stabilized efficiencies greater than 20%. *Science* **2017**, 5655.
- (150) Bryant, D.; Aristidou, N.; Pont, S.; Sanchez-Molina, I.; Chotchunangatchaval, T.; Wheeler, S.; Durrant, J. R.; Haque, S. A. Light and oxygen induced degradation limits the operational stability of methylammonium lead triiodide perovskite solar cells. *Energy Environ. Sci.* **2016**, 9, 1655.
- (151) Eames, C.; Frost, J. M.; Barnes, P. R.; O'regan, B. C.; Walsh, A.; Islam, M. S. Ionic transport in hybrid lead iodide perovskite solar cells. *Nat. commun.* **2015**, 6, 7497.
- (152) Ahn, N.; Kwak, K.; Jang, M. S.; Yoon, H.; Lee, B. Y.; Lee, J.-K.; Pikhitsa, P. V.; Byun, J.; Choi, M. Trapped charge-driven degradation of perovskite solar cells. *Nat. commun.* **2016**, 7, 13422.
- (153) Aristidou, N.; Eames, C.; Sanchez-Molina, I.; Bu, X.; Kosco, J.; Islam, M. S.; Haque, S. A. Fast oxygen diffusion and iodide defects mediate oxygen-induced degradation of perovskite solar cells. *Nat. commun.* **2017**, 8, 15218.
- (154) Niu, G.; Li, W.; Meng, F.; Wang, L.; Dong, H.; Qiu, Y. Study on the stability of CH₃NH₃PbI₃ films and the effect of post-modification by aluminum oxide in all-solid-state hybrid solar cells. *J. Mater. Chem. A* **2014**, 2, 705-710.
- (155) Burschka, J.; Pellet, N.; Moon, S.-J.; Humphry-Baker, R.; Gao, P.; Nazeeruddin, M. K.; Grätzel, M. Sequential deposition as a route to high-performance perovskite-sensitized solar cells. *Nature* **2013**, 499, 316.
- (156) Zhang, L.; Ju, M.-G.; Liang, W. The effect of moisture on the structures and properties of lead halide perovskites: a first-principles theoretical investigation. *Phys. Chem. Chem. Phys.* **2016**, 18, 23174-23183.
- (157) Habisreutinger, S. N.; Leijtens, T.; Eperon, G. E.; Stranks, S. D.; Nicholas, R. J.; Snaith, H. J. Carbon nanotube/polymer composites as a highly stable hole collection layer in perovskite solar cells. *Nano Lett.* **2014**, 14, 5561-5568.
- (158) Ahn, N.; Kwak, K.; Jang, M. S.; Yoon, H.; Lee, B. Y.; Lee, J. K.; Pikhitsa, P. V.; Byun, J.; Choi, M. Trapped charge-driven degradation of perovskite solar cells. *Nat. commun.* **2016**, 7, 13422.
- (159) Galisteo-López, J. F.; Anaya, M.; Calvo, M.; Míguez, H. Environmental effects on the photophysics of organic-inorganic halide perovskites. *J. Phys. Chem. Lett.* **2015**, 6, 2200-2205.
- (160) Stranks, S. D.; Burlakov, V. M.; Leijtens, T.; Ball, J. M.; Goriely, A.; Snaith, H. J. Recombination kinetics in organic-inorganic perovskites: excitons, free charge, and subgap states. *Phys. Rev. Appl.* **2014**, 2, 034007.
- (161) Christians, J. A.; Miranda Herrera, P. A.; Kamat, P. V. Transformation of the excited state and photovoltaic efficiency of CH₃NH₃PbI₃ perovskite upon controlled exposure to humidified air. *J. Am. Chem. Soc.* **2015**, 137, 1530-1538.
- (162) Gottesman, R.; Haltzi, E.; Gouda, L.; Tirosh, S.; Bouhadana, Y.; Zaban, A.; Mosconi, E.; De Angelis, F. Extremely slow photoconductivity response of CH₃NH₃PbI₃ perovskites suggesting structural changes under working conditions. *J. Phys. Chem. Lett.* **2014**, 5, 2662-2669.

- (163) Merdasa, A.; Bag, M.; Tian, Y.; Källman, E.; Dobrovolsky, A.; Scheblykin, I. G. Super-Resolution Luminescence Microspectroscopy Reveals the Mechanism of Photoinduced Degradation in CH₃NH₃PbI₃ Perovskite Nanocrystals. *J. Phys. Chem. C* **2016**, *120*, 10711-10719.
- (164) Yuan, Y.; Huang, J. Ion migration in organometal trihalide perovskite and its impact on photovoltaic efficiency and stability. *Acc. Chem. Res.* **2016**, *49*, 286-293.
- (165) Lee, S.; Park, J. H.; Lee, B. R.; Jung, E. D.; Yu, J. C.; Di Nuzzo, D.; Friend, R. H.; Song, M. H. Amine-based passivating materials for enhanced optical properties and performance of organic-inorganic perovskites in light-emitting diodes. *J. Phys. Chem. Lett.* **2017**, *8*, 1784-1792.
- (166) Back, H.; Kim, G.; Kim, J.; Kong, J.; Kim, T. K.; Kang, H.; Kim, H.; Lee, J.; Lee, S.; Lee, K. Achieving long-term stable perovskite solar cells via ion neutralization. *Energy Environ. Sci.* **2016**, *9*, 1258-1263.
- (167) Besleaga, C.; Abramiuc, L. E.; Stancu, V.; Tomulescu, A. G.; Sima, M.; Trinca, L.; Plugaru, N.; Pintilie, L.; Nemnes, G. A.; Iliescu, M. Iodine migration and degradation of perovskite solar cells enhanced by metallic electrodes. *J. Phys. Chem. Lett.* **2016**, *7*, 5168-5175.
- (168) Zhao, L.; Kerner, R. A.; Xiao, Z.; Lin, Y. L.; Lee, K. M.; Schwartz, J.; Rand, B. P. Redox Chemistry Dominates the Degradation and Decomposition of Metal Halide Perovskite Optoelectronic Devices. *ACS Energy Lett.* **2016**, *1*, 595.
- (169) Carrillo, J.; Guerrero, A.; Rahimnejad, S.; Almora, O.; Zarazua, I.; Mas - Marza, E.; Bisquert, J.; Garcia - Belmonte, G. Ionic reactivity at contacts and aging of methylammonium lead triiodide perovskite solar cells. *Adv. Energy Mater.* **2016**, *6*, 1502246.
- (170) Li, J.; Shan, X.; Bade, S. G. R.; Geske, T.; Jiang, Q.; Yang, X.; Yu, Z. Single-layer halide perovskite light-emitting diodes with sub-band gap turn-on voltage and high brightness. *J. Phys. Chem. Lett.* **2016**, *7*, 4059-4066.
- (171) Li, J.; Bade, S. G. R.; Shan, X.; Yu, Z. Single - Layer Light - Emitting Diodes Using Organometal Halide Perovskite/Poly (ethylene oxide) Composite Thin Films. *Adv. Mater.* **2015**, *27*, 5196-5202.
- (172) Shan, X.; Li, J.; Chen, M.; Geske, T.; Bade, S. G. R.; Yu, Z. Junction Propagation in Organometal Halide Perovskite-Polymer Composite Thin Films. *J. Phys. Chem. Lett.* **2017**, *8*, 2412-2419.
- (173) Wang, X.; Ling, Y.; Chiu, Y.-C.; Du, Y.; Barreda, J. L.; Perez-Orive, F.; Ma, B.; Xiong, P.; Gao, H. Dynamic Electronic Junctions in Organic-Inorganic Hybrid Perovskites. *Nano Lett.* **2017**, *17*, 4831-4839.
- (174) Kim, H. P.; Kim, J.; Kim, B. S.; Kim, H.-M.; Kim, J.; Yusoff, A. R. b. M.; Jang, J.; Nazeeruddin, M. K. High-Efficiency, Blue, Green, and Near-Infrared Light-Emitting Diodes Based on Triple Cation Perovskite. *Adv. Optical Mater.* **2017**, *5*, 1600920.
- (175) Diroll, B. T.; Nedelcu, G.; Kovalenko, M. V.; Schaller, R. D. High-Temperature Photoluminescence of CsPbX₃ (X = Cl, Br, I) Nanocrystals. *Adv. Funct. Mater.* **2017**, *27*, 1606750.
- (176) Tian, Y.; Zhou, C.; Worku, M.; Wang, X.; Ling, Y.; Gao, H.; Zhou, Y.; Miao, Y.; Guan, J.; Ma, B. Highly Efficient Spectrally Stable Red Perovskite Light - Emitting Diodes. *Adv. Mater.* **2018**, *30*, 1707093.

- (177) Kim, Y.-H.; Wolf, C.; Kim, H.; Lee, T.-W. Charge carrier recombination and ion migration in metal-halide perovskite nanoparticle films for efficient light-emitting diodes. *Nano Energy* **2018**, *52*, 329-335.
- (178) Sutherland, B. R.; Hoogland, S.; Adachi, M. M.; Kanjanaboos, P.; Wong, C. T.; McDowell, J. J.; Xu, J.; Voznyy, O.; Ning, Z.; Houtepen, A. J. Perovskite thin films via atomic layer deposition. *Adv. Mater.* **2015**, *27*, 53-58.
- (179) Xing, G.; Mathews, N.; Lim, S. S.; Yantara, N.; Liu, X.; Sabba, D.; Grätzel, M.; Mhaisalkar, S.; Sum, T. C. Low-temperature solution-processed wavelength-tunable perovskites for lasing. *Nat. Mater.* **2014**, *13*, 476.
- (180) Sutherland, B. R.; Hoogland, S.; Adachi, M. M.; Wong, C. T.; Sargent, E. H. Conformal organohalide perovskites enable lasing on spherical resonators. *ACS nano* **2014**, *8*, 10947-10952.
- (181) Stranks, S. D.; Wood, S. M.; Wojciechowski, K.; Deschler, F.; Saliba, M.; Khandelwal, H.; Patel, J. B.; Elston, S. J.; Herz, L. M.; Johnston, M. B. Enhanced amplified spontaneous emission in perovskites using a flexible cholesteric liquid crystal reflector. *Nano Lett.* **2015**, *15*, 4935-4941.
- (182) Kao, T. S.; Chou, Y.-H.; Chou, C.-H.; Chen, F.-C.; Lu, T.-C. Lasing behaviors upon phase transition in solution-processed perovskite thin films. *Appl. Phys. Lett.* **2014**, *105*.
- (183) Yakunin, S.; Protesescu, L.; Krieg, F.; Bodnarchuk, M. I.; Nedelcu, G.; Humer, M.; De Luca, G.; Fiebig, M.; Heiss, W.; Kovalenko, M. V. Low-threshold amplified spontaneous emission and lasing from colloidal nanocrystals of caesium lead halide perovskites. *Nat. commun.* **2015**, *6*.
- (184) Wang, Y.; Li, X.; Song, J.; Xiao, L.; Zeng, H.; Sun, H. All-Inorganic Colloidal Perovskite Quantum Dots: A New Class of Lasing Materials with Favorable Characteristics. *Adv. Mater.* **2015**, *27*, 7101-7108.
- (185) Pan, J.; Sarmah, S. P.; Murali, B.; Dursun, I.; Peng, W.; Parida, M. R.; Liu, J.; Sinatra, L.; Alyami, N.; Zhao, C. Air-stable surface-passivated perovskite quantum dots for ultra-robust, single-and two-photon-induced amplified spontaneous emission. *J. Phys. Chem. Lett.* **2015**, *6*, 5027-5033.
- (186) Eaton, S. W.; Lai, M.; Gibson, N. A.; Wong, A. B.; Dou, L.; Ma, J.; Wang, L.-W.; Leone, S. R.; Yang, P. Lasing in robust cesium lead halide perovskite nanowires. *Proceedings of the National Academy of Sciences* **2016**, *113*, 1993-1998.
- (187) Klimov, V. I. Spectral and dynamical properties of multiexcitons in semiconductor nanocrystals. *Annu. Rev. Phys. Chem.* **2007**, *58*, 635-673.
- (188) Yuan, F.; Wu, Z.; Dong, H.; Xi, J.; Xi, K.; Divitini, G.; Jiao, B.; Hou, X.; Wang, S.; Gong, Q. High Stability and Ultralow Threshold Amplified Spontaneous Emission from Formamidinium Lead Halide Perovskite Films. *J. Phys. Chem. C* **2017**, *121*, 15318-15325.
- (189) Fu, Y.; Zhu, H.; Schrader, A. W.; Liang, D.; Ding, Q.; Joshi, P.; Hwang, L.; Zhu, X. Y.; Jin, S. Nanowire Lasers of Formamidinium Lead Halide Perovskites and Their Stabilized Alloys with Improved Stability. *Nano Lett.* **2016**, *16*, 1000-1008.
- (190) Shum, K.; Chen, Z.; Qureshi, J.; Yu, C.; Wang, J. J.; Pfenninger, W.; Vockic, N.; Midgley, J.; Kenney, J. T. Synthesis and characterization of CsSnI₃ thin films. *Appl. Phys. Lett.* **2010**, *96*, 221903.
- (191) Lee, B.; He, J.; Chang, R. P.; Kanatzidis, M. G. All-solid-state dye-sensitized solar cells with high efficiency. *Nature* **2012**, *485*, 486.

- (192) Huang, L.-y.; Lambrecht, W. R. Electronic band structure, phonons, and exciton binding energies of halide perovskites CsSnCl₃, CsSnBr₃, and CsSnI₃. *Phys. Rev. B* **2013**, *88*, 165203.
- (193) Hao, F.; Stoumpos, C. C.; Cao, D. H.; Chang, R. P.; Kanatzidis, M. G. Lead-free solid-state organic-inorganic halide perovskite solar cells. *Nat. Photonics* **2014**, *8*, 489.
- (194) Chong, W. K.; Thirumal, K.; Giovanni, D.; Goh, T. W.; Liu, X.; Mathews, N.; Mhaisalkar, S.; Sum, T. C. Dominant factors limiting the optical gain in layered two-dimensional halide perovskite thin films. *Phys. Chem. Chem. Phys.* **2016**, *18*, 14701-14708.
- (195) Li, M.; Wei, Q.; Muduli, S. K.; Yantara, N.; Xu, Q.; Mathews, N.; Mhaisalkar, S. G.; Xing, G.; Sum, T. C. Enhanced Exciton and Photon Confinement in Ruddlesden - Popper Perovskite Microplatelets for Highly Stable Low - Threshold Polarized Lasing. *Adv. Mater.* **2018**, *30*, 1707235.
- (196) Zhu, H.; Fu, Y.; Meng, F.; Wu, X.; Gong, Z.; Ding, Q.; Gustafsson, M. V.; Trinh, M. T.; Jin, S.; Zhu, X. Y. Lead halide perovskite nanowire lasers with low lasing thresholds and high quality factors. *Nat. Mater.* **2015**, *14*, 636.
- (197) Zhang, Q.; Ha, S. T.; Liu, X.; Sum, T. C.; Xiong, Q. Room-temperature near-infrared high-Q perovskite whispering-gallery planar nanolasers. *Nano Lett.* **2014**, *14*, 5995-6001.
- (198) Liao, Q.; Hu, K.; Zhang, H.; Wang, X.; Yao, J.; Fu, H. Perovskite Microdisk Microlasers Self-Assembled from Solution. *Adv. Mater.* **2015**, *27*, 3405-3410.
- (199) Jia, Y.; Kerner, R. A.; Grede, A. J.; Brigeman, A. N.; Rand, B. P.; Giebink, N. C. Diode-pumped organo-lead halide perovskite lasing in a metal-clad distributed feedback resonator. *Nano Lett.* **2016**, *16*, 4624-4629.
- (200) Saliba, M.; Wood, S. M.; Patel, J. B.; Nayak, P. K.; Huang, J.; Alexander-Webber, J. A.; Wenger, B.; Stranks, S. D.; Horantner, M. T.; Wang, J. T. et al. Structured Organic-Inorganic Perovskite toward a Distributed Feedback Laser. *Adv. Mater.* **2016**, *28*, 923-929.
- (201) Chen, S.; Zhang, C.; Lee, J.; Han, J.; Nurmikko, A. High-Q, Low-Threshold Monolithic Perovskite Thin-Film Vertical-Cavity Lasers. *Adv. Mater.* **2017**, *29*.
- (202) Jia, Y.; Kerner, R. A.; Grede, A. J.; Rand, B. P.; Giebink, N. C. Continuous-wave lasing in an organic-inorganic lead halide perovskite semiconductor. *Nat. Photonics* **2017**, *11*, 784.
- (203) Lin, K.; Xing, J.; Quan, L. N.; de Arquer, F. P. G.; Gong, X.; Lu, J.; Xie, L.; Zhao, W.; Zhang, D.; Yan, C. Perovskite light-emitting diodes with external quantum efficiency exceeding 20 per cent. *Nature* **2018**, *562*, 245.
- (204) Ban, M.; Zou, Y.; Rivett, J. P.; Yang, Y.; Thomas, T. H.; Tan, Y.; Song, T.; Gao, X.; Credington, D.; Deschler, F. Solution-processed perovskite light emitting diodes with efficiency exceeding 15% through additive-controlled nanostructure tailoring. *Nat. commun.* **2018**, *9*, 3892.
- (205) Xing, J.; Zhao, Y.; Askerka, M.; Quan, L. N.; Gong, X.; Zhao, W.; Zhao, J.; Tan, H.; Long, G.; Gao, L. Color-stable highly luminescent sky-blue perovskite light-emitting diodes. *Nat. commun.* **2018**, *9*, 3541.
- (206) Gong, X.; Voznyy, O.; Jain, A.; Liu, W.; Sabatini, R.; Piontkowski, Z.; Walters, G.; Bappi, G.; Nokhrin, S.; Bushuyev, O. Electron-phonon interaction in efficient perovskite blue emitters. *Nat. Mater.* **2018**, *1*.

- (207) Zhao, L.; Rolston, N.; Lee, K. M.; Zhao, X.; Reyes - Martinez, M. A.; Tran, N. L.; Yeh, Y. W.; Yao, N.; Scholes, G. D.; Loo, Y. L. Influence of Bulky Organo - Ammonium Halide Additive Choice on the Flexibility and Efficiency of Perovskite Light - Emitting Devices. *Adv. Funct. Mater.* **2018**, 1802060.
- (208) Zeng, W.; Lai, H. Y.; Lee, W. K.; Jiao, M.; Shiu, Y. J.; Zhong, C.; Gong, S.; Zhou, T.; Xie, G.; Sarma, M. Achieving Nearly 30% External Quantum Efficiency for Orange - Red Organic Light Emitting Diodes by Employing Thermally Activated Delayed Fluorescence Emitters Composed of 1, 8 - Naphthalimide - Acridine Hybrids. *Adv. Mater.* **2018**, 30, 1704961.
- (209) Yang, X.; Zhang, X.; Deng, J.; Chu, Z.; Jiang, Q.; Meng, J.; Wang, P.; Zhang, L.; Yin, Z.; You, J. Efficient green light-emitting diodes based on quasi-two-dimensional composition and phase engineered perovskite with surface passivation. *Nat. commun.* **2018**, 9, 570.
- (210) Yang, Y.; Zheng, Y.; Cao, W.; Titov, A.; Hyvonen, J.; Manders, J. R.; Xue, J.; Holloway, P. H.; Qian, L. High-efficiency light-emitting devices based on quantum dots with tailored nanostructures. *Nat. Photonics* **2015**, 9, nphoton. 2015.2036.
- (211) Di, D.; Romanov, A. S.; Yang, L.; Richter, J. M.; Rivett, J. P.; Jones, S.; Thomas, T. H.; Jalebi, M. A.; Friend, R. H.; Linnolahti, M. High-performance light-emitting diodes based on carbene-metal-amides. *Science* **2017**, eaah4345.
- (212) Lee, C. W.; Lee, J. Y. Above 30% external quantum efficiency in blue phosphorescent organic light - emitting diodes using pyrido [2, 3 - b] indole derivatives as host materials. *Adv. Mater.* **2013**, 25, 5450-5454.
- (213) Zhao, L.; Yeh, Y. W.; Tran, N. L.; Wu, F.; Xiao, Z.; Kerner, R. A.; Lin, Y. L.; Scholes, G. D.; Yao, N.; Rand, B. P. In Situ Preparation of Metal Halide Perovskite Nanocrystal Thin Films for Improved Light-Emitting Devices. *ACS Nano* **2017**, 11, 3957-3964.
- (214) <http://www.udcoled.com/>.
- (215) Correa-Baena, J.-P.; Saliba, M.; Buonassisi, T.; Grätzel, M.; Abate, A.; Tress, W.; Hagfeldt, A. Promises and challenges of perovskite solar cells. *Science* **2017**, 358, 739-744.
- (216) Saliba, M.; Matsui, T.; Domanski, K.; Seo, J.-Y.; Ummadisingu, A.; Zakeeruddin, S. M.; Correa-Baena, J.-P.; Tress, W. R.; Abate, A.; Hagfeldt, A. Incorporation of rubidium cations into perovskite solar cells improves photovoltaic performance. *Science* **2016**, 354, 206-209.
- (217) Li, B.; Kawakita, Y.; Liu, Y.; Wang, M.; Matsuura, M.; Shibata, K.; Ohira-Kawamura, S.; Yamada, T.; Lin, S.; Nakajima, K. Polar rotor scattering as atomic-level origin of low mobility and thermal conductivity of perovskite CH₃NH₃PbI₃. *Nat. commun.* **2017**, 8, 16086.
- (218) Saparov, B.; Mitzi, D. B. Organic-inorganic perovskites: structural versatility for functional materials design. *Chem. Rev.* **2016**, 116, 4558-4596.
- (219) Mao, L.; Wu, Y.; Stoumpos, C. C.; Wasielewski, M. R.; Kanatzidis, M. G. White-light emission and structural distortion in new corrugated two-dimensional lead bromide perovskites. *J. Am. Chem. Soc.* **2017**, 139, 5210-5215.
- (220) Protesescu, L.; Yakunin, S.; Kumar, S.; Bar, J.; Bertolotti, F.; Masciocchi, N.; Guagliardi, A.; Grotevent, M.; Shorubalko, I.; Bodnarchuk, M. I. et al. Dismantling the "Red Wall" of Colloidal Perovskites: Highly Luminescent Formamidinium and Formamidinium-Cesium Lead Iodide Nanocrystals. *ACS Nano* **2017**, 11, 3119-3134.

- (221) Chih, Y. K.; Wang, J. C.; Yang, R. T.; Liu, C. C.; Chang, Y. C.; Fu, Y. S.; Lai, W. C.; Chen, P.; Wen, T. C.; Huang, Y. C. et al. NiO_x Electrode Interlayer and CH₃NH₂ /CH₃NH₃PbBr₃ Interface Treatment to Markedly Advance Hybrid Perovskite-Based Light-Emitting Diodes. *Adv. Mater.* **2016**, *28*, 8687-8694.
- (222) Seo, H. K.; Kim, H.; Lee, J.; Park, M. H.; Jeong, S. H.; Kim, Y. H.; Kwon, S. J.; Han, T. H.; Yoo, S.; Lee, T. W. Efficient Flexible Organic/Inorganic Hybrid Perovskite Light - Emitting Diodes Based on Graphene Anode. *Adv. Mater.* **2017**, *29*, 1605587.
- (223) Fan, Z.; Xiao, H.; Wang, Y.; Zhao, Z.; Lin, Z.; Cheng, H.-C.; Lee, S.-J.; Wang, G.; Feng, Z.; Goddard III, W. A. Layer-by-layer degradation of methylammonium lead tri-iodide perovskite microplates. *Joule* **2017**, *1*, 548-562.
- (224) Tsai, H.; Nie, W.; Blancon, J. C.; Stoumpos, C. C.; Soe, C. M. M.; Yoo, J.; Crochet, J.; Tretiak, S.; Even, J.; Sadhanala, A. Stable Light - Emitting Diodes Using Phase - Pure Ruddlesden-Popper Layered Perovskites. *Adv. Mater.* **2018**, *30*, 1704217.
- (225) Sum, T. C.; Mathews, N.; Xing, G.; Lim, S. S.; Chong, W. K.; Giovanni, D.; Dewi, H. A. Spectral features and charge dynamics of lead halide perovskites: origins and interpretations. *Acc. Chem. Res.* **2016**, *49*, 294-302.